Universidade de Lisboa

Faculdade de Ciências

Departamento de Engenharia Geográfica Geofísica e Energia

Climatic changes in the Western Iberian Upwelling System

José Miguel Rodrigues Alves

Doutoramento em Ciências Geofísicas e da Geoinformação
(Meteorologia)

Tese Orientada por:
Prof. Doutor Pedro Miranda
Doutor Nuno Serra

2011

Contents

Acknowledgements

I thank my advisors Pedro Miranda and Nuno Serra for their guidance and support during my PhD. In particular, I thank Nuno Serra for welcoming me at the University of Hamburg during my one month visit.

I acknowledge the Instituto Dom Luiz (IDL - Centro de Geofísica), my host institution, for the given work conditions, in particular, the computational time that was essential to conduct this work. IDL is funded by the Portuguese Foundation for Science and Technology (FCT) under the project PEST-OE/CTE/LA0019/2011/2012.

I show gratitude to John Warner for having permitted me to visit the USGS in Woods Hole, Massachusetts, USA, which allowed me to gain experience with an atmosphere-ocean coupled modelling system and for having given me access to the USGS computer cluster, used to perform the coupled simulations.

The RACMO data used in Chapter five was provided through the PRUDENCE data archive funded by the European Union through contract EVK2-CT2001-00132.

This work was supported by FCT under grant SFRH/BD/32049/2006 and in the frame of project AMIC (grant PTDC/AAC-CLI/109030/2008).

I thank my colleagues (Emanuel, João Martins, Miguel Nogueira, Miguel Teixeira, Pedro Soares Ricardo, Sandra and Rita) in the laboratory for their friendship and support during the last years. I also thank Greg King for his comments on the final stage of the thesis.

I am grateful to my family, Father, Mother, Pedro, Ana and Leonor; without their constant encouragement it would not be possible to finish my PhD. Special thanks go to Sandra for her patient, motivation and love.

Abstract

This study is largely based on numerical simulations and focuses the Iberian coastal upwelling. The dissertation aims at improving the understanding on the behaviour of coastal upwelling in the context of climate change. The analysis relies on sets of numerical simulations conducted with a regional ocean numerical model and a coupled atmosphere-ocean coupled model system. Two separate questions are addressed: (1) which physical variables characterize best the Iberian upwelling? (2) what trends are to be expected in Iberian upwelling with global warming?

Two multi-decadal simulations were realized with an ocean numerical model forced with reanalysis atmospheric data from the European Centre for Medium-Range Weather Forecast (ECMWF). During the last two simulated decades, a decreasing number of coastal upwelling events in the northern part of the western Iberian coast and an increasing number of coastal upwelling events in the southern part of western Iberian coast were noted. These opposite trends in the mean number of coastal upwelling days are in good agreement with the trends of the meridional component of wind off western Iberia, computed with ERA-40, ERA-Interim and satellite scatterometer data, all indicating a weakening of meridional wind intensity in the north and an intensification of the meridional wind intensity in the south.

To assess the impact of climate change in the frequency and intensity of coastal upwelling events off western Iberia, a control simulation corresponding to the 1961-1990 climate and a scenario simulation for the period 2071-2100 were conducted, using seven forcing atmospheric variables (surface wind, shortwave net radiation, surface air temperature, surface pressure, relative humidity, cloud cover and precipitation rate) retrieved from the RACMO (Regional Atmospheric Climate Model) simulations. When analysing the forcing variable with more impact on the upwelling, the surface wind, an increase in both the westerly and northerly components of the mean surface wind over the last 30 years of the XXI century is simulated by RACMO, resulting in an increase of the intensity of coastal upwelling during the scenario period.

A coupled model system, comprised of an ocean, an atmosphere and a wave model, was used to show the large impact of ocean surface waves on the sea surface and atmospheric surface temperature fields during the summer season, most probably related with the large ocean vertical temperature gradient during this season.

Keywords: Climate change, coastal upwelling, sea surface temperature, surface wind, numerical modelling

Resumo

Esta tese de doutoramento baseia-se no estudo do afloramento costeiro, um fenómeno que se caracteriza pela emersão à superfície de água profunda que normalmente apresenta temperaturas relativamente baixas e elevados valores de concentração de nutrientes. Este fenómeno ocorre nalgumas regiões costeiras dos oceanos, devido ao efeito combinado da rotação da terra e do vento sobre as águas à superfície do oceano. Devido ao transporte para o largo das correntes à superfície que este efeito implica, o transporte para o largo por continuidade tem de ser compensado com água mais profunda que emerge à superfície. As regiões onde se observa o afloramento costeiro nos oceanos englobam menos de 1% da área total dos oceanos, mas, devido ao elevado teor de nutrientes das águas superficiais, é estimado que 20% das pescas globais se verifiquem nestas regiões.

Em termos físicos, o facto de se verificar um súbito arrefecimento da temperatura da superfície do mar quando se verifica um episódio de afloramento costeiro também implica um clima mais fresco nas regiões costeiras adjacentes sobre o continente, nomeadamente através de um regime de brisa costeira.

A costa ocidental da Península Ibérica constitui o limite Norte de um dos maiores ecossistemas de afloramento costeiro do Oceano Mundial, que se estende desde a costa do Senegal a sul, até ao extremo norte da costa ocidental da Península Ibérica. Os limites sul e norte deste ecossistema variam sazonalmente de acordo com o regime de ventos regional, sendo que ao largo da costa ocidental da Península Ibérica este fenómeno é normalmente observado durante o Verão, devido aos ventos de norte causados pelo anticiclone dos Açores a pela depressão térmica no centro da Península Ibérica que se forma normalmente durante os meses de Verão.

Esta tese teve como um dos principais objectivos contribuir com os resultados apresentados para identificar tendências recentes do afloramento costeiro ao longo da costa ocidental da Península Ibérica, utilizando para este fim modelos numéricos de circulação atmosférica e oceânica. Nesta tese foram realizadas simulações com um modelo numérico de circulação oceânica e um sistema composto por três modelos acoplados, um oceânico, um atmosférico e outro de agitação marítima.

Com o modelo numérico oceânico foram realizadas duas simulações forçadas por dados de duas reanálises atmosféricas do Centro Europeu (ECMWF), uma para o período 1961 a 2001 (ERA-40) e outra para o período 1989 a 2008 (ERA-Interim). Nestas simulações verificou-se uma tendência de decréscimo do número de dias de afloramento costeiro a norte e uma tendência para o aumento do número de dias de afloramento costeiro na parte sul da costa ocidental da Península Ibérica. Estas tendências estão de acordo com a tendência observada na variável atmosférica com maior influência no afloramento costeiro, o vento à superfície. Com efeito, na componente meridional do vento ao longo da costa ocidental da Península Ibérica observou-se um enfraquecimento na parte Norte e uma

intensificação na parte sul. Em relação à elevação da superfície do mar junto à costa, verificou-se um aumento do nível médio do mar, embora este aumento tenha vindo a diminuir de intensidade nas últimas décadas analisadas, possivelmente devido ao aumento do número de eventos de afloramento costeiro, que implicam um decréscimo do nível médio do mar junto à costa e um aumento ao largo devido à convergência verificado nas camadas superficiais do oceano durante um evento de afloramento costeiro.

O campo da temperatura da superfície do mar simulado pelo modelo de circulação oceânica foi validado com dados de satélite, tendo-se verificado diferenças pequenas entre a temperatura simulada pelo modelo e a obtida a partir de dados de satélite. Da comparação dos anos comuns às simulações realizadas com os dados ERA-40 e ERA-Interim, verificou-se que esta última apresenta resultados mais próximos aos observados por satélite. Observou-se que a variabilidade da temperatura da superfície do mar é superior junto à costa que ao largo, devido ao arrefecimento causado pelo afloramento costeiro junto à costa durante o Verão.

De modo a identificar o impacto das alterações climáticas no afloramento costeiro, foram realizadas duas simulações com o modelo numérico oceânico forçado com dados atmosféricos de um modelo regional de Clima o qual teve em conta a concentração de gases com efeito de estufa previstas no cenário A2 do IPCC (International Panel for Climate Change). É importante referir que, até ao presente, o efeito do afloramento costeiro não se encontra correctamente representado nas simulações apresentadas pelo IPCC, devido à baixa resolução utilizada nas simulações globais. Uma intensificação do afloramento costeiro numa região pode implicar um clima menos quente ou mesmo mais frio, pelo que determinar a tendência do afloramento costeiro num cenário futuro pode ter implicações extremamente importantes nas regiões costeiras afectadas por este fenómeno.

Com o modelo numérico de circulação oceânica foi realizada uma simulação para o período de controlo (1961-1990) e uma outra simulação para o período de cenário (2071-2100). Da comparação dos resultados obtidos nestas duas simulações observou-se um aumento em cerca de 10% do número de dias de afloramento costeiro por ano no período de cenário, que provavelmente se deve a uma intensificação também de cerca de 10% do vento ao longo da costa ocidental da Península Ibérica. Interessa notar que o aumento do número de dias de afloramento costeiro é quase na totalidade verificado nos eventos mais intensos. Nos eventos de menor intensidade verifica-se um valor constante ou mesmo uma ligeira diminuição durante o período de cenário. Verificou-se também no período de cenário um ligeiro aumento das correntes à superfície do oceano. Em relação ao nível médio do mar verificou-se um decréscimo no período de cenário quando comparado com o período de controlo, devido ao efeito do aumento do número de dias de afloramento costeiro, que se sobrepõem ao efeito do aquecimento global, o qual implica um aumento do nível médio do mar devido à dilatação térmica

nas camadas superficiais do oceano. No período de cenário, embora a maioria dos eventos se continuem a verificar no verão, é notado um aumento do número de eventos nas outras estações do ano, particularmente durante o Inverno, estação em que no período de controlo quase não se verificaram eventos de afloramento costeiro. Associado ao aumento do número médio de dias de afloramento costeiro por ano no período de cenário, observou-se um aumento da variabilidade intra-anual da temperatura da superfície do mar.

Na parte final da tese são apresentados resultados obtidos com um sistema acoplado composto por três modelos, um modelo oceânico, outro de agitação marítima e outro atmosférico. Este sistema permitiu simular os fluxos de calor na interface atmosfera-oceano em tempo real e similar o impacto da inclusão de um modelo de agitação marítima no campo da temperatura à superfície do mar. Conclui-se que durante o verão o impacto da inclusão do modelo de agitação marítima é muito mais significativo do que durante o resto do ano, embora seja durante o verão que se observe um valor da altura significativa da agitação marítima com valores mais baixos. Esta situação é justificada pelo facto de no verão se verificar um maior gradiente vertical da temperatura junto à superfície do oceano. Em relação aos fluxos de calor latente e sensível, foi notado que estas duas variáveis são dois bons indicadores do afloramento costeiro, uma vez que são fortemente influenciadas pela variação da temperatura à superfície do oceano.

Palavras chave: alterações climáticas, afloramento costeiro, temperatura da superfície do mar, vento à superfície do mar, modelos numéricos

Chapter 1 **Motivation and objectives**

1.1 **Motivation**

Portugal, with a coast extension of about 1187 km and with more than 1.7 million km^2 of coastal waters representing approximately 18 times its terrestrial area, has one of the largest exclusive economic zones in Europe. But presently, it is also a country where the ocean related activities are far from being fully explored, in many cases, due to an absence of accurate scientific knowledge of atmospheric and oceanic coastal related phenomena.

Recently, some studies on the impact of sea-related activities in European national economies indicated their increasing importance in the upcoming decades. In Portugal, the Maritime Cluster, an association created to promote and stimulate sea-related activities, projected that the percentage of the national Gross Domestic Product (GDP) related with maritime activities can increase from the actual (2009) 2 % to between 4 % and 5 % in 2025. If indirect activities were taken into account than it is estimated that, by 2025, 10 % to 12 % of the national GDP may be associated with sea-related activities.

One of these sea-related activities is the fishing industry, where an accurate forecast of the coastal upwelling regime off the western Iberian coast will certainly improve the fish catchments records in the region. Other areas that can benefit from an accurate description of the ocean and atmospheric coastal conditions are the off-shore wind and ocean wave renewable energy fields, where several on-going research projects predict future significant contributions to the fraction of energy from renewable sources in Portugal. The maritime transport, in particular the harbour's activity, and the sea related tourism activities are other areas that can profit from an accurate high temporal and spatial resolution forecast of the atmospheric and oceanic coastal conditions.

The elaboration of climate scenarios for coastal regions is of great importance, as it is in these regions that approximately half of the European population lives, according to data from the European Commission. In Portugal, this percentage is even greater, as it is estimated that more than 75 % of the Portuguese population lives in coastal regions. The correct elaboration of decadal scenarios for these areas can have influence on the decision makers, in future investments and measures of mitigation in coastal zones.

The IPCC (Intergovernmental Panel on Climate Change) created different climate scenarios for the XXI century taken into account different levels of technological development and international cooperation between governments and international institutions. Figure 1 shows the projected evolution of the four main greenhouse gases in the different IPCC scenarios for the XXI century. The

greenhouse gases concentration trends depend significantly on the considered IPCC scenario. Each scenario accounts for a different social, economic and technical development, which represents different policies taken by the national governments and international institutions and that lead to different levels of technological development during the XXI century.

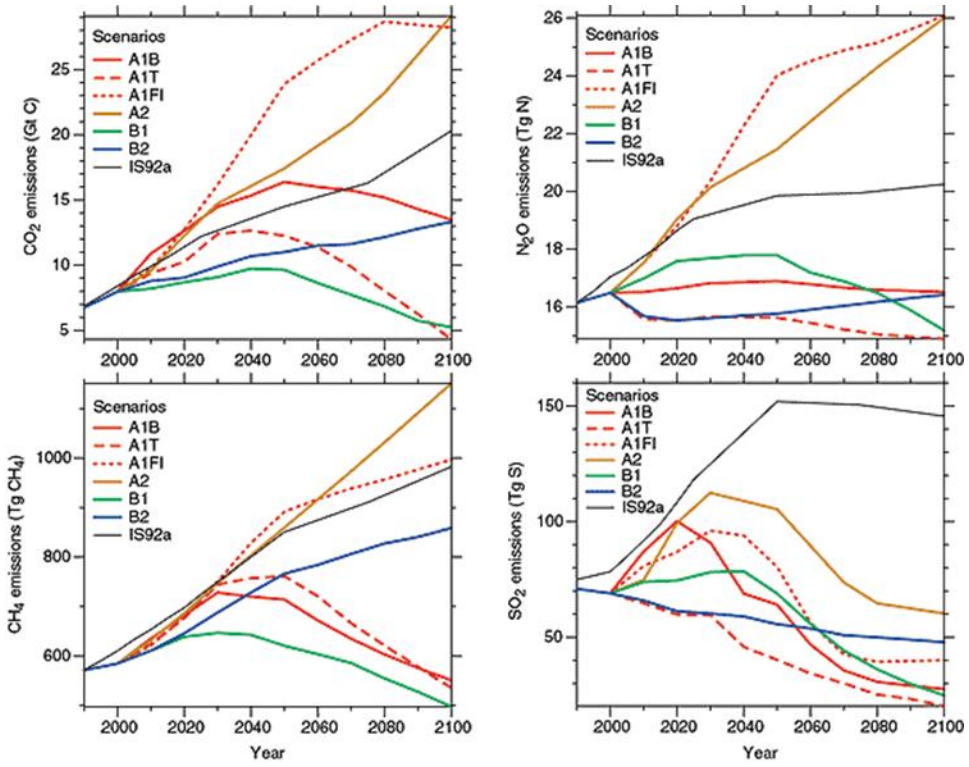

Figure 1 Projected evolution of four greenhouse gases (CO_2 ; N_2O ; CH_4 and SO_2) for the XXI century in the different IPCC scenarios. In the legend the letter B refers to a balanced energetic use across all energy sources, T to the use of non-fossil energy sources and FI to the use of fossil intensive energy sources. These three sub-scenarios of the A1 scenario are related with the future technological development during the XXI century. IS92a is the prediction from an earlier SAR (IPCC Second Assessment Report).

In the A1 and A2 scenarios more attention is given to economic policies, whereas in the B1 and B2 scenarios more focus is given to environmental policies. In the A1 and B1 scenarios there is an increasing international cooperation, whereas in the A2 and B2 scenarios the decision making power is transferred from the international to the national institutions and governments.

When looking at the IPCC scenarios, it is important to keep in mind that there is an uncertainty associated with each scenario that increases with the number of years being predicted. The uncertainty can be due to an inadequate scientific understanding of the problems, through data gaps or lack of data, and to the inherent uncertainties of future events. One example of an unpredictable event is a

huge volcano eruption that can have an impact on the mean global air temperature. For instance, it is estimated that the Mt. Pinatubo eruption in 1991 emitted about 20 megatons of SO_2 into the stratosphere, which implied a decrease of 0.5 °C in the surface air temperature and of 0.6 °C in the troposphere in mid-1992 (Parker et al, 1996). The stratospheric cloud from this eruption persisted in the atmosphere for three years after the eruption, maintaining its effects for this period of time.

A significant increase in the CO_2 atmospheric concentration is noticed in all IPCC scenarios until the end of the XXI century (Figure 1). The different scenarios show that this increasing trend will continue and may even be intensified during the XXI century. The increasing concentration of CO_2 results in an inhibition of night-time longwave radiation cooling, and in an enhancement of day-time shortwave radiation heating. Consequently, an intensification of continental thermal lows is expected, which results in an increased zonal surface pressure gradient and intensification of alongshore wind in coastal regions and potentially in an increased persistence of coastal upwelling. The coastal upwelling can be an important aspect in climatic variability, as the cooling and consequent stabilization of atmospheric air in contact with upwelled waters can result in a cooler or not so warm future climate in upwelling adjacent coastal regions, even in a global warming IPCC scenario. It is noted that, so far, due to the low resolution of the global models used to elaborate the IPCC reports, the impact of coastal upwelling on the regional climate has not been taken into account in the IPCC scenarios.

1.2 Objectives

This thesis aims to improve the understanding of the evolution of coastal upwelling in the context of climate change. The analysis relies on sets of numerical simulations with a regional ocean numerical model and a coupled atmosphere-ocean model, and will address two separate questions: (1) what trends are to be expected in the Iberian upwelling from global warming? (2) How will feedback mechanisms, introduced by coupling the ocean and atmosphere, impact the Iberian coastal upwelling simulations?

Atmospheric data from recent decades analyzed by ECMWF and NCEP during their reanalysis projects will be here used together with ocean and coupled atmosphere-ocean models to address the above questions. The simulation results are compared against available observations, looking for simulated regional patterns of change consistent with local and remote sensing datasets. Global future climate scenarios, downscaled to the European region during the “Prudence” project, are used to force regional ocean simulations of the Iberian western coast, to assess the impact of climate change on the

coastal upwelling. The impact of ocean surface waves on the SST and surface atmospheric temperature will also be assessed with a coupled ocean-atmosphere-wave model.

1.3 Thesis layout

The following chapter presents a summary of the state of the art of coastal upwelling studies. The third chapter presents a description of the setup of the numerical models used in the study, and of the different databases required for initial and boundary conditions in the computational domain used in each simulation. Chapter four presents results of regional ocean simulations for the ERA-40 (1961-2001) and ERA-Interim (1989-2008) periods, using reanalysis data as forcing conditions for the ocean model. Chapter five does a similar analysis in the context of a climate change scenario (scenario A2 from IPCC-AR4), using atmospheric forcing data from simulations performed by the RACMO regional climate model within project "Prudence". Chapter six introduces a coupled atmosphere-ocean-wave model and discusses the impact of key atmospheric and oceanic variables from the three modeled systems on the coastal upwelling. In the last chapter, a summary of the main conclusions of each chapter is presented and some ideas for future work related to the coastal upwelling phenomena research are suggested.

Chapter 2 **Introduction**

2.1 **The Canary Current Upwelling System**

There are four main coastal upwelling ecosystems in the World Oceans: the California and Humboldt Current ecosystems, in the northern and southern eastern Pacific, and the Canary and Benguela current ecosystems in the northern and southern eastern Atlantic. The geographic location of those systems is presented in Figure 2, showing the mean chlorophyll-a surface concentration distribution for the period 1998-2007.

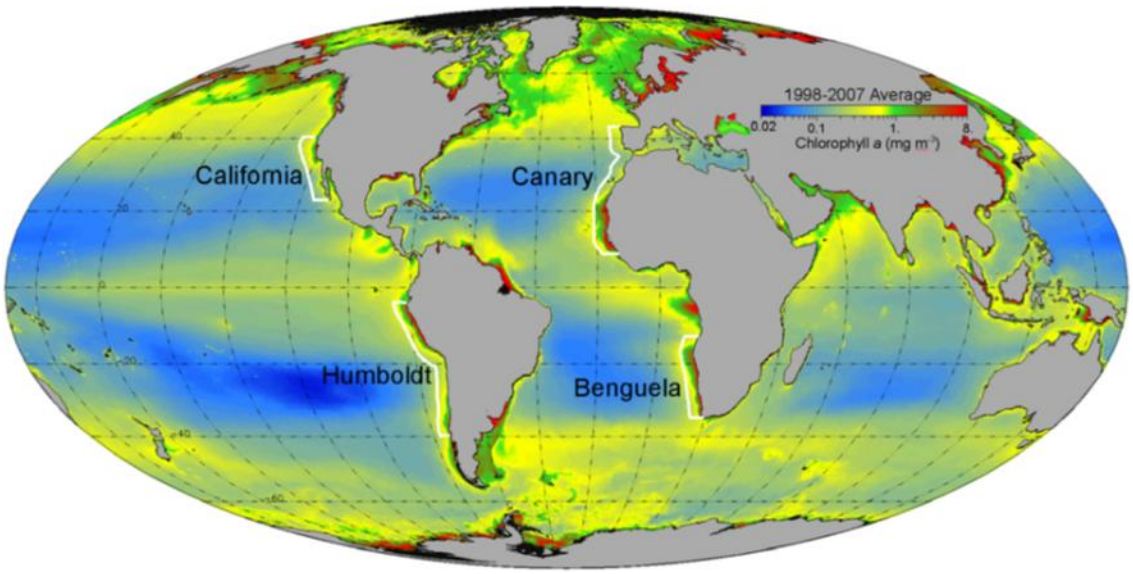

Figure 2 Geographic locations of the four main coastal upwelling ecosystems in the World Oceans, with the mean distribution of chlorophyll-a surface concentration for the period 1998-2007 (courtesy of H. Demarcq, IRD, France).

The four coastal upwelling ecosystems have in common the fact of having an anticyclone on its western side over the ocean, and a depression of thermal origin on the eastern side over the continent (Bakun, 1990). The presence of the quasi-stationary counter-rotating atmospheric circulation systems around the upwelling regions gives rise to northerly wind in the Northern Hemisphere and southerly wind in the Southern Hemisphere, originating horizontal divergence in the coastal upper ocean layers due to Ekman transport. The upwelling regions are characterized by cyclonic wind stress curl, typically, in the first 200 km off the coast (distance where the maximum wind stress is usually observed). In the zone offshore from the zone of maximum wind stress, an anticyclonic wind stress

curl region is normally observed, implying a convergence zone in the upper ocean and consequently downwelling (Bakun and Nelson, 1991).

The Canary current upwelling ecosystem extends from the north-western extreme of the Iberian Peninsula until the Senegal coast. The northern and southern limits of this system vary seasonally according to the local meridional surface wind. This ecosystem is characterized by different hydrological and dynamical characteristics along its meridional extension. For this reason, Aristegui et al. (2009) divided this ecosystem into six sub-regions. A southernmost region between parallels 12 °N and 21 °N, where freshwater runoff assumes importance in the coastal regime due to the outflow of several rivers in the region and a second region between parallels 21 °N and 33 °N off the Mauritanian–Senegalese coast, south of Cape Blanc, that is defined in the north by the separation of the Canary Current from the coast and in the south by the southern limit of the winter upwelling favorable winds. A third region, that comprises the Moroccan and Western Sahara coasts between Cape Sim and Cape Blanc, characterized by year-round upwelling. A fourth region, that corresponds to the Gulf of Cadiz, delimited by parallels 33 °N and 37 °N, unfavorable to upwelling occurrence due to the coastline orientation, as noted by Nykjaer and Van Camp (1994), who reported, from an analysis of ten years of satellite sea-surface temperature data, the absence of upwelling in the region. A fifth region, off western Iberia, that comprises the Portuguese coast and a sixth region, the northernmost one, corresponding to the Galician coast, influenced by freshwater outflow due to the presence of the Rias. The influence of freshwater is noted along the entire western Iberian coast but its importance decreases southwards and it is highly seasonal. Off the Portuguese coast the main sources of freshwater are the rivers Douro, Mondego and Tagus.

Off the western Iberian coast, the upwelling phenomena usually occur during the summer season (Ambar and Dias, 2008; Wooster et al., 1976; Fraga 1981; Tenore et al., 1984; Blanton et al., 1984, Alvarez-Salgado et al., 1993; Perez et al., 1995; Gomez-Gesteira et al., 2006), due to the geographic location of the Azores anticyclone (Bakun and Nelson, 1991) and the presence of the Iberian thermal depression. During the others seasons this process is not normally observed, although some sporadic events have been noticed as referred by Santos et al. (2004) , Alvarez et al. (2003), and deCastro et al. (2006, 2008).

In this thesis only the northern limit of the Canary current ecosystem that encloses the Portuguese and Galician western coasts will be addressed.

The first upwelling studies in the Canary current upwelling ecosystem region were conducted in the mid-1970s by Hughes and Barton (1974a, b) and were based on the analysis of hydrological data obtained from the RRS (Royal Research Ship) “Discovery” cruises in the north-western Africa region. In these studies, some of the main characteristics of coastal upwelling were already noticed. For

instance, these authors observed the presence of a poleward undercurrent over the continental slope and also noted that upwelling appeared to be more intense off the main capes, namely Cape Blanc and Cape Bojador. A few years later, Barton et al. (1977) using data from an array of buoys and current meters, also off the northwest Africa region, reported a two-layer flow regime during upwelling events, with a zonal shoreward undercurrent and an upper offshore layer.

Off the western Iberia coastal region, Fiuza (1983), based on remotely sensed surface thermography, observed that coastal upwelling has a strong seasonality with most of the events occurring during the summer season.

Like all major upwelling regions, the Canary current ecosystem is characterized by a rich mesoscale structure in the transition zone between the coastal upwelling region and the open ocean. The interaction between cool, nutrient-rich upwelling waters and warmer, oligotrophic offshore waters is governed by mesoscale activity in the form of filaments, eddies and island wakes (Barton et al., 1998). Off the western Iberian coast, one observes the persistence of intense upwelling filaments off the main capes, namely Cape Finisterre in the northern limit of western Iberian coast, Cape Carvoeiro in the central region and Cape St. Vicente on the southern limit of western Iberia Peninsula coast. The persistence of filaments off the main capes is thought to be related with the interaction of the near-surface ocean current with topographic features and/or connected with orographic effects in the surface wind stress field, as capes seem to induce an increased cyclonic surface wind stress curl in the region nearby (Haynes et al., 1993). These ocean filaments exhibit enhanced turbulence values in its boundaries, as noted by Barton et al. (2001).

2.2 Basic upwelling dynamics

In the following paragraphs it is made a brief description of the expected ocean dynamical behavior during a coastal upwelling event, and of the basic equations that describe this behavior, namely within the upper ocean boundaries layer.

The persistent northerly surface wind blowing along the western Iberian coast gives origin to coastal upwelling, characterized by offshore Ekman transport in the upper ocean layers, which implies the formation of a strong density front where the thermocline upwells to the surface and the presence of an associated along-front equatorward jet-like flow (Peliz et al., 2002; Aristegui et al., 2009). Simultaneously, the sea level near the coast is lowered due to the convergence of upper ocean layers in the offshore region, building a zonal gradient of the sea surface height contributing to the onset of the

above-mentioned geostrophic southward flow. The latter weakens with depth and usually becomes poleward near the seafloor over the continental slope.

In a zonal cross-section, seen from the south (Figure 3), the along-coast ocean currents are represented by the tail of an arrow (⊗), indicating northward flow, or by its tip (⊙), indicating southward flow. In this figure the dashed blue lines represent the mean depth of the Ekman and benthic boundary layers, the green zone represent the upwelled pycnocline, the grey arrows represent the offshore transport within the surface Ekman layer, and the dark arrows represent the deep onshore transport.

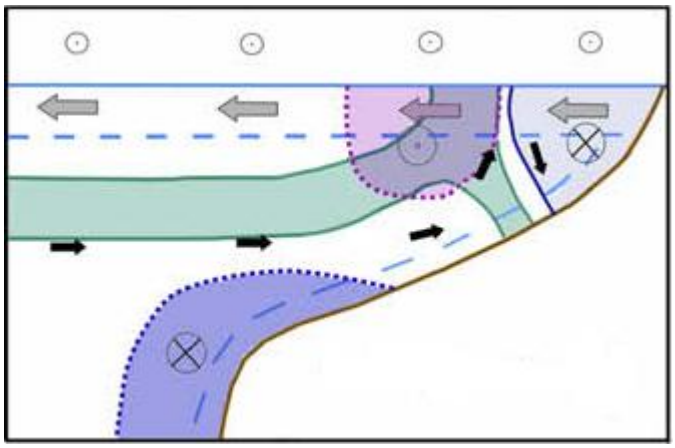

Figure 3 Sketch of the mean circulation off the western Iberian coast during the upwelling season (Aristegui et al., 2009).

The poleward undercurrent flow, represented by the dark blue color in Figure 3 is largely forced by the interaction between the meridional density gradient and the continental slope and shelf (Huthnance, 1984). In addition to this poleward undercurrent, Peliz et al. (2002) also noticed a second inner shelf counter-flow characterized by a northward current, represented in Figure 3 by the light blue inner shelf region. According to the authors it has origin in the response to the strong offshore deflection of the upwelling current and to the presence of the WIBP (Western Iberia Buoyant Plume), which comprises low salinity surface waters present on the inshore side of the upwelling front originating from the rivers runoff along the western Iberian coast. Also according to the authors, the WIBP has a strong seasonal cycle, with a weaker intensity in summer due to lower river runoff. Within the inner-shelf region the Ekman and bottom boundary layers overlap, the flow is strictly parallel to the coast, the cross-shore transport vanishes, and the frictional effects due to wind and bottom stresses compensate each other and maintain the flow in the alongshore direction throughout the entire water column. This area is, typically, more extended in wide and shallow continental regions, and creates an inner ocean

front which provides retention for biological material (e.g. fish eggs and larvae) in the highly productive near-shore environment (Estrade et al., 2008). In the region to the west of the inner-shelf front, the main upwelling front and associated southward jet are present. This is the region where the pycnocline upwells to the surface and is represented in purple in Figure 3.

Contrary to open-ocean upwelling, coastal upwelling is not only due to diverging Ekman transport, but also due to Ekman pumping. While the near-shore surface wind drop-off favors the Ekman pumping mechanism, the stronger near-shore winds (i.e. smooth drop-off) favors coastal upwelling due to divergence in the upper ocean layers (Capet et al., 2004).

Figure 4 depicts the ocean surface Ekman layer and its respective hodograph.

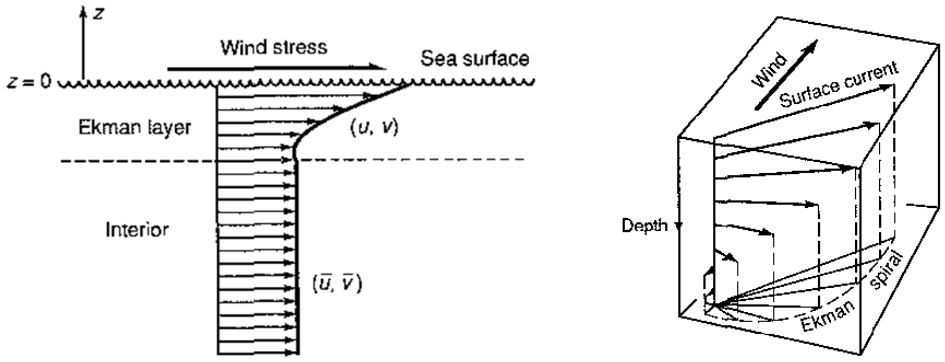

Figure 4 Scheme of the surface Ekman layer generated by surface stress on the ocean surface (Cushman Roisin, 1994).

Neglecting pressure gradients, the zonal and meridional momentum in the upper ocean Ekman layer satisfy the following equations:

$$-f(v-\bar{v}) = \upsilon \frac{\partial^2 u}{\partial z^2} \quad (1a)$$

$$-f(u-\bar{u}) = \upsilon \frac{\partial^2 v}{\partial z^2} \quad (1b)$$

In the above equations, u and v are the zonal and meridional currents within the Ekman surface layer and $\bar{u}$ and $\bar{v}$ are the zonal and meridional currents in the ocean interior, f is the Coriolis parameter, υ is the ocean kinematic viscosity and z is the vertical coordinate, as represented in Figure 4.

To solve the above equations the following boundary conditions at the ocean surface ($z = 0$) are taken into account:

$$\rho_0 \upsilon \frac{\partial u}{\partial z} = \tau_x \tag{2a}$$

$$\rho_0 \upsilon \frac{\partial v}{\partial z} = \tau_y \tag{2b}$$

In the lower boundary, toward the ocean interior ($z \to -\infty$), the considered boundary conditions are $u = \bar{u}$ and $v = \bar{v}$.

In equations (2a) and (2b), ρ_0 is the reference density, τ_x and τ_y are respectively the zonal and meridional wind stress.

The solution to the above equations is:

$$u = \bar{u}\left(1 - e^{-z/d} cos\left(\frac{z}{d}\right)\right) - \bar{v} e^{-z/d} sin\left(\frac{z}{d}\right) \tag{3a}$$

$$v = \bar{u} e^{-z/d} sin\left(\frac{z}{d}\right) + \bar{v}\left(1 - e^{-z/d} cos\left(\frac{z}{d}\right)\right) \tag{3b}$$

From equations (3a) and (3b) it can be noted that the wind driven flow is inversely proportional to the Ekman depth, that takes the form:

$$d = \sqrt{\frac{2\upsilon}{f}} \tag{4}$$

Near the surface (z $\to$ 0) the downstream and transverse components have approximately the same value (u $\cong$ v), thus implying that the velocity is 45° to the right of the interior velocity.

The vertical velocity in the interior of the Ekman layer, usually named Ekman pumping, is computed by vertical integration of the continuity equation taken into account the boundary conditions $w(z = 0) = 0$ at the ocean surface and $w(z \to \infty) = \bar{w}$ at the ocean interior boundary of the Ekman layer:

$$\bar{w} = -\int_0^{\infty} \left(\frac{\partial u}{\partial x} + \frac{\partial v}{\partial y}\right) dz = \frac{d}{2}\left(\frac{\partial \bar{v}}{\partial x} - \frac{\partial \bar{u}}{\partial y}\right) = \frac{d}{\rho_0 f} \nabla^2 \bar{P} \qquad (5)$$

In the last member of the above expression, P represents pressure and the geostrophic approximation was considered. Relation (5), shows that the Ekman pumping velocity increases with the vorticity, and decreases with latitude (decreasing *f*).

2.3 Coastal upwelling indices

Since the first coastal upwelling studies, researchers have tried to use an index to determine the intensity, frequency and duration of this coastal phenomenon. One of the first coastal upwelling studies was conducted during the 1970's by the Pacific Fisheries Environmental Laboratory (PFEL). At that time, daily and monthly upwelling indices were generated at fifteen geographic locations along the west coast of North America. The first set, beginning in 1967, included daily and weekly averages of six-hourly upwelling indices estimated from six-hourly synoptic pressure fields. The second set was extended back to 1946 and derived from monthly mean pressure fields. The zonal and meridional wind components were computed taken into account the geostrophic approximation:

$$u_g = -\frac{1}{f \rho_a R} \frac{\delta P}{\delta \phi} \qquad (6a)$$

$$v_g = \frac{1}{f \rho_a R \cos \phi} \frac{\delta P}{\delta \lambda} \qquad (6b)$$

Equations (6a) and (6b) express the geostrophic wind, where $f = 2\Omega sin\theta$ is the Coriolis parameter (Ω is the Earth's angular velocity), ρ_a is the air density and R is the Earth mean radius, P is the surface pressure, ϕ is latitude, and λ is longitude. The ocean Ekman transport was then computed as:

$$\vec{M} = \frac{1}{f}\vec{k} \times \vec{\tau} \quad (7)$$

where τ is the wind stress computed with expression:

$$\vec{\tau} = \rho_a C_d |\vec{v}| \vec{v} \quad (8)$$

in which C_d is an empirical drag coefficient, $\vec{v}$ is the computed near surface wind vector with magnitude $|\vec{v}|$.

More recently, Alvarez et al. (2008) computed an upwelling index for the western Iberian coast based on surface wind data from the QuikSCAT sensor. These authors computed the zonal and meridional Ekman transport, respectively Q_x and Q_y, for the 2000-2006 period, following the relations:

$$Q_x = \frac{\rho_a C_d}{\rho_w f}(U^2 + V^2)^{1/2} V \quad (9a)$$

$$Q_y = -\frac{\rho_a C_d}{\rho_w f}(U^2 + V^2)^{1/2} U \quad (9b)$$

In equations (9a) and (9b), U and V are the zonal and meridional components of the wind speed at 10 m, the other symbols represent the same variables indicated before. The upwelling index (U_I) was then computed as the Ekman transport perpendicular to the coastline:

$$U_I = -\sin(\theta)\, Q_x + \cos(\theta) Q_y \quad (10)$$

In equation (10) $\theta = \frac{\pi}{2} + \varphi$ where φ is the angle of the unitary vector perpendicular to the coastline pointing landward (Gomez-Gesteira et al., 2006).

A different kind of coastal upwelling index, that is also one of the most commonly applied, consists in a simple SST difference between a point close to the coast and a point located far enough away from the coast as not to be affected by the upwelling front or filaments. The SST data used to define the

upwelling index is normally retrieved from satellite sensors. With the development of remote detection technologies verified in the last decades, the temporal and spatial resolution of available observational data over the oceans has significantly increased.

SST data derived from AVHRR (Advanced Very High Resolution Radiometer) sensor is available since the beginning of the 1980's. This sensor works in the infrared band, which has the disadvantage of being affected by cloud cover and the presence of fog, both leading to a sparse database particularly in coastal upwelling regions during the summer season (when foggy days and stratus clouds are frequently observed). Recently, the AMSR-E (Advanced Microwave Scanning Radiometer for EOS) sensor on-board the Aqua satellite and the TMI (Trmm Microwave Imager) sensor on-board the TRMM (Tropical Rainfall Measuring Mission) satellite started to retrieve SST data. These two sensors work in the microwave frequency band, which has the advantage of not being affected by the presence of clouds. On the other hand, those sensors have the disadvantage of not retrieving SST data under large precipitation conditions and in regions within 50 km from the coast, making them less appropriated for upwelling studies. Moreover, the TMI sensor only gives SST values between the latitudes 40°S and 40°N. In addition to SST retrieved from satellite sensors, one can also obtain SST data from local observations, but these are normally only available close to the coast, in discrete points and with a poor temporal resolution.

2.4 **Inter-annual variability and trends of the upwelling regime**

During the last years, coastal upwelling trends have been observed in the four main coastal upwelling ecosystems based on surface wind and SST data.

Demarcq (2009) analyzed SST data for the period 1985-2007 from the Pathfinder database and observed a slightly lower SST trend in upwelling regions (0.42°C per decade) than elsewhere in the continental margins (0.56°C per decade), which can possibly be interpreted as a consequence of an increase in the upwelling intensity. However, the SST trends computed by Demarcq (2009) are not equal among the four upwelling ecosystems. Lower SST trends were observed in the southern Pacific and Atlantic ecosystems (<0.2°C per decade), while a stronger SST trend was observed in the Canary and California ecosystems (>0.5°C per decade). It is here noted that the spatial structure of those trends within each ecosystem was not analyzed. From QuikSCAT wind data for 2000-2007, the author computed a mean positive trend in meridional wind intensity of 0.12 $m.s^{-1}.decade^{-1}$ in the four main

upwelling regions. This intensification of the meridional wind component seems to agree with atmospheric global models and data reanalyses that indicate an intensification and expansion of the Hadley cell in recent decades (Mitas and Clement, 2006; Seidel et al., 2008). This is also in agreement with Bakun (1990), who based on individual wind reports from ships at sea, for the 1970-1985 period, showed an intensification of the along-coast wind in the four main eastern boundary upwelling ecosystems.

Concerning the western Iberian upwelling ecosystem, the conclusions with respect to coastal upwelling trends in the last decades are not in complete agreement among the different published studies. Alvarez et al. (2008), using Ekman transport data, computed from a PFEL wind database for the 1967-2006 period (with 1° resolution, approximately), observed a weakening in upwelling intensity during most of the year (with the exception of February, June and July) taking into account the mean Ekman transport value at six points equally spaced along the western Iberian coast. The authors also noted a stronger variability in the upwelling index in autumn and winter, when compared to spring and summer.

With regard to studies of upwelling trends some authors find that stronger Ekman transport (computed from surface winds) occurs one to two month earlier than when more upwelling events are observed in the satellite sea surface temperature maps (Alvarez et al., 2010, Fiuza et al., 1982; Nykjaer and VanCamp, 1994; deCastro et al., 2008). This time lag can lead, when analyzing only wind data, to inaccurately identifying the months when coastal upwelling events occur more frequently.

In a more recent study, Alvarez et al. (2010), also using Ekman transport data provided by PFEL but this time just for the western and northern Galician coasts, noticed that the number of upwelling favorable days off the western Galician coast, identified by the upwelling intensity threshold $UI_{ET} > 16$ $m^3.s^{-1}.km^{-1}$ (this threshold corresponds to winds with intensity lower than 1 $m.s^{-1}$ to remove calms), have been decreasing during the 1967-2008 period, while an increasing trend in the yearly mean computed upwelling index ($UI_{ET} = -Q_x$) was observed (Q_x represent the zonal Ekman transport values). To quantify the real impact of coastal upwelling these authors computed a new variable expressed by:

$$U_{imp} = \frac{\sum_{i=1}^{N} n_i < UI_{ET} >}{N_d} \qquad (11)$$

The upwelling impact variable (U_{imp}) computed using equation (11) takes into account the upwelling intensity (UI_{ET}), n_i the number of consecutive days under upwelling favourable conditions considering

ni≥4 and the number of days under upwelling favorable conditions (N_d). No significant trend was observed in this variable, with just a slight increase being noticed by the authors.

Using wind data from the Portuguese Institute of Meteorology and a linear regression model, Lemos and Pires (2004) found a progressive weakening of the upwelling regime along the western Portuguese coast from 1941 to 2000.

More recently, Narayan et al. (2010) noticed an increasing trend in the intensity of coastal upwelling off the northwestern African coast during the period 1960-2001. Their analysis was based on the meridional wind stress and SST data from the COADS (Comprehensive Ocean-Atmosphere Data Set) database. These authors, as Bakun (1990), related the coastal upwelling increasing trend with the global warming due to higher greenhouse gases concentration. As a consequence of the warming, an intensification of the thermal depression on the continental side of the Canary current upwelling ecosystem, and consequent intensification of the northerly winds along the western Iberian coast, was suggested.

From analyzing satellite-derived SST time series for the period 1985-2008 Santos et al. (2005) found evidence in SST fields of coastal upwelling intensification off the western Iberian coast from 1992 onwards. Relvas et al. (2009) also reported a weaker warming trend off the southern part of western Iberian coast when compared with that farther north. This seems to indicate an intensification of coastal upwelling in the southwestern Iberian coast since 1985.

A study by McGregor et al. (2007) looked at longer term changes in upwelling off northwestern Africa, and its impact on the sediment record, and concluded that significant changes may have occurred on the decadal to centennial scales.

When comparing different wind databases, Narayan et al. (2010) identified significant discrepancies for the 1960-2000 period between the COADS, NCEP/NCAR and ECMWF/ERA-40 meridional wind data along the northwestern African coast. The COADS and ERA-40 databases, for instance, show an increasing trend in the wind intensity while the NCEP/NCAR database shows a decreasing tendency. Even comparing the COADS and ERA-40 databases, although both indicate a positive trend, the trend in the COADS database is 3 times larger than the one in the ERA-40 database.

Chapter 3 **Methodology**

3.1 **Advantages of using numerical models**

The development of numerical models and computational processing capabilities during the last decades has permitted the numerical simulation of the atmosphere and ocean dynamical and thermal fields with an increasing temporal and spatial resolution. In the particular case of coastal upwelling studies, the use of numerical models allowed to better identify coastal upwelling events, when compared with studies based only on SST or wind observational data.

In purely observational studies, it is likely that some events can be misinterpreted as upwelling, since observed cool coastal SST can be due to mechanisms other than coastal upwelling. For instance, the cold coastal temperatures can be caused by a meridional advection of cold ocean surface waters or by an offshore advection of low temperature continental air over the ocean. The latter process cools the ocean surface by transferring heat across the atmosphere-ocean interface. This situation can possibly occur, more frequently, during the autumn and winter months, when the surface air temperature over the continents decreases faster than over the ocean due to different thermal capacities of both fluids. In both of the above cases, the lower SST observed in coastal waters is not due to the vertical advection of deeper cold water caused by a coastal upwelling event.

There are also some issues that should be taken into account, when studying coastal upwelling based on wind data only. The vertical stratification and dynamical field of the coastal ocean off western Iberian varies during the year. As a result, wind with a specific intensity and direction will have different effects on the SST field, depending on the season of the year.

In short, when analyzing separately SST or wind data there may be cold SST days at the coast, that are misinterpreted as upwelling events. To clarify the analysis it is essential to look at both the coastal dynamical and thermal fields. Numerical models allow the simultaneous analysis of all relevant fields, including sea surface height, ocean currents, temperature and salinity at a convenient vertical and horizontal grid resolution. This enables the computation of an upwelling index that takes into account both the ocean dynamical and thermal properties and is more likely to properly identify cases where cold coastal SSTs are due to coastal upwelling events. Another important advantage in the use of numerical models is their capability to simulate future climate scenarios, as those presented in IPCC reports.

But numerical models also have some disadvantages. When interpreting the output of numerical models, it is important to keep in mind that the numerical methods applied to solve the dynamic and thermodynamic equations of the ocean and atmosphere always have associated errors. These errors

often lead to significant deviations from observations. Errors in numerical models can be due to the lack of accuracy of the imposed initial and boundary conditions or to model deficiencies (for instance, lack of proper physical parameterizations). Because of their individual limitations and strengths, numerical models, satellite and in situ observations all play an important and complementary role in coastal upwelling studies.

3.2 Model description

3.2.1 The Regional Ocean Modeling System (ROMS)

The ROMS numerical model is being developed at the University of Rutgers, USA, and is presently one of the most used numerical models in coastal ocean research. As an open source model its code is currently the result of numerous contributions from world-wide researchers. There are presently three main versions of the ROMS model: one maintained at UCLA (University of California, USA), one at IRD (Institut de Recherche pour le Dévelopement, France) and the main one at Rutgers University. The results here presented were obtained with the latter version.

ROMS has been successfully applied to the four major coastal upwelling ecosystems referred in Chapter 2. In the western Iberian region, Oliveira et al. (2009) used the model and satellite data to show the main regional patterns of coastal spatial and temporal SST variability, namely the strong along-slope flows, the development of filaments, separated jets and shadow areas downstream of the main capes, frontal-scale instabilities and the rapid onset of coastal counter-currents along the inshore zone during wind relaxation phases. For this upwelling ecosystem, Peliz et al. (2007b) also used ROMS with a lagrangian sub-model that includes advection, diffusion, and diel vertical migration, to simulate crab larvae dispersal, which resulted in a good match between model results and observations.

For the California current upwelling ecosystem, Penven et al. (2006) made use of a one-way grid nesting technique in ROMS to simulate upwelling phenomena at a higher resolution in the coastal region, where the dominant spatial scales are typically smaller than those observed in the open ocean. Also in the California current ecosystem, Capet et al. (2004) applied the model to show the impact of the nearshore wind spatial structure on the patterns of the upwelling circulation, surface temperature, and biogeochemical processes.

For the Benguela current ecosystem, Penven et al. (2001) and Blanke et al. (2002) showed the ability of the model to correctly simulate upwelling events in the region by obtaining a fair degree of correlation between the model output and local observations.

For the Humboldt current upwelling ecosystem, Penven et al. (2005) showed that ROMS model is able to reproduce the known dynamics of the region, namely, the equatorward Peru coastal current, the Peru-Chile undercurrent and the Peru-Chile countercurrent. Also Echevin et al. (2008) used ROMS to study the southern Indian Ocean upwelling ecosystem and noted that the highest chlorophyl concentration is observed in austral summer and lowest values during austral winter, in agreement with satellite and in situ observations.

3.2.1.1 ROMS equations

In order to made a brief description of the numerical model used in this study, from which most of the results presented here were retrieved, in the following lines are presented some of the main equations solved numerically by ROMS during the simulations.

The ROMS numerical model is a free-surface, terrain-following, primitive equations model, that uses the hydrostatic approximation (the vertical pressure gradient balances the buoyancy force) and Boussinesq approximation (density variations are neglected in the momentum equations except when their contribution to the buoyancy force in the vertical momentum equation are taken into account). In the hydrostatic approximation, the vertical momentum equation is reduced to:

$$\frac{\partial P}{\partial z} = -\rho g \tag{12}$$

where P represents pressure, z the vertical coordinate, ρ density and g is the acceleration due to gravity.

The horizontal momentum equations in the zonal (x) and meridional (y) directions are expressed by the following equations:

$$\frac{\partial u}{\partial t} + \vec{v}.\nabla u - fv = -\frac{\partial \phi}{\partial x} - \frac{\partial}{\partial z}\left(\overline{u'w'} - v\frac{\partial u}{\partial z}\right) + F_u + D_u \tag{13a}$$

$$\frac{\partial v}{\partial t} + \vec{v}.\nabla v + fu = -\frac{\partial \phi}{\partial y} - \frac{\partial}{\partial z}\left(\overline{v'w'} - v\frac{\partial v}{\partial z}\right) + F_v + D_v \qquad (13b)$$

where u and v are, respectively, the zonal and meridional components of currents, u', v' and w' represent small-scale fluctuations of the three current components and f is the Coriolis parameter ($f = 2\Omega sin\theta$) , where Ω is the Earth's angular velocity $\left(\Omega = \frac{2\Pi}{T}\right)$, T is the sidereal period, θ is the latitude, ϕ is the dynamical pressure, computed as $\phi = \frac{P}{\varrho_0}$. In the above equations an overbar represents a time average and F and D are, respectively, the forcing and diffusive terms.

The advection-diffusion equation for the tracers (temperature and salinity) is expressed as:

$$\frac{\partial C}{\partial t} + \vec{v}\nabla C = -\frac{\partial}{\partial z}\left(\overline{C'w'} - v_\theta\frac{\partial C}{\partial z}\right) + F_c + D_c \qquad (14)$$

where C is a scalar concentration field.

Considering the ocean an incompressible fluid, the continuity equation is expressed by:

$$\frac{\partial u}{\partial x} + \frac{\partial v}{\partial y} + \frac{\partial w}{\partial z} = 0 \qquad (15)$$

The model equations are discretized over a variable topography using a stretched, terrain-following, vertical coordinate. As a result, each grid cell has a different level thickness and volume depending on the local depth. The model state variables are staggered on an Arakawa C-grid, as shown in Figure 5.

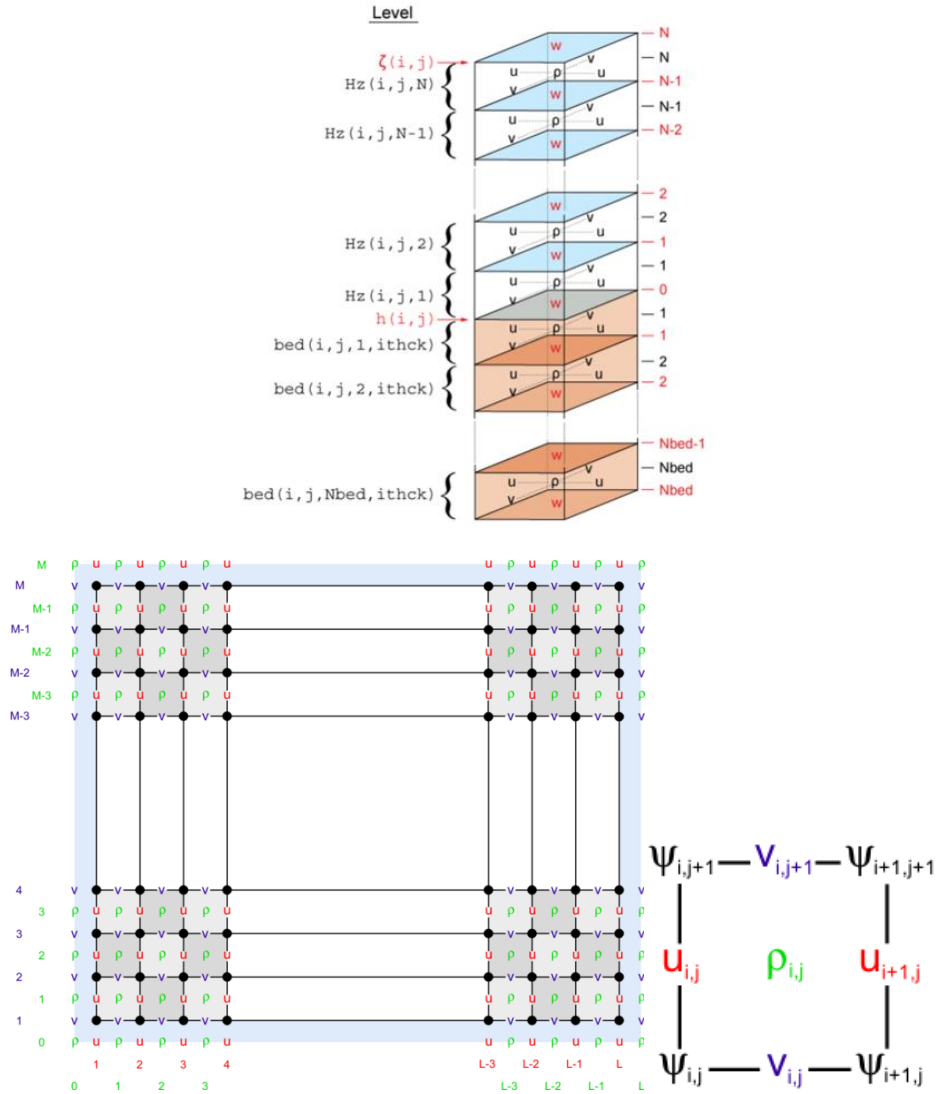

Figure 5 Sketches of the Arakawa-C grid used in ROMS (figures retrieved from the wikiroms website).

In each computational grid cell, the free-surface, density, temperature and salinity variables are calculated at the center of the cell, whereas the zonal and meridional horizontal velocities are located, respectively, at the west and south edges of the cell, and the vertical velocities are calculated at upper and lower edges of each computational cell.

ROMS is a split-explicit ocean model, where short time steps are used to advance, explicitly, the surface elevation and barotropic momentum equations (thus called barotropic time step), and a larger time step (called baroclinic) is used to advance the temperature, salinity, and baroclinic momentum equations.

The 3D and 2D equations are time discretized using a Leap-Frog predictor and a three-time Adams-Moulton corrector method. For advection schemes ROMS has various options, like second and fourth order centered differences and a third order, upstream biased, scheme.

In ROMS, turbulence is computed explicitly for parameterization of sub-grid scale vertical mixing processes. A two equations turbulence scheme, named GLS (Generic Length Scale), developed by Warner et al. (2005), was used in the simulations presented here.

ROMS parameterize the turbulent fluxes at the air-sea interface following the COARE 3.0 algorithms presented in Fairall et al. (2003). These algorithms were formulated based on ship, buoy, aircraft, satellite and model data.

The UNESCO (United Nations Educational, Scientific and Cultural Organization) non-linear equation of state derived by Jackett and McDougall (1995) is used to compute in situ density from salinity and potential temperature and pressure values. It should be noted that the new equation of state TEOS-10 was recently implemented in the ROMS code but it was not used in the results presented in this thesis in order to maintain all the ROMS simulations here presented consistent. The new equation of state is based on a Gibbs function formulation from which all thermodynamic properties of seawater (density, enthalpy, entropy and sound speed) can be derived in a thermodynamically consistent manner.

A complete description of the model equations and of the numerical methods applied to solve them is not the scope here and can be found in Shchepetkin and McWilliams (2003, 2005, 2009) and Haidvogel (2000).

3.2.1.2 ROMS boundary conditions

The lateral boundary conditions most frequently used in the ROMS are the radiation and nudging conditions (Marchesiello et al., 2001).

The radiation condition for a generic prognostic model variable ϕ is represented by:

$$\frac{\partial \phi}{\partial t} + C_x \frac{\partial \phi}{\partial x} + C_y \frac{\partial \phi}{\partial y} = 0 \qquad (16)$$

where C_x and C_y are, respectively, the zonal and meridional components of the phase speed, that are computed as follows:

$$C_x = -\frac{\partial\phi}{\partial t}\frac{{}^{\partial\phi}/_{\partial x}}{\left({}^{\partial\phi^2}/_{\partial x^2}\right)+\left({}^{\partial\phi^2}/_{\partial y^2}\right)} \quad (17a)$$

$$C_y = -\frac{\partial\phi}{\partial t}\frac{{}^{\partial\phi}/_{\partial y}}{\left({}^{\partial\phi^2}/_{\partial x^2}\right)+\left({}^{\partial\phi^2}/_{\partial y^2}\right)} \quad (17b)$$

If the computational boundary has an outward propagation for a prolonged time, the predicted boundary values may evolve to values quite different from the imposed boundary conditions; when an inward propagation is verified, numerical instabilities may arise at the boundaries (Marchesiello et al., 2001). To overcome this problem, an additional term is added to the radiation boundary condition equation (see right hand side term below), thus applying a nudging condition:

$$\frac{\partial\phi}{\partial t} + C_x\frac{\partial\phi}{\partial x} + C_y\frac{\partial\phi}{\partial y} = -\frac{1}{\tau}(\phi - \phi^{ext}) \quad (18)$$

where,

$$\tau = \tau_{out} \text{ if } C_x > 0 \text{ (outward propagation)} \quad (18a)$$

$$\tau = \tau_{in} \text{ and } C_x = C_y = 0 \text{ if } C_x < 0 \text{ (inward propagation)} \quad (18b)$$

In equation (18) ϕ^{ext} represents the external data given as boundary conditions and τ_{in} *and* τ_{out} represent, respectively, the inward and outward relaxation timescales. Typically, the outward timescale has a much higher value than the inward timescale ($\tau_{out} >> \tau_{in}$). During outward propagation weak nudging prevents huge deviations and the over-specification problem, while during inward propagation a strong nudging is applied, although not too strong in order to avoid data-shock

problems. In addition to the radiation and nudging boundary conditions, a sponge layer is also usually applied. This sponge condition consists on imposing a lateral layer around the computational domain with an increased viscosity and diffusivity in order to reduce eventual boundary instabilities.

In the ROMS model the upper boundary conditions are expressed by the following expressions:

$$K_m \frac{\partial u}{\partial z} = \tau_s^x(x, y, t) \tag{19a}$$

$$K_m \frac{\partial v}{\partial z} = \tau_s^y(x, y, t) \tag{19b}$$

$$K_C \frac{\partial C}{\partial z} = \frac{Q_C}{\rho_0 c_P} \tag{19c}$$

where K_m is the vertical eddy viscosity, K_C is the vertical eddy diffusivity, and τ_s^x and τ_s^y are the zonal and meridional components of the surface wind stress and Q_C represents the surface concentration flux,

The vertical velocity on the ocean surface (w) is computed by:

$$w = \frac{\partial \varphi}{\partial t} \tag{20}$$

where φ is the height of the ocean free surface.

The bottom boundary conditions are expressed by:

$$K_m \frac{\partial u}{\partial z} = \tau_b^x(x, y, t) \tag{21a}$$

$$K_m \frac{\partial v}{\partial z} = \tau_b^y(x, y, t) \tag{21b}$$

$$K_C \frac{\partial C}{\partial z} = 0 \tag{21c}$$

$$-w + \vec{v}.\nabla h = 0 \tag{21d}$$

In the above equations τ_b^x and τ_b^y represent, respectively, the zonal and meridional components of the bottom stress. In equation (21d) w is the bottom vertical velocity and the other variables have the same meaning indicated above for the upper boundary conditions. The horizontal velocity components are constrained to accommodate a prescribed bottom stress that obeys the quadratic formulation of bottom friction.

As a free surface model, ROMS can gain or lose water through its computational lateral boundaries. In order to avoid cumulative volume errors, the barotropic inflow are uniformly adjusted at the open boundaries in a way that the total volume transport across the boundaries is balanced (Marchesiello et al., 2001).

The volume conservation condition is expressed by:

$$\frac{dV}{dt} = \frac{d}{dt}\left[\iiint_V \quad\right] dV = \iint_{S_b} \overrightarrow{u}.\vec{n}\, dS = \int_{L_b} h\vec{\overrightarrow{u}}\vec{n}\, dL \tag{22}$$

where $\vec{n}$ is the inward unitary vector, u the surface current and S_b and L_b are, respectively, the enclosed area and perimeter of the computational domain.

A normal velocity correction (u_c) is defined in order to obtain a new barotropic current expressed by

$$\overrightarrow{\overrightarrow{u_{new}}} = \vec{\overrightarrow{u}} - \overrightarrow{u_c}\vec{n} \tag{23}$$

So that the variation of total volume is only a result of physical sources and sinks of seawater (F), as expressed by

$$\frac{dV}{dt} = F = \int_{L_b} h\left(\vec{u} - \overline{u_c}\right).\vec{n}\, dL = \int_{L_b} h\vec{u}.\vec{n} dL - \int_{L_b} h\overline{u_c} dL \quad (24)$$

where $\overline{u_c}$ is the normal velocity correction, computed by:

$$\overline{u_c} = \frac{1}{S_b}\left(\int_{L_b} h\vec{u}.\vec{n} dL - F\right) \quad (25)$$

In this way the change of volume within the computational domain depends only on sinks and sources present inside the domain, as thermal expansion effects, precipitation, evaporation, river runoff and tidal fluxes, expressed by the F term.

3.2.2 The COAWST coupled ocean-atmosphere system

COAWST (Coupled Ocean-Atmosphere-Wave-Sediment Transport) is a coupled modeling system comprising three open source models (Figure 6): an oceanic model (ROMS), an atmospheric model (WRF) and a wave model (SWAN). To exchange properties between the different models the MCT (Model Coupling Toolkit) coupler is used. MCT allows the transmission and transformation of distributed data between component models (Larson et al., 2004; Jacob et al., 2005). Each model calls the MCT during execution to send and receive data. The coupled system COAWST is being developed at the USGS, USA. Warner et al. (2010) present a description of COAWST and show results of the system, when applied to a real case of hurricane Isabel, which stroke the United States eastern coast in the summer of 2003.

Within the COAWST system each model runs with its own grid, which can be common or different among them. In simulations with different spatial resolutions, in order to allow the models to exchange fields, the SCRIP (Spherical Coordinate Remapping Interpolation Package) code (Jones, 1998) is used to compute the interpolation weights. The weights are computed as a pre-processing step and then are read during initialization and used in the sparse matrix interpolation as described in Warner et al. (2008).

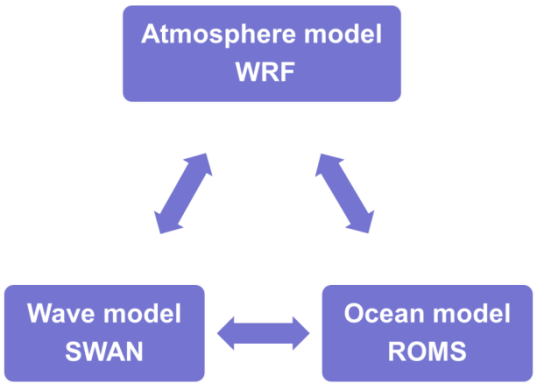

Figure 6 Numerical models that comprise the COAWST coupled system.

The WRF (Weather Research and Forecasting) atmospheric model is a widely used model in both operational weather forecasting and atmospheric research. The core equations of the WRF-ARW (Advanced Research WRF) version are the fully compressible, Eulerian and non-hydrostatic equations with a run-time hydrostatic option. The model is conservative for scalar variables and uses a terrain-following hydrostatic-pressure vertical coordinate, with the top of the model being a constant pressure surface. It uses an Arakawa-C horizontal grid. For time integration, second and third-order Runge-Kutta schemes can be used. For the spatial discretization, in both horizontal and vertical orientations, second to sixth order advection schemes can be applied. A detailed description of the WRF model can be found in Skamarock et al., (2008).

SWAN (Simulating WAves Nearshore) is a spectral wave model that simulates wind wave generation and propagation in coastal waters and includes the processes of refraction, diffraction, shoaling, wave–wave interaction and dissipation due to white-capping, wave breaking and bottom friction (Booij et al., 1999).

The wave model solves the action balance equation (26), expressed by Holthuijsen, (2008):

$$\frac{\partial N}{\partial t}+\frac{\partial c_x N}{\partial x}+\frac{\partial c_y N}{\partial y}+\frac{\partial c_\sigma N}{\partial \sigma}+\frac{\partial c_\theta N}{\partial \theta}=\frac{S_w}{\sigma} \qquad (26)$$

where $N(\sigma,h,x,y,t)$ is the action density spectrum, defined as the wave energy density (E) divided by the relative frequency ($N=\frac{E}{\sigma}$), a quantity that is conserved in the presence of currents. Parameter σ is the relative radian frequency (in a reference frame moving with the ocean current), θ is the direction normal to the wave crest, x and y are spatial coordinates and t is time. On the left-hand side

of (26) the group velocities in the x and y directions, respectively c_x and c_y represent the propagation of action density in space, the fourth term represents changes in relative frequency due to variations in depth and currents with a propagation speed c_σ in the frequency space, and the fifth term represents the depth and current-induced refraction with a speed c_θ in directional space. On the right-hand side the S_w term represents sources and sinks of wave energy density. The SWAN model allows input of temporal and spatially varying ocean currents and water level, and changes in bathymetry and bottom roughness.

The COAWST coupled system allows different configurations with the numerical models that comprise the system, as shown in Figure 7. In the configuration presented in case A, the WRF model is forced by a time varying SST that, for instance can be retrieved from an Optimally Interpolated SST database. In case B, the COAWST system consists of WRF coupled with ROMS. In this case, the ROMS model transfers the SST field to the WRF atmospheric model and the latter provides ROMS with surface wind, atmospheric pressure, relative humidity, surface air temperature, cloud clover, precipitation, and the shortwave and longwave net radiation. The configuration presented in case C corresponds to the fully coupled system WRF-ROMS-SWAN. In this case, the variables exchanged between WRF and ROMS are identical to those described for case B; the WRF model transmits to SWAN the surface wind field, while SWAN communicates to ROMS the significant wave height, the wave length, the wave direction, surface wave period, bottom wave period, the percentage of wave breaking, the wave energy dissipation and the bottom orbital period fields. In turn, ROMS provides SWAN with zonal and meridional surface currents, sea surface elevation and bathymetry. The SWAN model communicates to WRF the significant wave height and wave length fields.

Within COAWST, the ROMS ocean model uses the COARE algorithms to compute the ocean surface stress and the ocean surface net heat and freshwater fluxes (Fairall, et al., 1996, 2003). As an alternative to COARE algorithms, it is possible to use in ROMS the momentum and heat fluxes computed by WRF, allowing both models to use identical fluxes at the atmosphere-ocean interface.

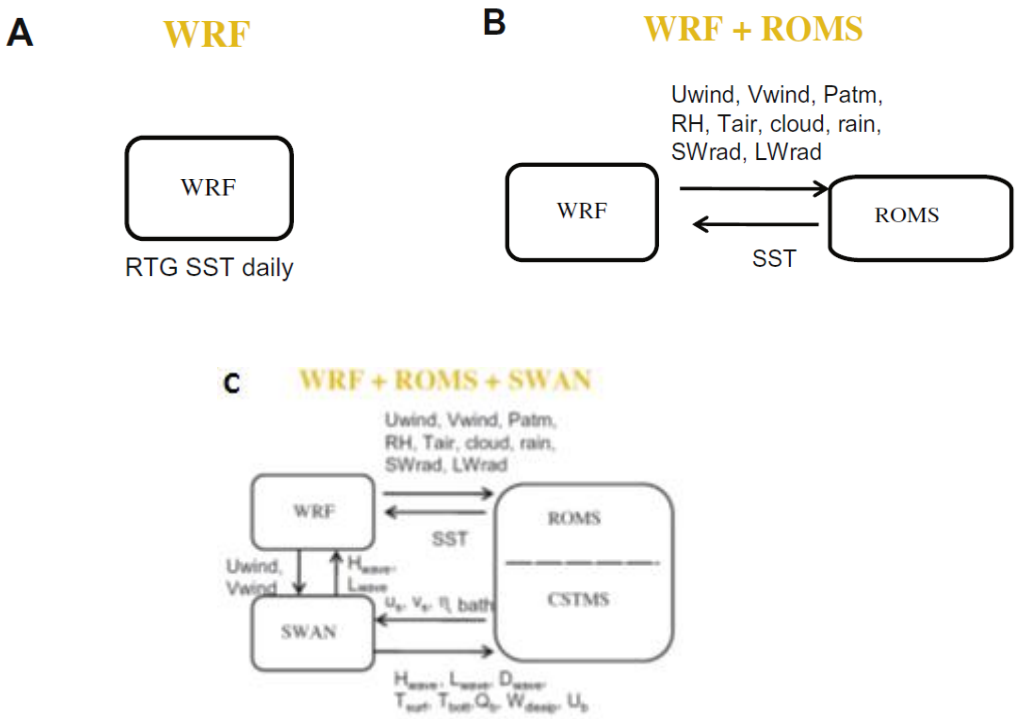

Figure 7 Different configurations that the COAST coupled system can assume. Legend: **Uwind**: zonal wind component; **Vwind**: meridional wind component; **Patm**: atmospheric pressure; **RH**: air relative humidity; **Tair**: atmospheric surface temperature; **Cloud**: cloud cover fraction; **Rain**: precipitation; **SWrad**: shortwave radiation; **LWrad**: longwave radiation; **SST**: sea surface temperature; **Us**: Zonal component of ocean surface current; **Vs**: Meridional component of ocean surface current; **η**: free surface elevation; **bath**: bathymetry; **Hsig**: significant wave height; **Lwave**: wave length; **Dwave**: wave direction; **Tsurf** : surface wave period; **Tbottom**: bottom wave period; **Qb**: percentage wave breaking; **Wdissip**: wave energy dissipation; **Ub**: bottom orbital velocity; **WRF**: Weather Reaseach and Forecasting; **ROMS**: Regional Ocean Modelling System; **SWAN**: Simulating Waves Nearshore; **CSTMS**: Community Sediment Transport Modelling System.

In WRF the sea surface roughness is computed as:

$$z_0 = c_a \frac{u_*^2}{g} + \frac{\upsilon}{u_*} \tag{27}$$

In COAWST, in order to take into account the effects of waves on the sea surface roughness, the same variable is computed following Taylor and Yelland (2000) as:

$$z_0 = 1200.0 * H_{wave} \left(\frac{H_{wave}}{L_{wave}}\right)^{4.5} + 0.11 \frac{\upsilon}{u_*} \tag{28}$$

where H_{wave} is the significant wave height, L_{wave} is the mean wavelength, u_* is the friction velocity and υ is the viscosity.

3.3 Model configuration

3.3.1 ROMS

In the ROMS simulations presented here a Mercator projection was used in a computational grid with 1/12° spatial resolution (approximately 7 km) and 32 vertical sigma layers, with increased resolution near the ocean surface and seafloor. The model was initialized with salinity and temperature profiles from the Levitus World Ocean database (Locarnini et al., 2006). A 5 year spin-up period was completed in each ROMS simulation, in order to become stable the mean annual kinetic energy within the computational domain. At the lateral boundaries, radiation and nudging conditions were imposed for the tracers variables (temperature and salinity) using climatological data and for the 3-D and 2-D momentum variables (U, V and W velocity components). For the ocean free surface, a simple gradient condition was applied. This condition consists in setting the gradient of the free surface to zero at the edge of the computational domain, and the outside value settled equal to the closest interior value. For the discretization of the advection term, third-order upstream horizontal advection and fourth-order centered vertical advection schemes were used. Tracers and momentum were horizontally mixed on geopotential (constant Z) surfaces.

Bulk-flux algorithms were used to compute the turbulent fluxes at the air-sea interface. The ocean surface was forced with time series of surface wind, air temperature, relative humidity, precipitation, cloud cover, pressure and net shortwave radiation. The net longwave radiation was computed internally by the model, using an equation presented by Beriland and Beriland (1952), as a function of air temperature, sea surface temperature, relative humidity and cloud fraction. An analytical bottom temperature and salinity flux and a quadratic bottom friction function were also used.

An equation for the turbulent kinetic energy and equation for kl (turbulent kinetic energy times the generic turbulent length scale) were used, as part of the turbulence closure scheme (GLS).

3.3.2 COAWST

A common grid with a 10 km spatial resolution was used in the present work for the three models that comprise the COAWST system (WRF, ROMS and SWAN). The ROMS initial and boundary conditions were derived from the Levitus world ocean database (Locarnini et al., 2006), similarly to the configuration presented above for the ROMS-only simulations.

Initial and boundary conditions of the WRF atmospheric model were computed with data from the GFS (Global Forecast System) global model from NCEP with a 1° spatial resolution (NCEP Final Analysis). Table 1 summarizes the main options used in the WRF model.

Microphysics (mp_physics)	*WRF Single-Moment 3-class scheme*
Longwave radiation (ra_lw_physics)	RRTM scheme: Rapid Radiative Transfer Model
Shortwave radiation (ra_sw_physics)	Dudhia scheme
Surface layer (sf_sfday_physics)	MM5 similarity
Land surface (sf_surface_physics)	Noah Land Surface Model
Planetary boundary layer (bl_pbl_physics)	Yonsei University scheme
Cumulus Parameterization (cu_physics)	Kain-Fritsch scheme
Diffusion Option (diff_opt)	Simple diffusion
K Option (km_opt)	2d Deformation

Table 1 Main options related to physical packages used in the atmospheric model (WRF).

The WRF model was configured to use the Single-Moment 3-class scheme. The computational procedures of this microphysics scheme are described in Hong et al. (2004) and Hong and Lim (2006). With respect to radiation parameterizations, longwave radiation was computed with the Rapid Radiative Transfer Model scheme (Mlawer et al., 1997) that accounts for multiple bands, trace gases, and microphysics species. Shortwave radiation was computed by the Dudhia scheme (Dudhia, 1989) that consists in a simple downward integration, efficiently representing clouds and clear-sky absorption and scattering. For the surface layer, a MM5 similarity scheme was used. This scheme is based on Monin-Obukhov with Carslon-Boland viscous sub-layer and stability functions from Paulson (1970), Dyer and Hicks (1970), and Webb (1970), used to compute surface exchange coefficients for

heat, moisture and momentum. A convective velocity following Beljaars (1994) is used to enhance surface fluxes of heat and moisture.

In what concerns surface physics, the Noah Land Surface Model scheme was selected (Chen and Dudhia, 2001), with soil temperature and moisture in four layers, fractional snow cover and frozen soil physics. The parameterization of the planetary boundary layer follows the Yonsei University scheme (Hong et al., 2006), a non-local K scheme with an explicit entrainment layer and parabolic K profile in the unstable mixed layer. In this scheme the PBL (Planetary Boundary Layer) top is defined using a null critical bulk Richardson number. Counter gradient terms are applied to represent fluxes due to non-local gradients, which give an explicit treatment of the entrainment layer at the PBL top. For cumulus parameterizations, the model uses the Kain-Fritsch scheme (Kain, 2004), a deep and shallow convection sub-grid scheme, using a mass flux approach with downdrafts and a Convective Available Potential Energy removal time scale.

Diffusion in WRF is defined by two parameters: the diffusion and the K options. The diffusion option selects how the derivatives used in diffusion are calculated. The selection was of a diffusion option in which gradients are simply taken along coordinate surfaces. The K option, which selects how the K coefficients are calculated, corresponds to a case where K for horizontal diffusion is diagnosed from horizontal deformation. The vertical diffusion is done by the PBL scheme.

Nudging boundary conditions are imposed and updated on a 6-hourly basis in a selected zone of one cell around the domain. The boundary conditions are determined entirely by temporal interpolation from external data and four relaxation cells around the domain, where the model is nudged towards the imposed data.

With respect to the wave model (SWAN), the initial conditions were obtained from a stationary steady state simulation and the boundary conditions are obtained from the NOAA NCEP Wave Watch 3 model output archive. Fields of wave height, period, and direction were interpolated to points along the open boundary of the wave model to create parametric files.

The ocean model used 32 sigma vertical levels and a baroclinic time step of 100 s and a barotropic time step of 100/120 s. The atmospheric model used 27 vertical levels and a time step of 60 s. All models were synchronized every 10 minutes to exchange data fields through the MCT coupler.

Chapter 4 Numerical simulations of the Iberian coastal upwelling with ECMWF re-analysis data

In this numerical study, two ROMS simulations were conducted using 6-hourly atmospheric forcing from the ECMWF (European Centre for Medium-Range Weather Forecast) reanalyses: one for the 1961-2001 period using ERA-40 data (Uppala et al., 2005); the second for the 1989-2008 period using ERA-Interim data (Dee et al., 2011). The main aim of these simulations is to test the ability of the ROMS model in the chosen setup to represent the Iberian coastal upwelling and to assess inter-annual variability and decadal trends.

4.1 Results and discussion

In order to simulate the ocean-atmosphere interaction in these ocean-only model runs, seven surface atmospheric variables are transferred to ROMS (surface wind, shortwave net radiation, surface air temperature, surface pressure, relative humidity, cloud cover and precipitation rate) with a 6-hour periodicity. Of the seven atmospheric variables used to force the ocean surface, the surface wind is the most relevant for coastal upwelling.

The upwelling episodes off western Iberia were identified through the analyses of the simulated sea surface temperature, sea surface height and surface currents. In sectors near three main capes of the western Iberian coast, more precisely Cape Finisterre (42.9°N; 9.3°W), Cape Carvoeiro (39.4°N; 9.4°W) and Cape St. Vincent (37.15°N; 8.9°W), daily time series were analyzed to assess trends in western Iberian upwelling. The geographic location of these capes is shown in Figure 8. The limits of the computational domain for the ERA-40 forced simulation are represented in Figure 8 by the black line and the limits of the ERA-Interim run by the yellow line.

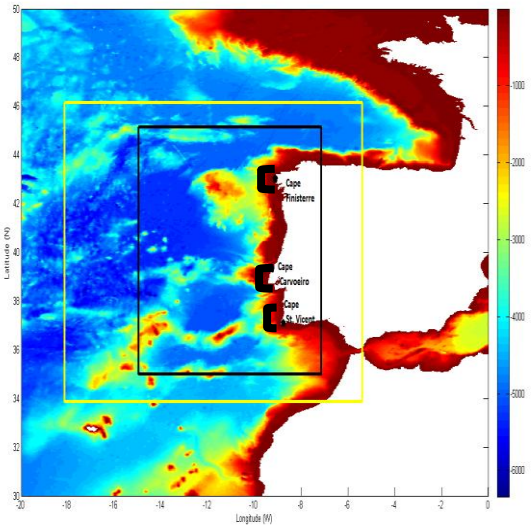

Figure 8 Limits and bathymetry of the ROMS computational domain for the ERA-40 (black line) and ERA-Interim (yellow line) forced simulations. The location of the north, central and south sectors used for the analysis of the ROMS results are also shown in the figure.

Figure 9 (a-c) shows the seasonal mean wind roses at each of the three capes studied here. At Cape Finisterre, Cape Carvoeiro and Cape St. Vincent the wind intensity and direction are essentially unchanged between the different seasons. At Cape Finisterre the mean wind blows from NE and at Capes Carvoeiro and St. Vincent the wind blows predominantly from NW. At the three capes the meridional wind component is always larger than the zonal component.

Spatially opposite decadal trends in the meridional wind field were computed in the 1989-2008 period of the ERA-Interim and in the 1987-2007 satellite-derived wind data (Figure 10). ERA-Interim and scatterometer data, essentially corresponding to the same time interval, agree in general terms, pointing to a decreasing of upwelling-favorable wind in the north and increasing of upwelling-favorable wind in the south. When compared to ERA-Interim, scatterometer data suggests stronger positive trends (decrease of northerly wind) in the north and central sectors, and weaker negative trends near the south sector. However, one should note that scatterometer data is unreliable near the coast. During the 90s decade the wind trend dipole is not present in the ERA-40 (Figure 10 a-left); it is just noted a stronger wind intensity weakening in the north than in the south. The evolution of the meridional wind field is more intense during the summer season, as noted in Figure 10b, where the dipole is presented in the 3 wind datasets analyzed.

In order to assess the statistical significance of these wind trends, the p-value of the meridional wind was computed following the Mann-Kendall method, applied to the full period of data (top panel in Figure 10). In the ERA-Interim data, trends are significant (at the 95% level) only in the southern

sector, whereas in scatterometer data trends are significant in most of the offshore domain west of Iberia. Due to the reduced number of data kept in the summer period (only 1 value per year in 20 years) the stronger summer trends are not found to be significant at the chosen level.

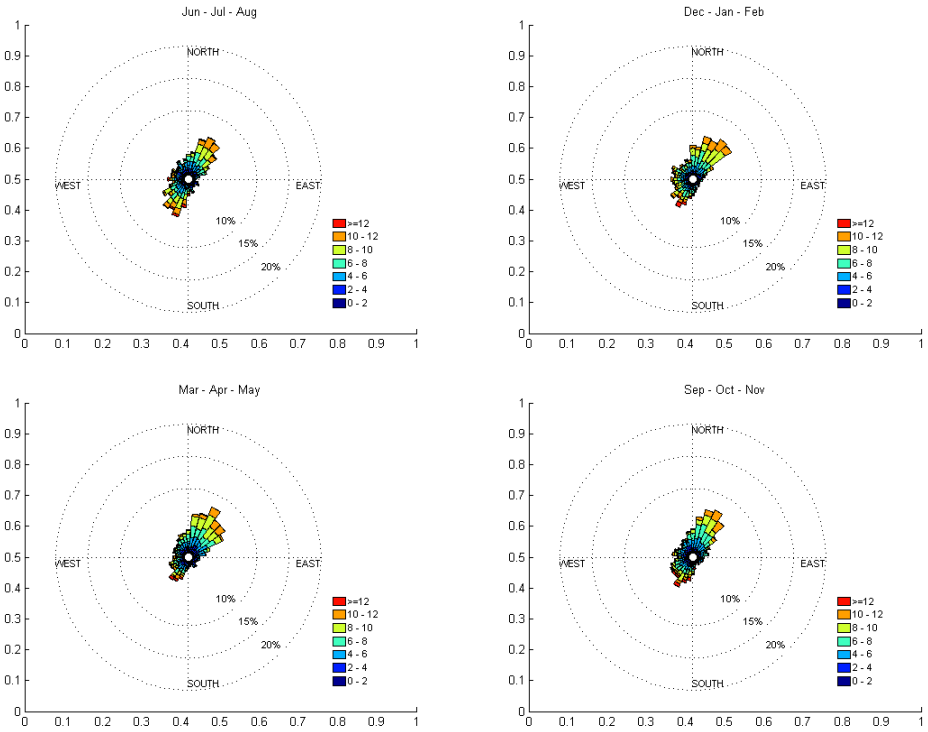

(a)

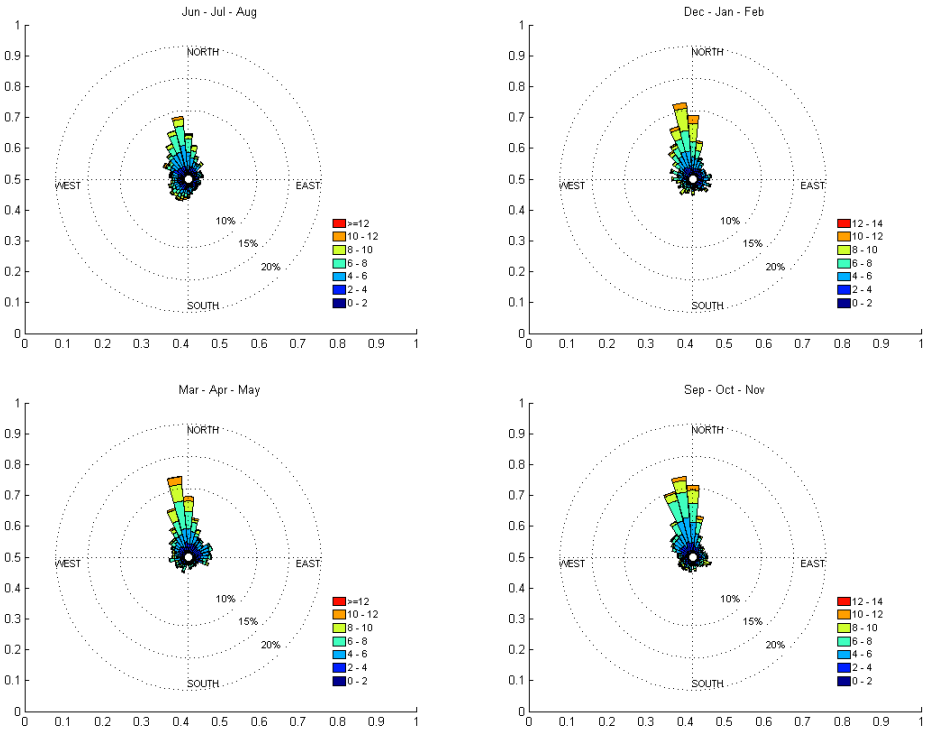

(b)

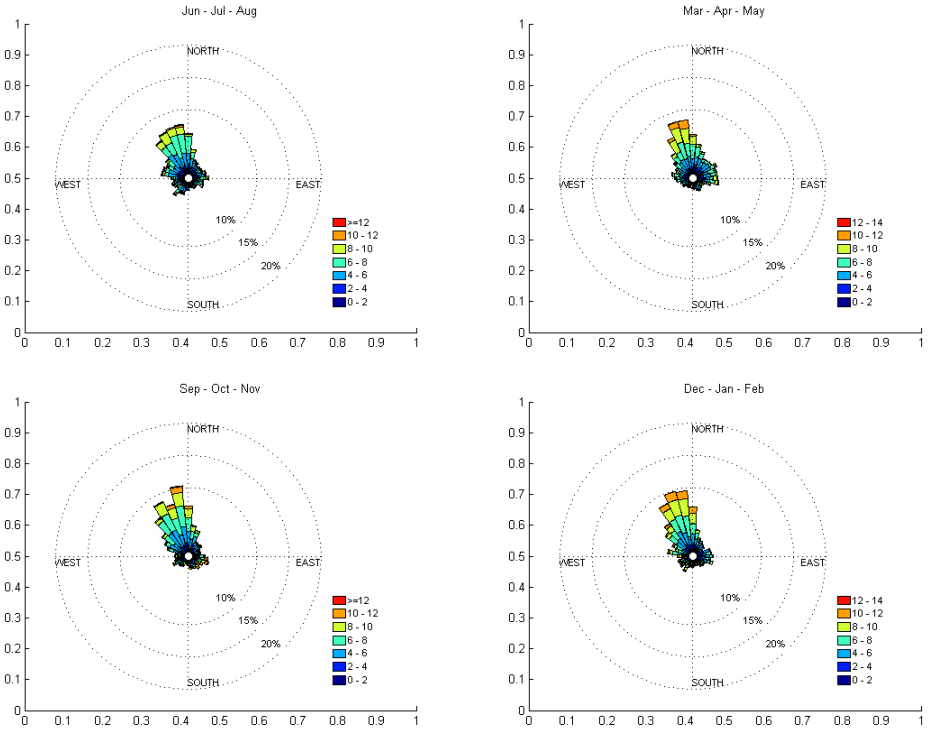

(c)

Figure 9 Seasonal wind roses for the period 1989-2008 at (a) Cape Finisterre, (b) Cape Carvoeiro and (c) Cape St. Vincent.

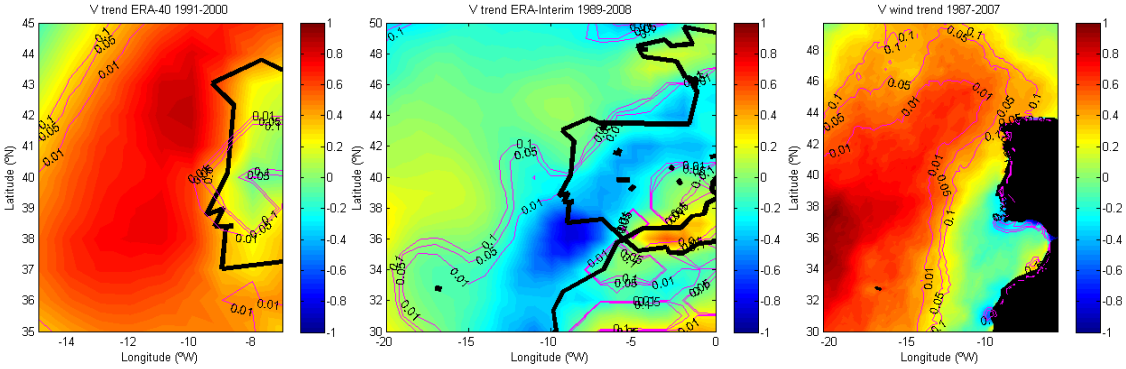

(a)

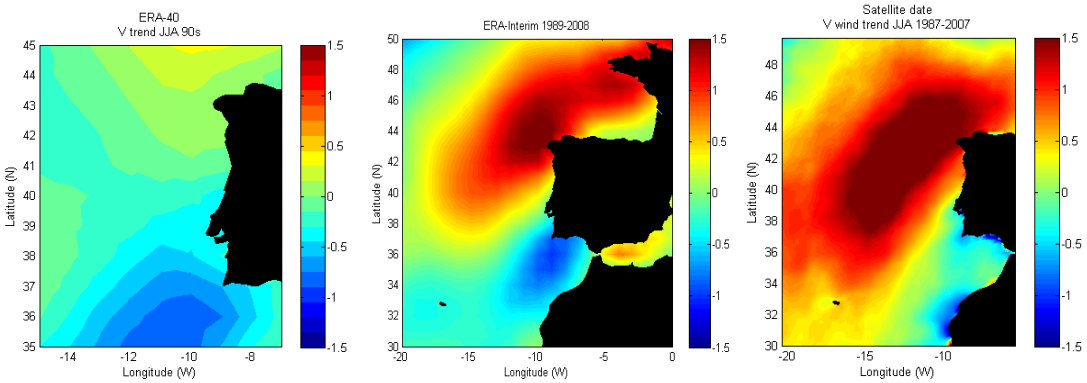

(b)

Figure 10 (a) Trend of the meridional component of wind (northerly wind on average) from (a-left) ERA 40 and for the period 1991-2000, (a-center) ERA-Interim for the period 1989-2008 and (a-right) satellite scatterometer measurements for the period 1987-2007. The isolines of p-value = 0.05 are superimposed. (b) Summer trend of the meridional component of wind (northerly wind on average) from (b-left) ERA 40 and for the period 1991-2000, (b-center) ERA-Interim for the period 1989-2008 and (b-right) satellite scatterometer measurements for the period 1987-2007.

Figure 11 shows the annual cycle of the wind curl, which can be directly associated with the forcing of coastal upwelling. As expected, the curl of the surface wind is cyclonic (positive) in coastal regions due to the surface drag being weaker over the ocean than over the continent. During the spring and summer seasons the cyclonic wind curl is more intense in the southern part than in the northern part of the western Iberian coast, possibly due to the intensification of Iberian thermal low during that season. During the autumn and winter seasons the maximum cyclonic wind curl field is displaced northwards, likely due to the wandering of the Azores High and a weakening of Iberian thermal depression. It is remembered that an increasing wind (stress) curl imply a higher Ekman pumping velocity, as shown in equation (5), thus implying more intense upwelling events, in the regions of high wind stress curl.

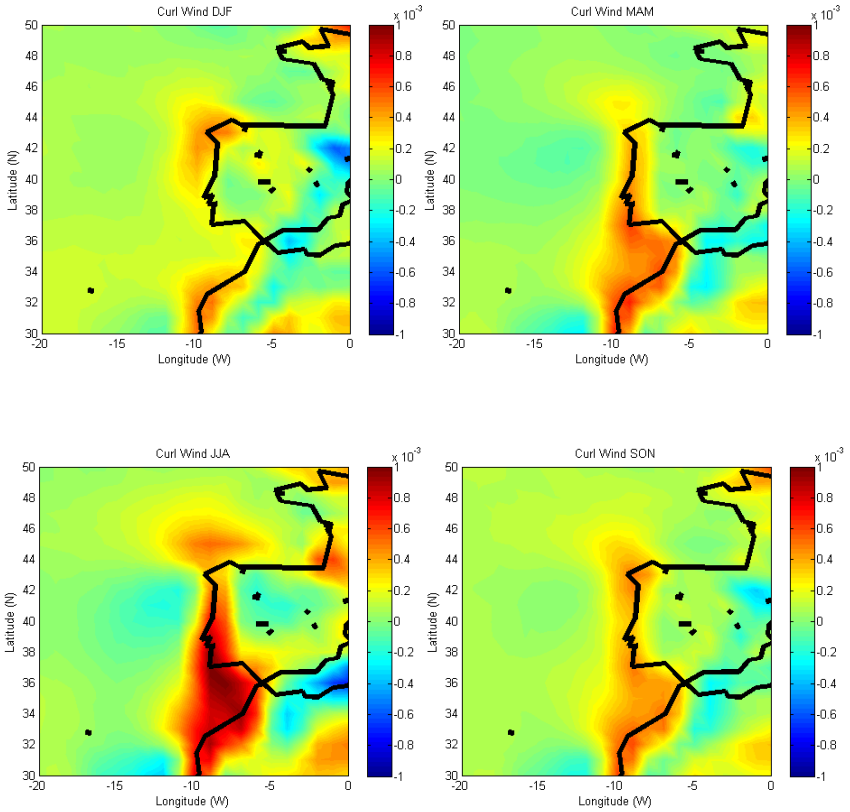

Figure 11 Maps of the wind curl (s^{-1}) averaged in different seasons.

In order to show the robustness of the modeled SST fields during an upwelling event, Figure 12 compares the SST simulated by ROMS in the sector close to Cape Carvoeiro with SST satellite data. Figure 12 also shows the meridional surface current, during a 40-day period from 20 June until 30 July 2004.

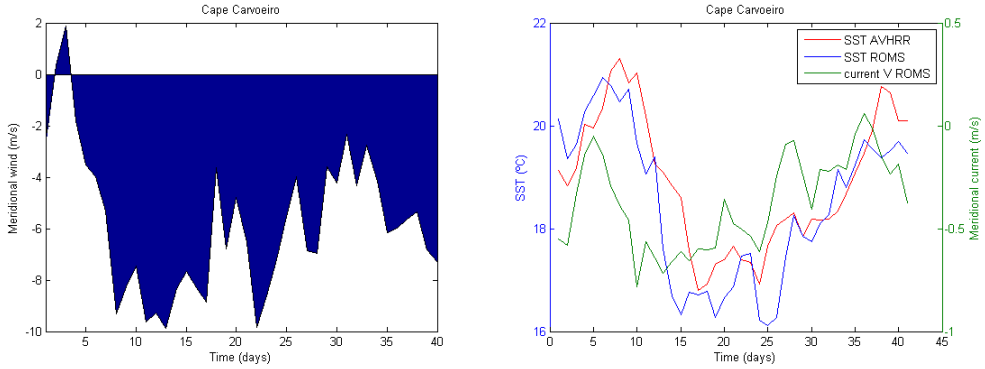

(a) (b)

Figure 12 Time series of (a) the meridional component of surface wind and (b) of SST retrieved from a satellite database (red line) and from a ROMS simulation (blue line), for a 40-day period between 20 June and 31 July 2004 in the Cape Carvoeiro region. The corresponding meridional component of surface currents is also shown in b) (green line).

During the 40 days period shown in the above figure an upwelling event occurred and it was realistically simulated by ROMS, as noted by the small differences between the blue and red line in Figure 12b. A quasi simultaneous intensification of the southward surface wind and current occurs between days 5 and 10. The SST decrease occurred 3-4 days later, due to the time required to transport the coastal deep water to the ocean surface.

Figure 13 shows the horizontal and vertical maps of ocean temperature for the days 1, 10 and 30 of July 2004, which correspond to the development, fully developed and occlusion stage of a major upwelling event.

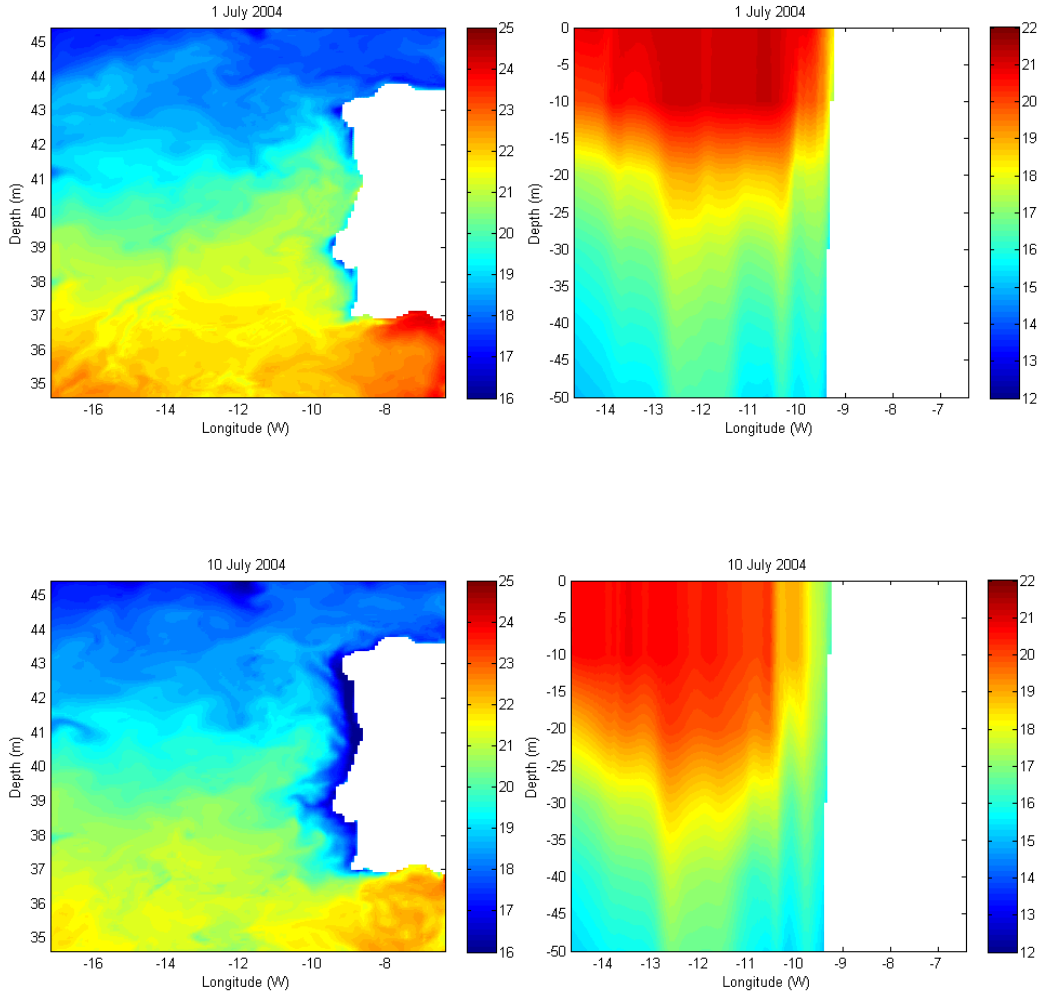

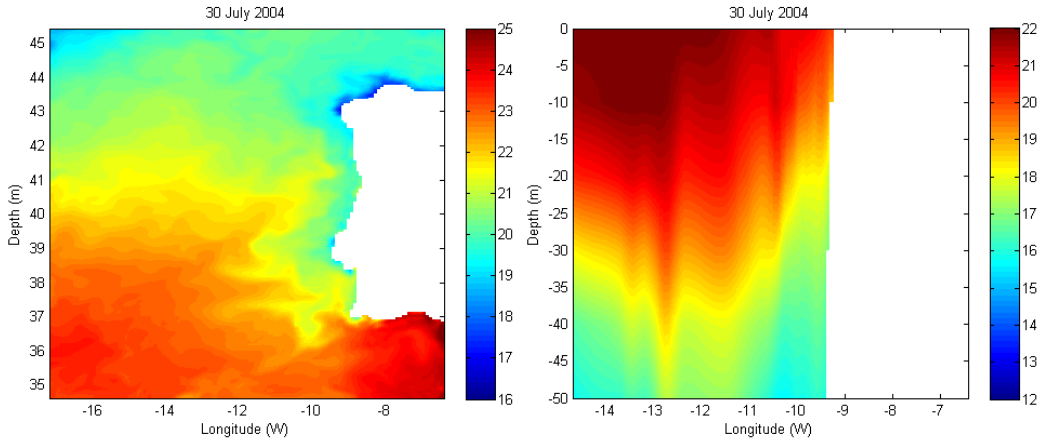

Figure 13 Horizontal and vertical distributions of ocean temperature during the beginning (top row), fully developed (middle row) and occlusion (bottom row) phases of a simulated upwelling event.

Comparing the vertical maps between days 1 July and 10 July, the rising and westward displacement of the isotherms is noted, implying a significant decrease in the ocean vertical temperature gradient in the coastal region during the fully developed phase of the upwelling event. When comparing the temperature distribution for days 10 and 30 of July the inverse situation is noted, meaning eastward displacement and descent of isotherms. In the SST maps it can be also noted that during the fully developed phase, the more significant SST decrease is only present in a narrow zone of about 100 km close to the coast.

Figure 14 shows the mean meridional current and zonal temperature gradient of the ocean upper 50 m for July 2004.

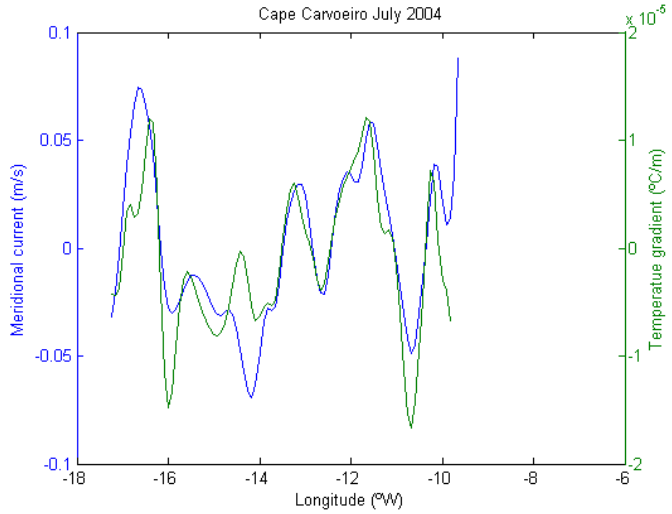

Figure 14 Mean upper-50 m meridional component of surface currents and temperature zonal gradient during July 2004.

In the above Figure a high correlation between meridional current and the zonal temperature gradient in the ocean upper 50 meters is clearly seen. The upwelling front is identified by the meridional current maximum that is present at approximately 1º to the west of the coast, and coincides with a maximum in the upper ocean temperature gradient. This corresponds to the location of the along-front equatorward jet-like flow.

Figure 15 presents the mean SST and surface current field during each season of the year.

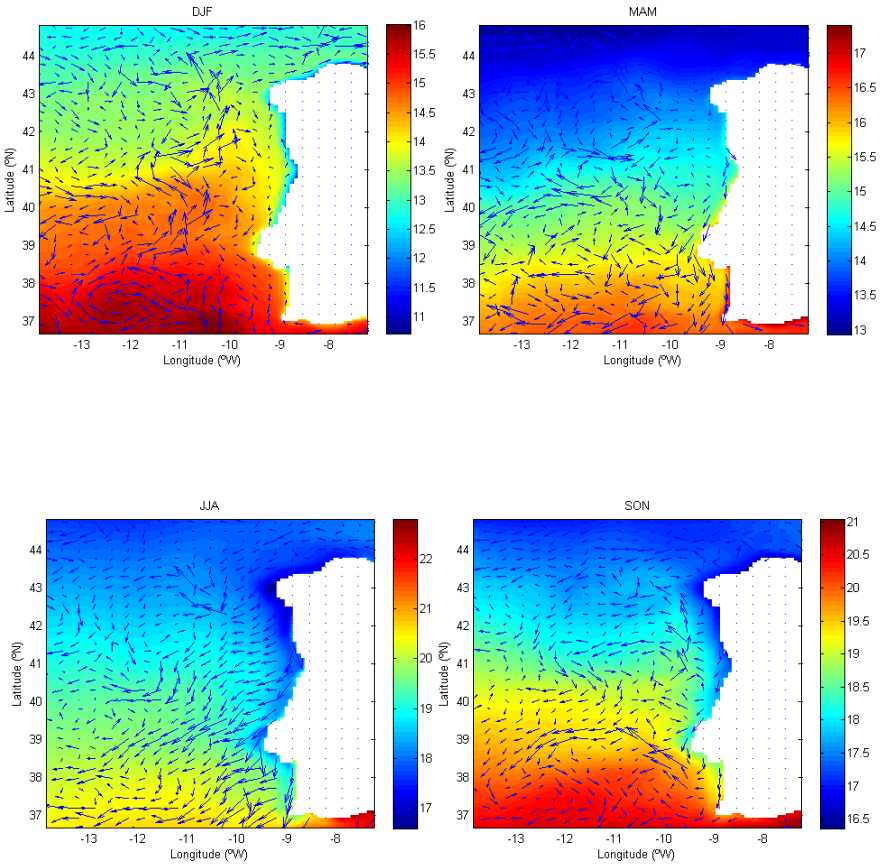

Figure 15 Mean seasonal SST and surface currents, retrieved from a ROMS simulation forced with ERA-Interim reanalysis.

In the above figure the coastal upwelling phenomenon is mostly noted by the low coastal SST during the summer months (JJA). Also noted is the expected south-westward surface current along the western Iberia coast during the upwelling season. During the other seasons the mean surface current field off western Iberia exhibits lower values than during summer. During winter a mean northward current is present in the northern part of western Iberia.

Figure 16 presents, for three coastal sectors along the western Iberian coast and for the summer months (JJA), the decadal boxplots of the number of days with a SST difference (between a sector

close to the coast and a sector located 300 km offshore) larger than 2°C. Each sector contains 5×2 computational cells, corresponding to a region of 35 km × 14 km nearby each cape. Figure 16a shows results from the ERA-40 forced ROMS run, Figure 16b from the ERA-Interim forced run and Figure 16c shows, for comparison and later discussion, satellite data.

In the boxplots, the edges of the box represent the 25th and 75th percentiles, the red line is the median and the green point is the mean value. Points are drawn as outliers (red points) if they are larger than $q_3 + 1.5 \times (q_3 - q_1)$ or smaller than $q_1 + 1.5 \times (q_3 - q_1)$, where q_1 and q_3 are the 25th and 75th percentiles, respectively.

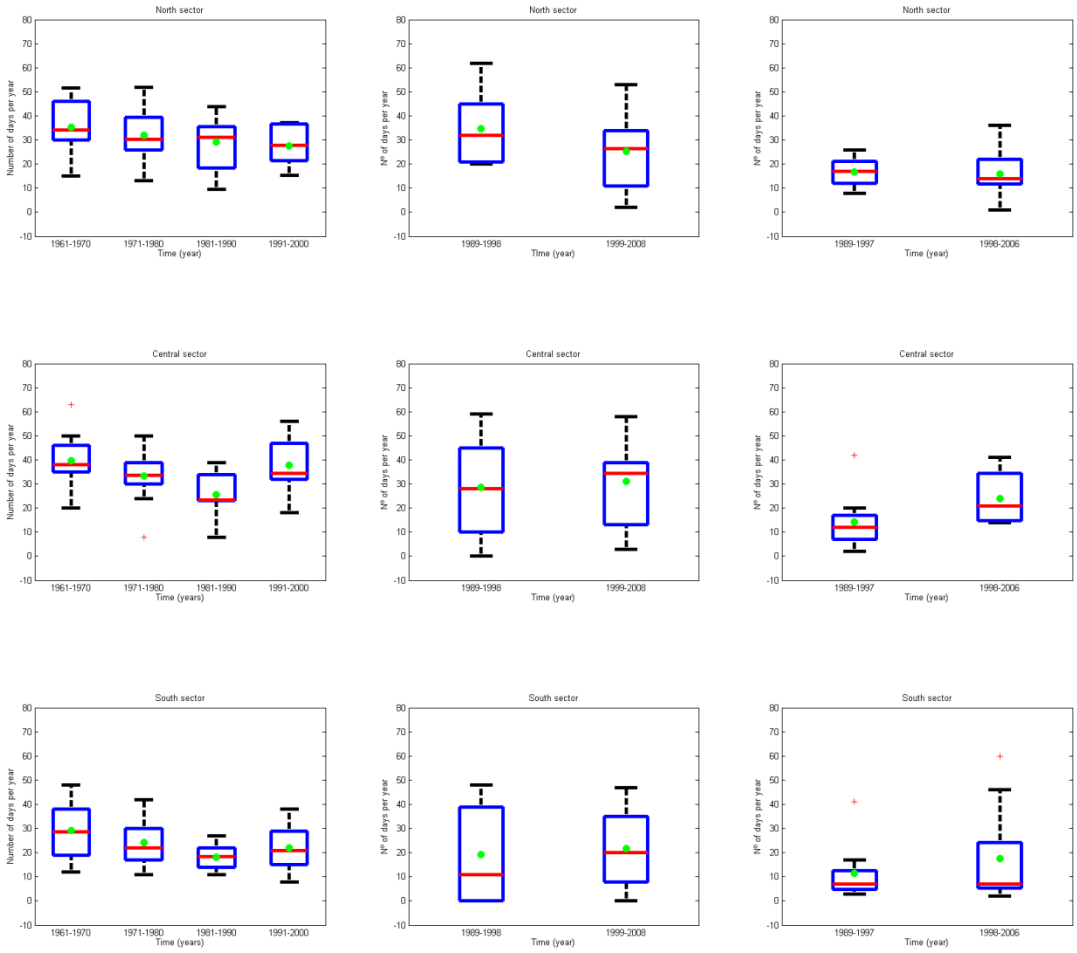

Figure 16 Inter-annual distribution of the mean number of upwelling days during summer months (JJA) in three sectors (north, center and south Iberia) along the western Iberian coast: (a, left panels) from the ERA-40 forced run; (b, middle) the ERA-Interim forced run; (c-right) from AVHRR satellite data. Upwelling days are defined as days with a near-coast SST 2°C colder than the 300-km offshore temperature.

In the above figure, the northern sector shows, in the ERA-40 forced simulation, a permanent decrease from the 60's to the 90's in the median (and also in the mean) value of the number of days with

ΔSST > 2°C. That feature continues to be noted in the ERA-Interim forced simulation and is also confirmed by the satellite data. In the central sector, the results indicate a decrease in the mean (and median) value of the number of upwelling days from the 60's to the 80's followed by an increase from the 80's to the 90's, which is also present in the ERA-Interim simulation and in the SST satellite data (period 1989-2007). The south sector follows a similar time history. Satellite data also indicate an increase in inter-annual variability and skewness in the central and south sectors.

The opposing trends in the meridional wind intensity along the western Iberian coast (Figure 10) are in good agreement with the boxplots of the number of days with ΔSST > 2 °C, which show a decrease of the upwelling index in the north sector and a slight increase in the south sector. These opposing trends confirm the results of some previous local studies, where a decreasing number of upwelling days during the last decades along the northern part of western Iberian coast was noticed (e.g. Bode et al., 2009) and an increasing number of upwelling days along the southern part of the coast was recorded (Santos, et al., 2005; Relvas et al., 2009).

With respect to the mean SST close to each of the three capes (not shown), a similar behavior during the analyzed period at the three sectors was seen: a slight decrease from the 60s to the 70s followed by an increase from the 70s to the 80s and an almost constant value from the 80s to the 90s. In the SST boxplots of the ERA-Interim forced simulation (not shown) a lower SST is noted in the second decade only at Cape St. Vincent, which should be a consequence of the larger number of upwelling days in that region. In the second decade, the variability of SST increases more in the south than in the north, which should also be a consequence of an increasing number of coastal upwelling events in the former region.

Figure 17 presents the mean SST for each day of the mean year in the central sector obtained from the ERA-40 and ERA-Interim forced simulations and from SST satellite data. In these figure the red line corresponds to the SST in the sector close to the coast and the blue line to the SST in a region located 300 km away from the coast.

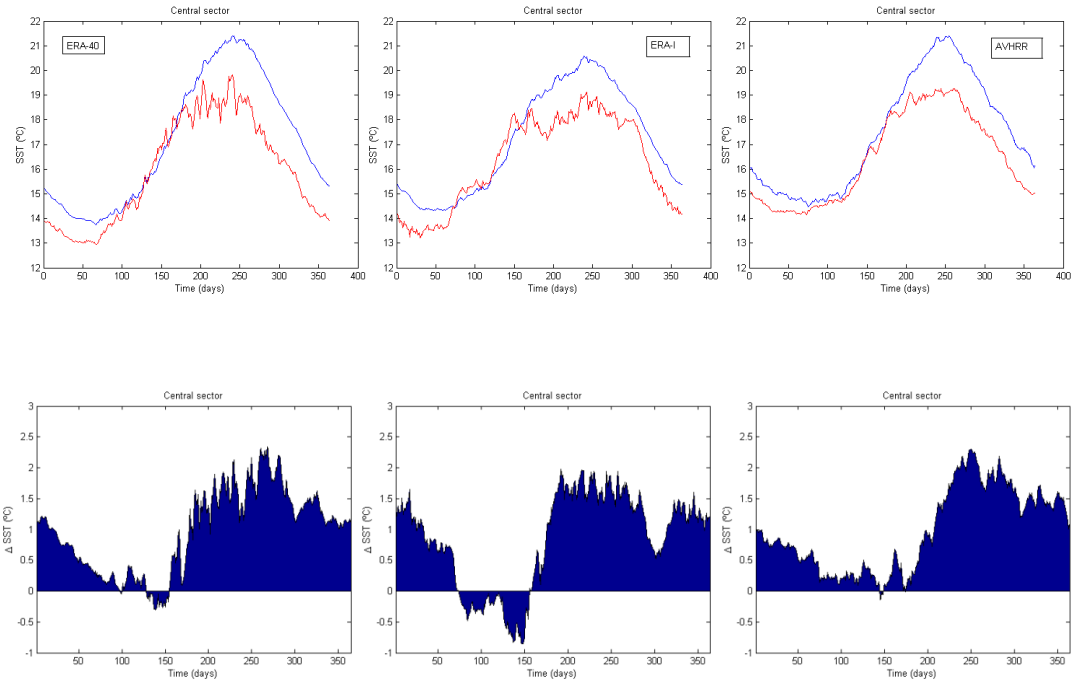

Figure 17 (upper panel) Mean sea surface temperature for each day of the mean year at the latitude of Cape Carvoeiro: (right) 1961-2000 ERA-40 forced run; (center) 1989-2008 ERA-Interim forced run; (left) 1989-2007 satellite AVHRR data. The near coast SST is depicted in red and the 300 km offshore SST is in blue. (lower pannel) Differences between the SSTs shown in upper pannel.

In Figure 17 the average impact of the episodic coastal upwelling is shown during the summer months by a mean lower SST, by about 2 ºC, in the region close to the coast compared to the sector located 300 km offshore. From autumn until the end of the winter season a weaker zonal SST gradient is still observed. During spring, higher SST is found close to the coast than in the sector 300 km offshore. The opposed SST zonal gradients during the autumn and spring seasons indicate the faster response of the shallower inshore region to air temperature changes than the deep ocean regions. The zonal SST gradient during the autumn and winter months and the absence or opposed sign of the gradient during spring is observed in the 3 datasets (ERA-40 run, ERA-Interim run and satellite data).

Figure 18 shows decadal boxplots of simulated SSH for the regions near each analyzed cape.

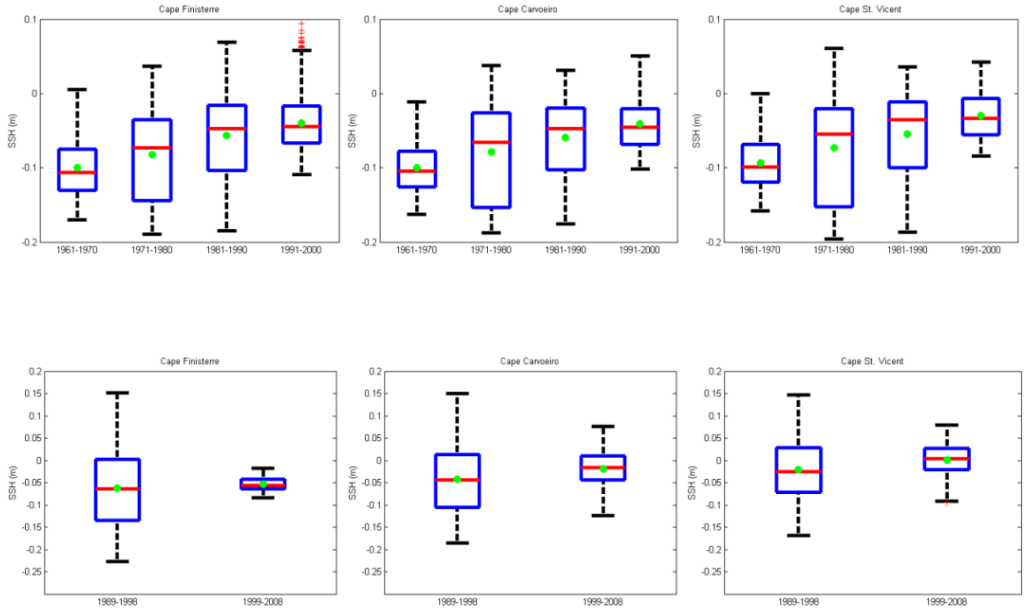

Figure 18 Decadal boxplots of sea surface height at (a-left) Cape Finisterre; (b-center) Cape Carvoeiro and (c-right) Cape St. Vincent, for the ROMS runs forced with (upper panel) ERA-40 (1961-2000) and (lower panel) ERA-Interim (1989-2008).

From the SSH spatial distributions it is possible to identify a coastal upwelling event, since the Ekman transport in the ocean surface layers implies a convergence of the ocean upper layers in the offshore region. As a consequence, a zonal gradient in the SSH field is observed, with higher SSH offshore and lower SSH close to the coast. This zonal SSH gradient set-up reveals an intensification of the ocean meridional geostrophic current.

The evolution of the near shore SSH is highly consistent at the three coastal sectors. From the 1970s onwards, the increase in near shore SSH has been accompanied by a significant reduction in inter-annual variability. At present, satellite data of SSH is not reliable in the near shore region, so the ROMS results cannot be directly validated. Coastal SSH trends may be due to two effects: first as a consequence of thermal expansion of the ocean (being a secondary effect of global warming); second as a dynamic response due to upwelling (with increased upwelling reducing the thermal expansion effect). This latter effect could be responsible for some decrease in near shore SSH trends, although there are also mechanical limitations to the slope of the sea surface.

A more episodic view of upwelling is presented in Figure 19. In this figure seasonal scatters and histograms of the SST difference and surface zonal current are presented for the region near each analysed cape and for the ERA-Interim period (1989-2008). In these scatters a point represents one day of simulation.

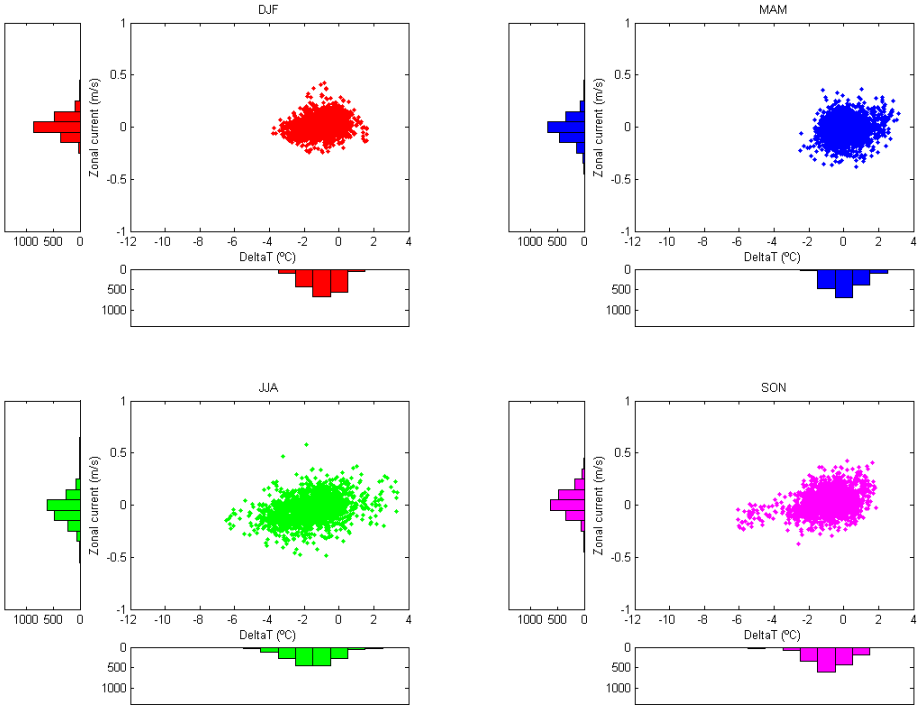
DJF
MAM
JJA
SON
Zonal current (m/s)
DeltaT (°C)
1000 500 0
1
0.5
0
-0.5
-1
-12 -10 -8 -6 -4 -2 0 2 4
0
500
1000

a)

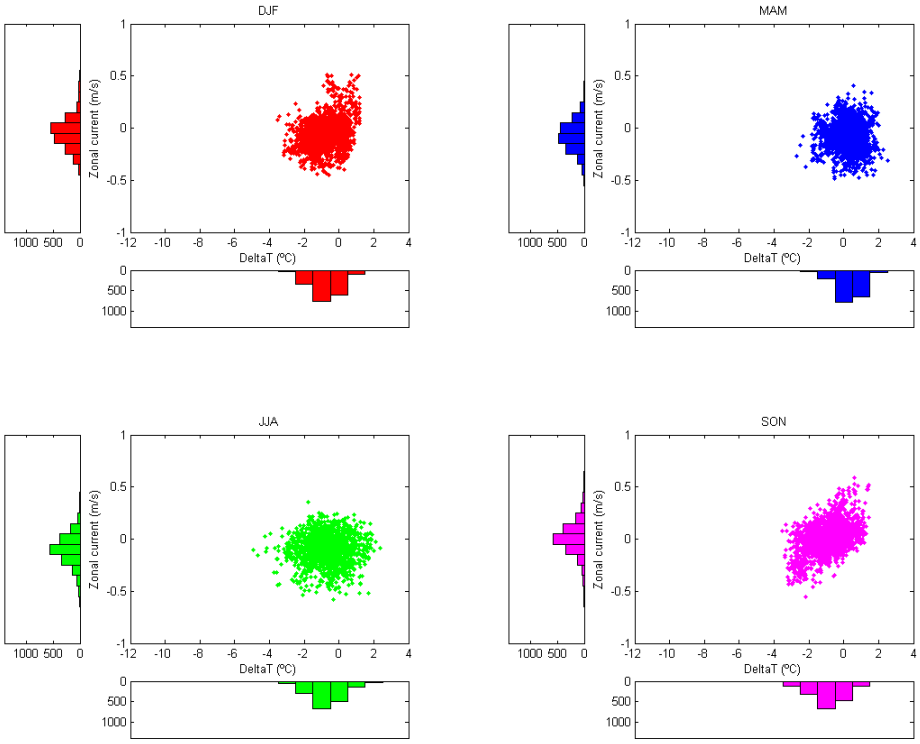
DJF
MAM
JJA
SON
Zonal current (m/s)
DeltaT (°C)
1000 500 0
1
0.5
0
-0.5
-1
-12 -10 -8 -6 -4 -2 0 2 4
0
500
1000

b)

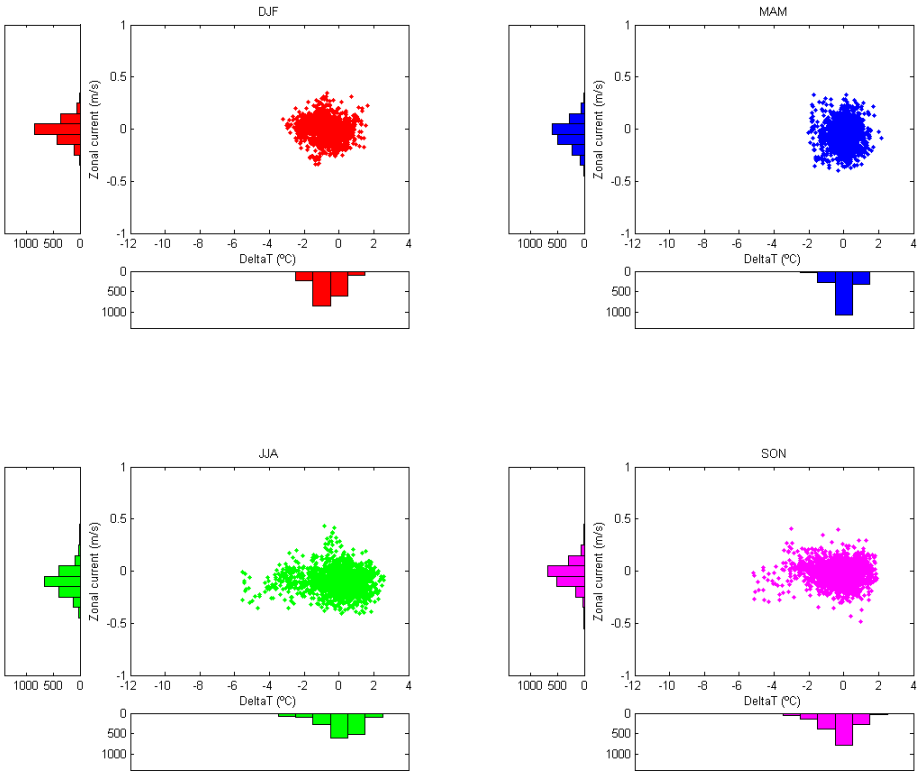

c)

Figure 19 Seasonal scatter plots of zonal current versus sea surface temperature difference (between coast and 300km offshore) and the associated histograms for 1989-2008 (ERA-Interim period) at: (a) Cape Finisterre; (b) Cape Carvoeiro and (c) Cape St. Vincent.

In Figure 19, the seasonality of the surface zonal current and ΔSST variables is clearly seen. The two plotted variables exhibit a higher variability during the summer and autumn seasons due to the occurrence of coastal upwelling events. The highest negative ΔSST is observed during the summer when some events with ΔSST < -6 °C are observed. With respect to the zonal surface current, a seasonal cycle is found with a westward (negative) intensification during the summer season, due to Ekman transport along the western Iberian coast. The seasonal scatters and histograms for the ROMS ERA-40 forced simulation (not shown) also exhibit the above mentioned characteristics.

Figure 20 shows the yearly cycle of the mean number of days per month with ΔSST < -2 °C for the sector nearby each analyzed cape during the ERA-Interim period. The figure shows that the maximum mean number of days with a ΔSST < - 2 °C occurs in July and August. It is noted that there are days with ΔSST < -2 °C in all months of the year. A low SST close to the coast does not necessary guarantee, however, that a coastal upwelling event has occurred. In order to verify if the zonal SST

gradient is due to coastal upwelling or not it is necessary to investigate ocean dynamical variables like the coastal surface currents and SSH.

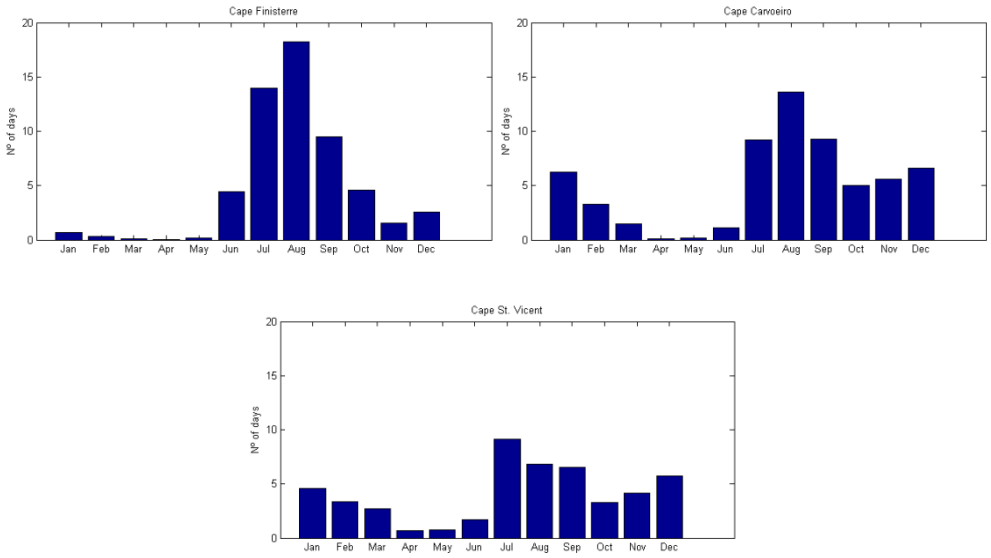

Figure 20 Histograms of the mean number of days per month with ΔSST > 2 ºC between a region close to each cape and a region located 300 km offshore: (top) for Cape Finisterre; (middle) for Cape Carvoeiro and (bottom) for Cape St. Vincent, constructed from the ROMS simulation forced with ERA-Interim reanalysis data.

Figure 21 shows the time series of the zonal and meridional components of surface currents and SST at the Cape Carvoeiro region. The SST time series 300 km offshore from Cape Carvoeiro is shown in blue.

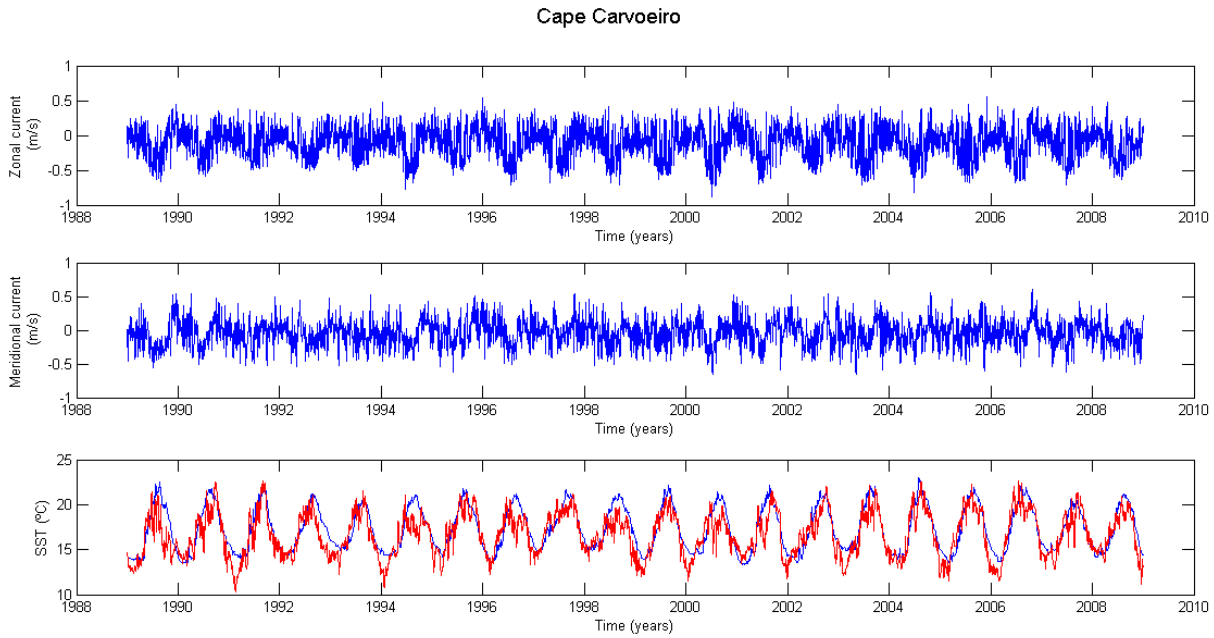

Figure 21 Time series of (top) zonal and (middle) meridional surface currents and (bottom) SST close to Cape Carvoeiro, for the 1989-2008 period. The blue line in the bottom figure corresponds to SST 300 km offshore from the cape.

The figure shows that zonal and meridional surface currents close to Cape Carvoeiro vary between -0.5 m/s and +0.5 m/s, with an intensification of the southward and westward current during the summer season. The SST usually varies between 10 °C and 21°C, with most of the summer days with a lower SST close to the coast than 300 km offshore as expected due to coastal upwelling. But it is noted that some days with lower SST close to the coast also occur during the winter.

Figure 22 shows the daily climatology of zonal and meridional surface and vertical currents at Cape Carvoeiro together with the climatology of SSH difference between the Cape and 300 km to the west.

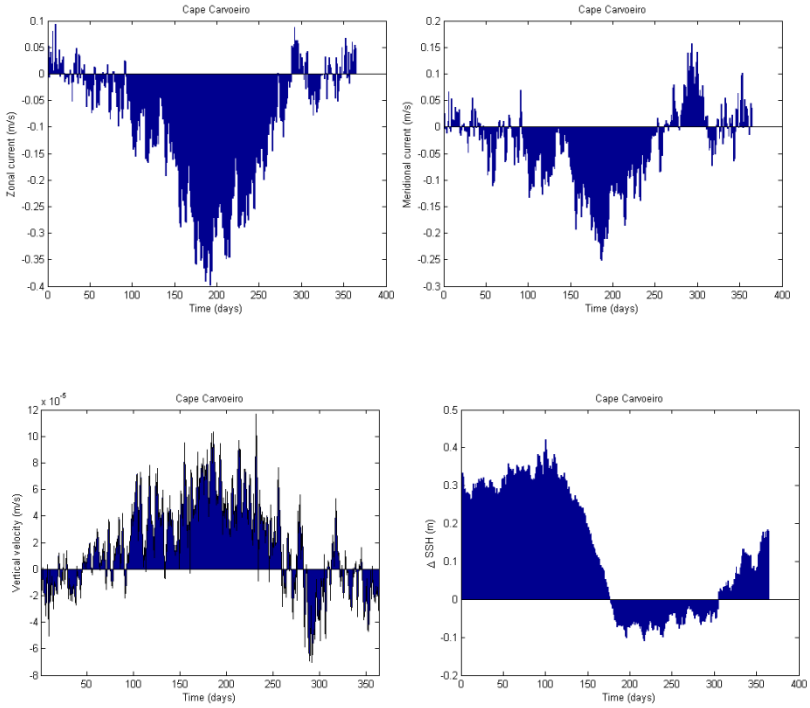

Figure 22 Climatological mean year of simulated (upper-left) zonal and (upper-right) meridional surface currents and (lower-left) vertical currents at Cape Carvoeiro for the ERA-Interim period (1989-2008) and (lower-right) ΔSSH between the cape and a location 300 km offshore.

Figure 22 shows that the expected dynamical behavior of coastal upwelling, characterized by an the intensification of southward and westward surface currents and upward vertical current and a lower SSH close to the coast (decaying and negative ΔSSH), is only noted during the summer season. These results indicate that the days with lower SST close to the coast during other seasons of the year, are not all due to coastal upwelling. As referred before, lower SST values can be due to a meridional advection of cold water into the region close to the coast, or due to low temperatures in the atmosphere in the coastal region, which will imply a heat transfer from the ocean to the atmosphere, as is normally the case during the autumn and winter months.

In Figure 23 time series of ΔSST and ΔSSH between Cape Carvoeiro and a region 300 km offshore are plotted. The figure shows that during the summer season, when most of the coastal upwelling events are observed, there is usually a zonal gradient of SST and SSH characterized by lower SSH and SST values close to the coast. However, during some of the summers there are periods when the SSH zonal gradient is observed but there is no zonal SST gradient (as is the case of summer 2003) and there are also days when a zonal SST gradient is observed but without an SSH counterpart (like during the summer of 1996). These cases indicate that caution should be taken when considered only the SSH as an upwelling index. The correlation between ΔSST and ΔSSH, presented in Figure 23 has a value of 0.43. Analyzing the simulated SSH in conjunction with the SST has the advantage of possibly

identifying the cases misinterpreted as upwelling events, when a lower SST observed close to the coast is not due to coastal upwelling**.** On the other hand, SSH varies much more slowly than SST, so SSH does not permit to correctly identify short-duration coastal upwelling events.

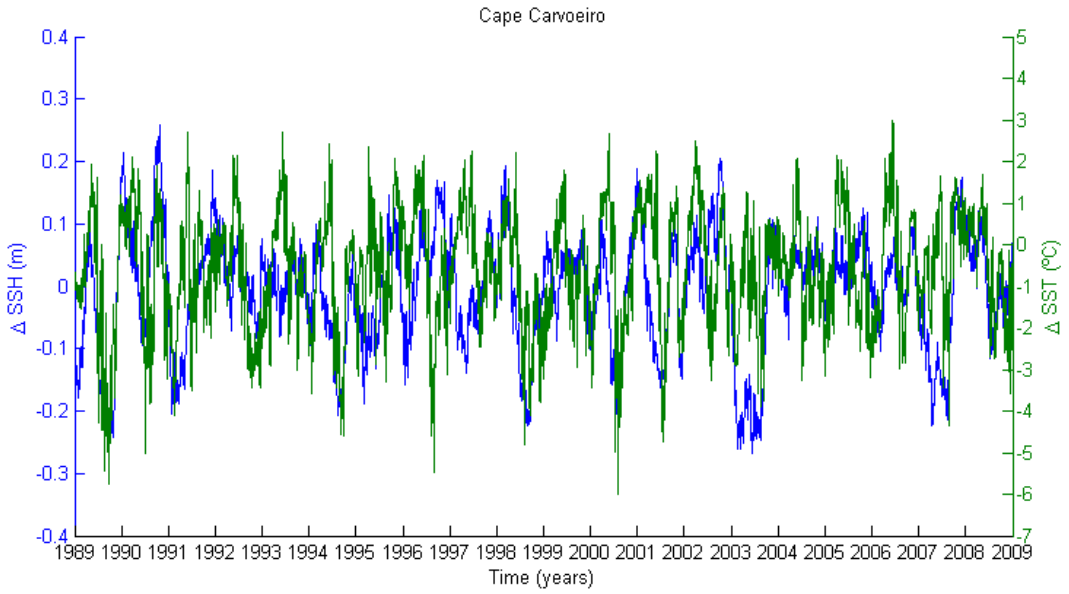

Figure 23 ΔSST (green line) and ΔSSH (blue line) between a sector near Cape Carvoeiro and a sector 300 km offshore.

The mean SST for the summer months of July, August and September along a line of constant latitude at Cape Carvoeiro is shown in Figure 24 for the case of the satellite data (red line) and of the ROMS model output (blue line).

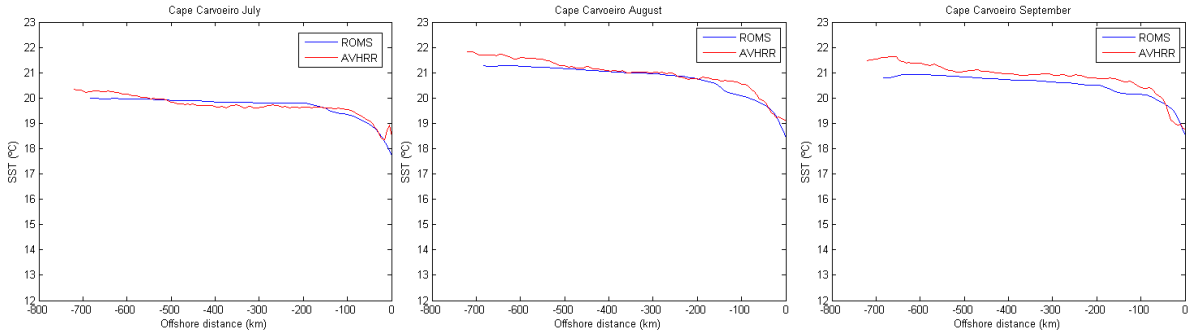

Figure 24 Zonal distribution of average SST along the Cape Carvoeiro parallel, obtained from the ROMS simulation with ERA-Interim forcing and from AVHRR Optimum Interpolated satellite data.

In the above figure it can be seen that the upwelling thermal front extends to about 200 km away from the coast in July, August and September. In the region more distant than 200 km one still verifies a slight (< 0.5 °C) SST increase until a distance of about 500 km, particularly in August, which seems to indicate that the thermal front of sporadic coastal upwelling filaments reaches distances longer than 200 km. The SST zonal gradient is present along the year, but during winter the thermal front is observed at distances much closer to the coast (lower than 50 km). A good agreement between the SST obtained from ROMS and satellite data is seen, with both sources indicating similar horizontal extent of the thermal front.

Figure 25 presents the SST trend maps for the three months of the year with higher number of coastal upwelling events (July, August and September), computed from a daily Optimal Interpolated database with a 1/16° resolution (Marullo et al., 2007). The validation with in situ measurements showed that the satellite OISST is able to reproduce in situ measurements with a mean bias of less than 0.1K and root mean square error of about 0.5 K and that those errors do not drift with time or with the interpolation error.

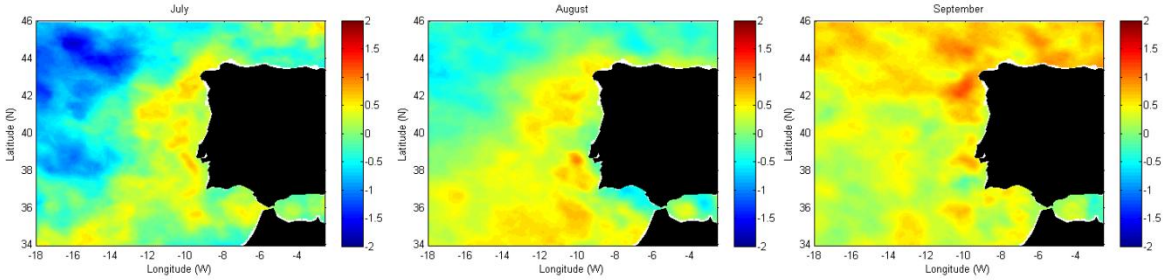

Figure 25 SST trends for the period 1989-2007 computed from a satellite AVHRR-sensor database for the months of (left) July, (middle) August and (right) September.

During the summer months a higher positive SST trend is noted in the region close to Cape Finisterre than farther south, at Capes Carvoeiro and St. Vincent, particularly in September, which should be a consequence of the increasing number of upwelling events in the southern regions and a reduced number of upwelling events in the Cape Finisterre region. These opposed trends were also noted in the ROMS simulations, presented above and in the analysis of SST trends retrieved from satellite data by Relvas et al. (2009).

The computed mean seasonal p-values, following the Mann-Kendall method of the simulated SST trends and the satellite-derived SST trends for the region adjacent to each analyzed cape, have a p-value lower than 0.01, indicating that these trends have a 99% probability of being statistically significant.

Figure 26a shows the mean daily SST of the sector nearby each cape and the sector located 300 km offshore, again for the cases of ERA-40, ERA-Interim and AVHRR-sensor data. These averaged time series were computed for the period 1989-2001, common to both ECMWF reanalyzes. In Figure 26b the mean SST difference between the satellite SST and ROMS modeled SST (when forced with ERA-Interim re-analysis data) is shown for the three sectors located close to the coast.

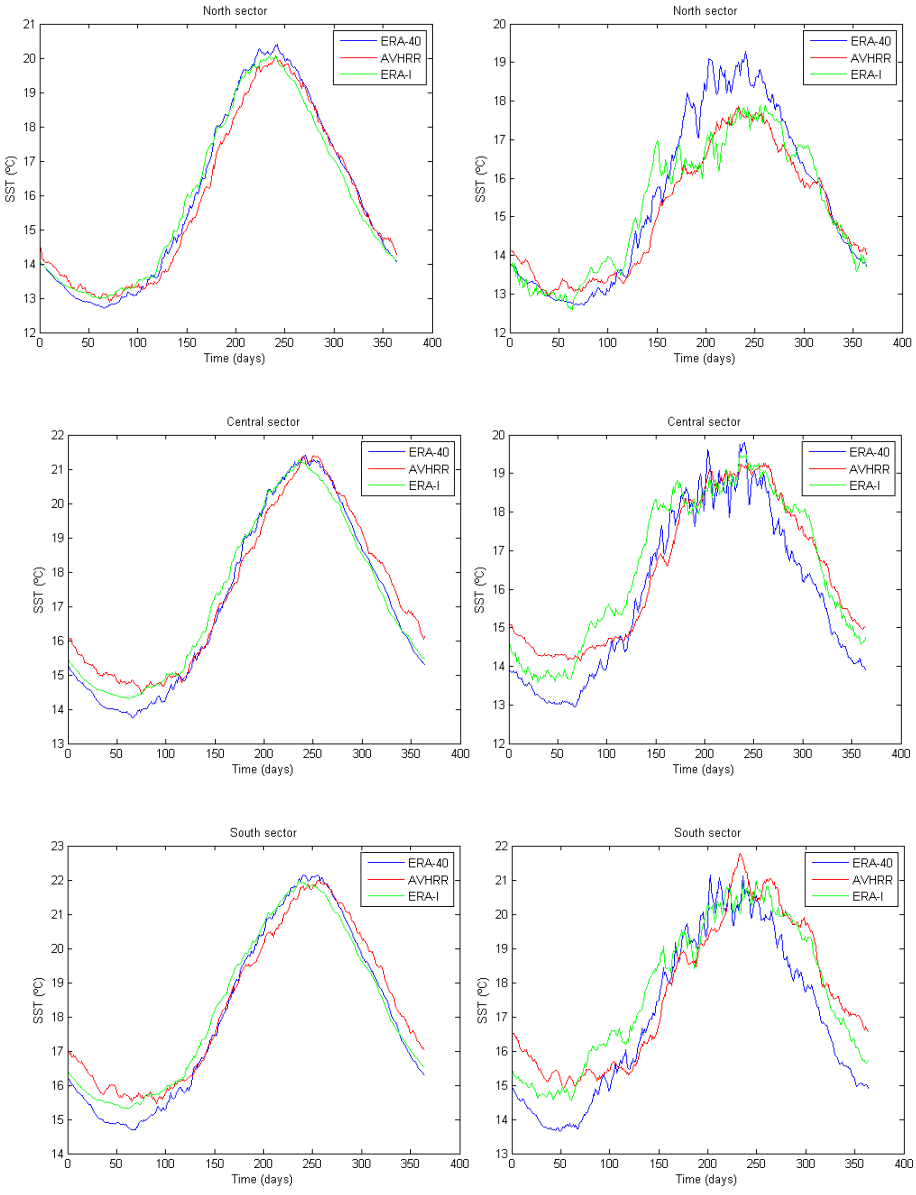

(a)

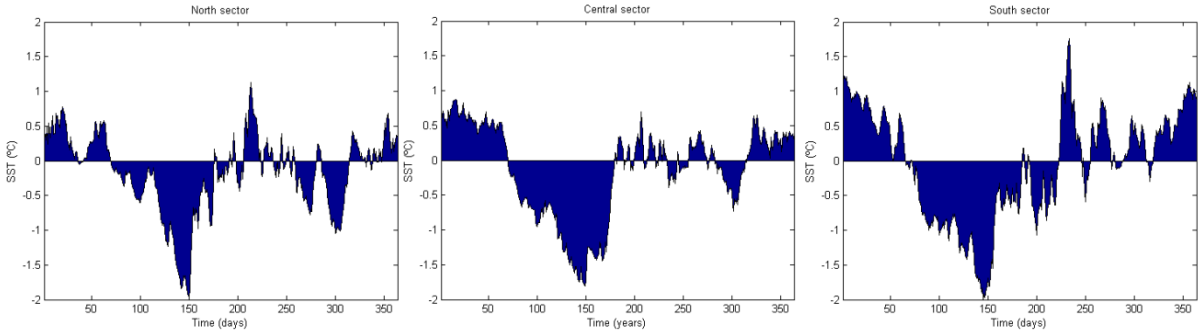

(b)

Figure 26 (a) Seasonal cycle (1989-2001 period) of sea surface temperature from ERA-40 and ERA-Interim forced runs and from AVHRR sensor data at: (upper row) Cape Finisterre, (middle row) Cape Carvoeiro and (bottom row) Cape St. Vincent. (b) Mean seasonality of satellite minus simulated (ERA-Interim forcing) SST difference for the period 1989-2001 at: (left) Cape Finisterre, (middle) Cape Carvoeiro and (right) Cape St. Vincent.

The SST differences between the ROMS simulations and the satellite data during most of the summer season are rather small (less than 0.5°C) either in the region close to each cape or in the region 300 km offshore. As expected, it is during summer that the largest variability is noted due to coastal upwelling events, which are unsynchronized between years and therefore appear attenuated in Figure 26a. During the others seasons, the SST differences between simulations and observations are larger, mainly during the spring months in the 3 coastal sectors, where differences as high as about 1.5°C can be seen. The SST cycle from the ERA-Interim forced simulation seems to be closer to the observations, demonstrating the higher quality of the ERA-Interim surface atmospheric fields when compared to ERA-40.

Figures 27 shows the differences between the mean simulated SST when forced with ERA-40 reanalysis and with ERA-Interim reanalysis data and the Optimal Interpolated SST database.

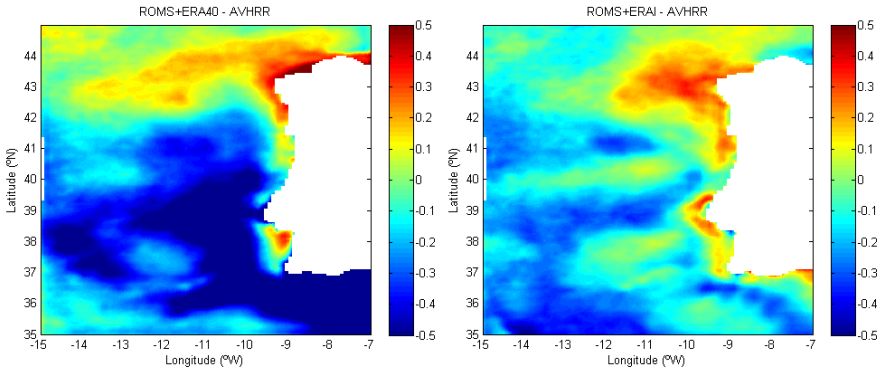

Figure 27 (Left) Mean SST retrieved from the ERA40 forced run minus the observed mean SST (from the OISST database) for the 1989-2001 period. (Right) Same as (left) but for the ERA-Interim forced run.

In the above figures can be clearly noted the improvement achieved in the SST simulated field when the ERA-Interim re-analysis data were used in comparison with the simulation forced by ERA-40. The main SST differences between the two above figures are noted in the southern part of the computational domain, where differences higher than 0.5°C are seen in the simulation forced with ERA-40. In the simulation with ERA-Interim the SST differences in this region are substantially reduced. The mean SST difference in the ERA-Interim forced simulation is lower than 0.4 °C all over the computational domain.

Figure 28 shows the intra-annual variability of SST, computed as the 1989-2001 mean of the intra-annual standard deviation, from the 3 datasets analysed (AVHRR satellite observations, ERA-40 forced ROMS simulations and ERA-Interim forced simulations) and for the common period 1989-2001. Results from the ROMS simulation forced by ERA-Interim are in a better match with observations than those with ERA-40. Observations (and the ERA-Interim simulation) indicate reduced intra-annual variability in the coastal waters, which is associated with cooling in the warmer period.

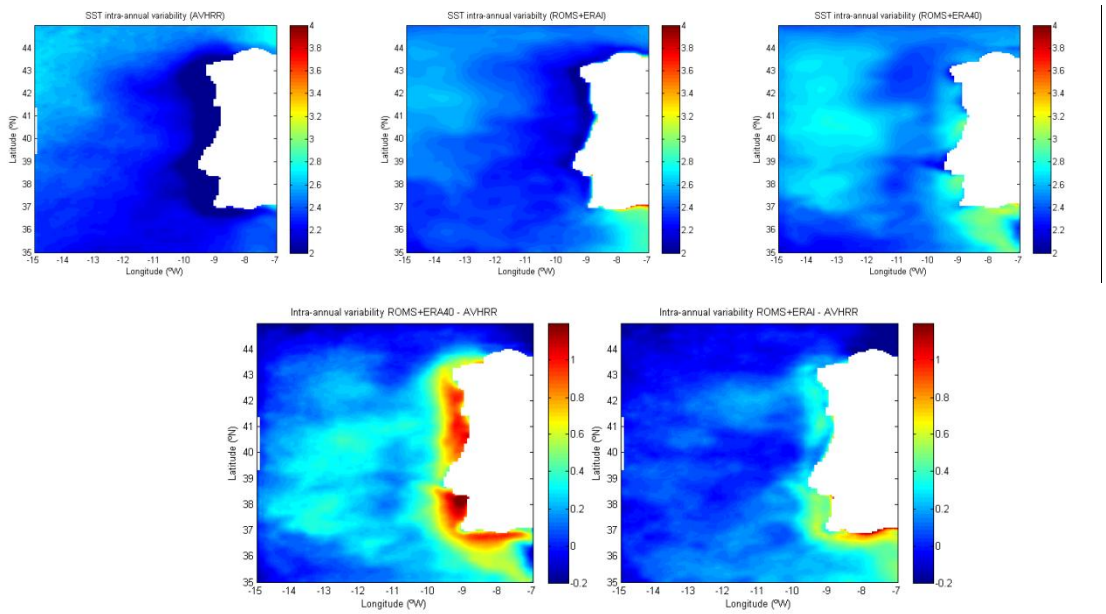

Figure 28 Intra-annual standard deviation of the SST field computed from (upper left) AVHR data; (upper centre) ERA-Interim forced run; (upper right) ERA-40 forced run. The lower panel shows the differences (upper centre)-(upper left) and (upper right)-(upper left).

The variability of the SST field is shown again in Figure 29, which compares the intra-annual and inter-annual variability found in the AVHRR dataset and in the ERA-Interim run. In this case an extended period (1989-2007) is used. Figure 29 (upper-left) is directly comparable with Figure 28 (upper-left), differing only in the extension of the dataset. They are indeed very similar, although there

is slightly more intra-annual variability when taking the longer period. Figure 29 indicates that the coastal region, where intra-annual variability is reduced by upwelling in summer, presents stronger inter-annual variability, at least partially explained by decadal climate trends (keeping in mind that a 20-year period is very short for climate change assessment). Results from the full ERA-Interim simulation (lower-left, lower-right) are qualitatively similar.

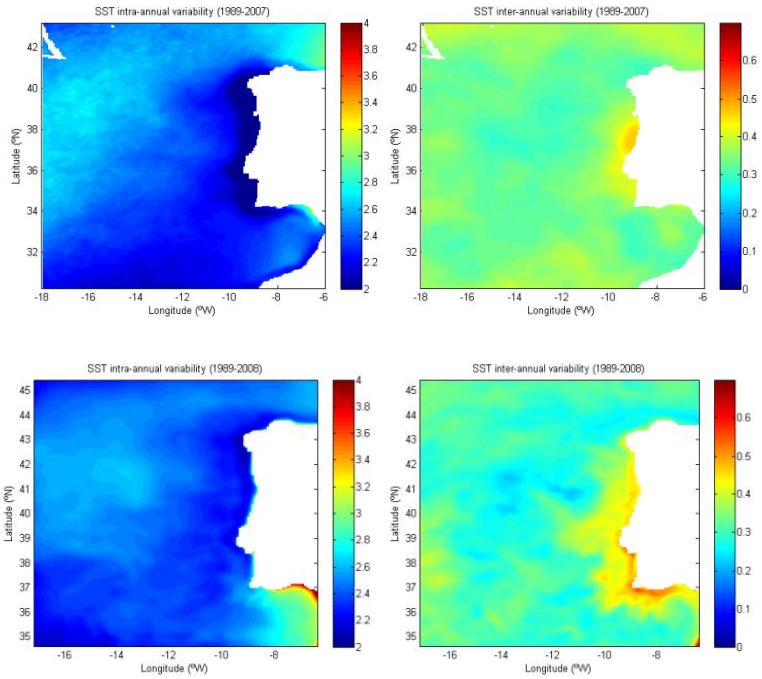

Figure 29 Standard deviation of the SST field: (upper-left) mean of intra-annual standard deviation of AVHRR SST (1989-2007); (upper-right) inter-annual standard deviation of the annual mean of SST AVHRR (1989-2007); (lower-left) as (upper-left) for the ERA-Interim ROMS run (1989-2008); (lower-right) as (upper-right) for the ERA-Interim ROMS run (1989-2008).

4.2 Conclusions

The ROMS simulations forced with the ERA-40 (1961-2001) and the ERA-Interim (1989-2008) re-analyses point to recent decadal trends of coastal upwelling phenomena with opposed signs along the western Iberian coast. The opposing trends in the number of coastal upwelling days were found in the ERA-40 forced simulation from the 80's to the 90's and in the ERA-Interim forced simulation from 1989 until 2008. The SST difference index from both simulations indicated an increasing number of upwelling days in the south and central sectors of the western Iberian coast and a decreasing number of upwelling days in the northern sector. Similar trends were observed with the AVHRR satellite

sensor during 1989-2007. The spatial pattern of the trends is well correlated with that from the meridional component of surface wind. The latter variable (from both the ERA-40 and the ERA-Interim reanalyses) features decreasing northerly wind intensity in the northern and increasing northerly wind intensity in the southern part of the Iberian coast during the summer season.

The main upwelling thermal front is present at about 200 km from the coast in the simulations, although a slight (< 0.5 °C) SST increase at higher distances from the coast indicates that the upwelling front is sporadically present in a region more distant from the coast.

In the simulations, days with pronounced zonal SST gradients are found almost in all months of the year, but just during summer there is clear evidence for coastal upwelling, with a consistent dynamical behavior in the coastal waters: an intensification of the southward and westward surface currents and upward vertical current and a SSH zonal gradient. The lack of this behavior in other seasons of the year supports the conclusion that the lower coastal SST is often not due to the coastal upwelling.

A faster response of the ocean thermal field to variations in the atmospheric surface temperature in shallower regions close to the coast than in the ocean deeper regions was observed in the simulations and also in the satellite data. Indeed, during the spring season the shallow coastal regions warm faster than the deep ocean and during autumn the shallow regions cool faster than the deep ocean.

From the comparison of the 1989-2001 SSTs simulated with the ERA-40 and the ERA-Interim data, it was shown that ROMS forced by the latter dataset produces SST values closer to observations, indicating that the ERA-Interim reanalysis leads to a more realistic ocean forcing.

Chapter 5 Projection of future Iberian upwelling changes using RACMO forcing

In this section results from two 30-year-long ROMS simulations forced by the Regional Atmospheric Climate Model (RACMO) output are presented. The first is a present-climate simulation and corresponds to the period 1961-1990 (hereafter termed control run); the second is a scenario simulation and encompasses the period 2071-2100 (hereafter termed scenario run). The simulations were conducted to assess the impact of climate change in the frequency and intensity of the upwelling off the western Iberian Peninsula. The RACMO surface wind features a slight increase in both its westerly and northerly components during the last 30 years of the XXI century when compared with the control period, resulting in an increase in the number of coastal upwelling events simulated during the scenario period.

5.1 RACMO data and setup of the simulations

The ROMS simulations presented in this chapter were forced with atmospheric data from the RACMO model (van Meijgaard et al., 2008), an atmospheric climate model developed at the Royal Netherlands Meteorological Institute – KNMI. The RACMO data used here corresponds to a simulation with a computational domain that encloses the European continent with a spatial resolution of approximately 0.5°. Those simulations were developed in the framework of the PRUDENCE project (Christensen et al., 2002; Christensen et al., 2007), that was part of a cooperative cluster of projects exploring future changes in extreme events in response to global warming. The RACMO model simulations were forced at the boundaries with data from the HadCM2 global coupled climate model (Cullen, 1993), with a spatial resolution of 2.5° x 3.75°. That model was developed at the Hadley Centre and took into account the greenhouse gases emissions prescribed in the A2 IPCC AR4 climate scenario. The global coupled model resolves 19 levels in the atmosphere and 20 levels in the ocean. The ocean model derives from Cox (1984) and has 20 levels with a maximum resolution near the surface. A 1-day coupling cycle was used, the oceanic component was updated using daily average fluxes of heat, freshwater and momentum from the atmosphere. Prescribed adjustments were made to the heat and freshwater fluxes to reduce errors in the simulation of present climate, as described in Murphy (1995).

The ROMS simulations, with a horizontal resolution of 1/12°, cover the domain shown in Figure 30 and use climatological lateral boundary conditions from the Levitus database (Locarnini et al., 2006). The unavailability of ocean boundary conditions from a global ocean model for the scenario period, justifies the use of climatological data in the present study. This fact restricts the analysis to the impact of regional processes on upwelling, leaving aside possible effects from changes in the large scale ocean circulation.

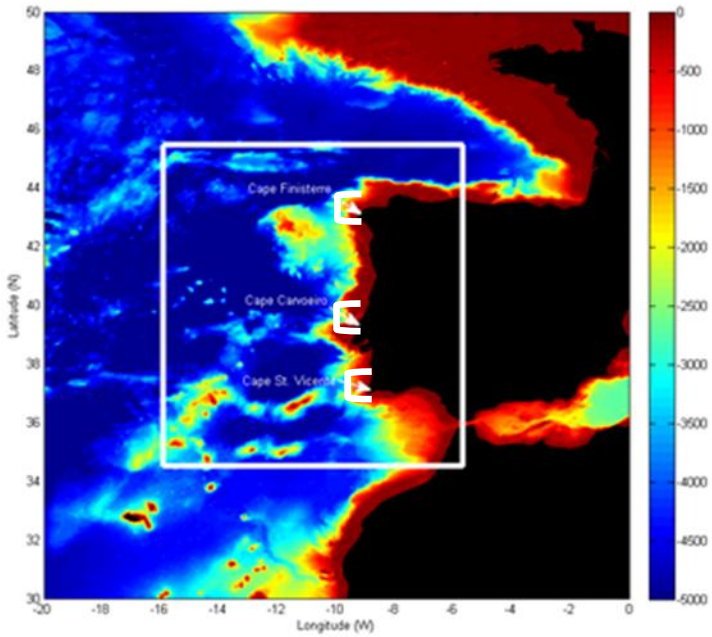

Figure 30 Bathymetry of the domain used in the RACMO-forced simulations. The geographic locations of Cape Finisterre, Cape Carvoeiro and Cape St. Vincent and the associated north, central and south sectors are indicated.

The RACMO simulated surface wind along the western Iberian coast was first analyzed with more detail, in the regions near Cape Finisterre, Cape Carvoeiro and Cape St. Vincent, separately for the control (1961-1990) and scenario (2071-2100) periods. Figure 31 shows mean wind roses computed from RACMO data at the three capes. While results are qualitatively very similar, with the same general structure of the rose at each cape, there is an increase in wind speed from the control to the scenario runs by about 10%. On the other hand, RACMO is consistent with ERA-40 in what concerns the distribution of dominant wind directions, with northeasterly flow at Cape Finisterre, rotating to northwesterly at Cape Carvoeiro and Cape St. Vincent. The wind intensity in RACMO is, however, larger than ERA-40 at all capes.

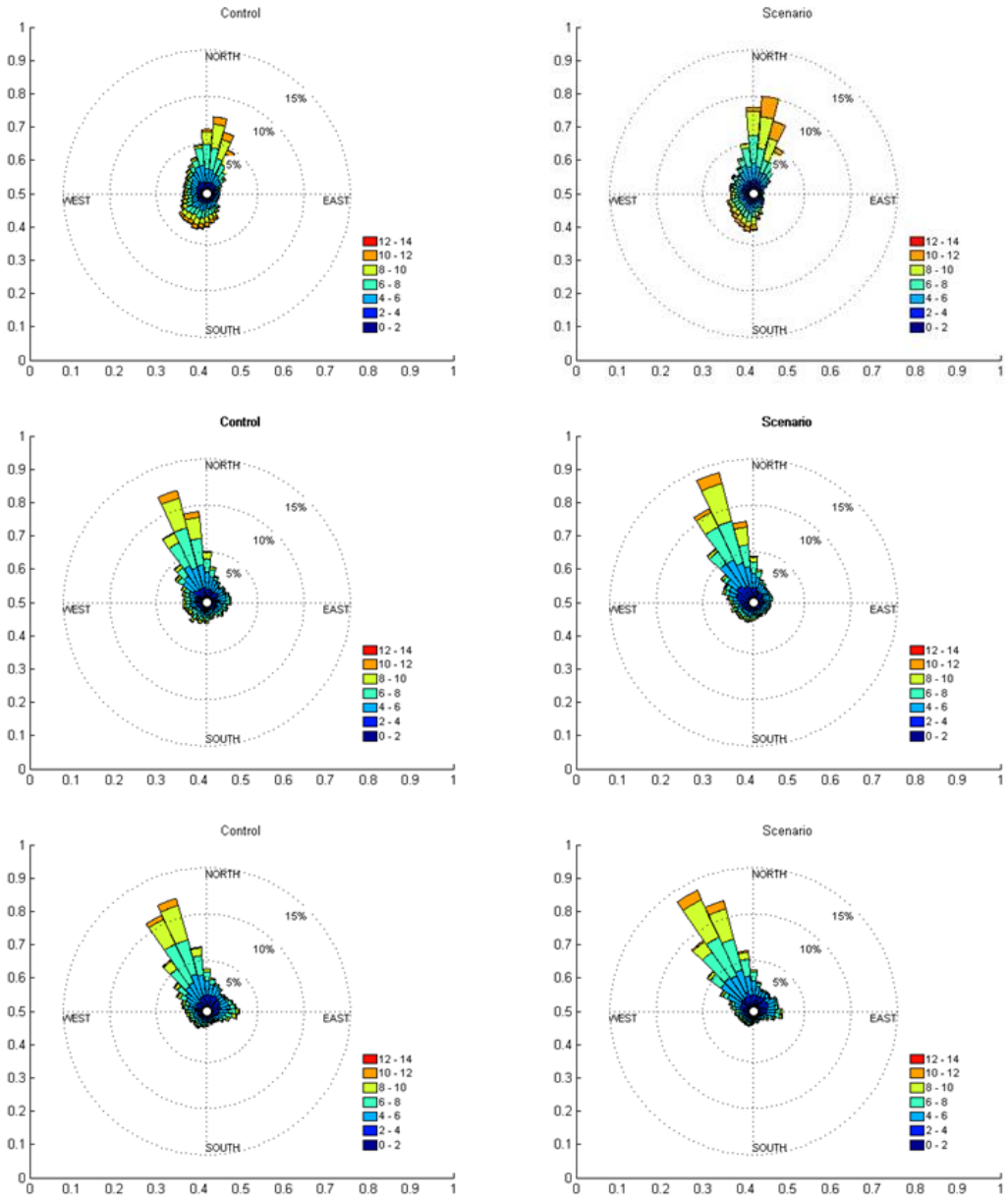

Figure 31 Wind roses of the RACMO surface wind for the control (1961-1990, left) and scenario (2071-2100, right) periods at Cape Finisterre (top row), Cape Carvoeiro (middle row) and Cape St. Vincent (bottom row).

The seasonal wind roses (not shown) for each of the three capes show that the simulated wind direction variability is strongly reduced during the summer season, during both the control and scenario periods. It is also noticed that the increase in wind intensity in the scenario is mainly verified during the summer months (JJA), most probably due to the intensification of two or one of the surface pressure systems responsible by the meridional wind along the western Iberian coast: the Azores anticyclone, on the west side and the Iberian thermal depression on the east side.

Figure 32 shows the differences between the scenario and control RACMO simulated mean fields of surface temperature and pressure. The temperature anomaly goes from nearly 2ºC in the Atlantic to about 5ºC in central Iberia, implying an annual mean increase in the sea-land thermal contrast of about 3ºC. Also noted was a slight decrease in the mean sea level surface pressure, that is more pronounced in the south-west region of Iberia and it is observed all along western Iberia. It should be caused by an intensification of the Iberian thermal Low due to global warming during the XXI century (Figure 32b).

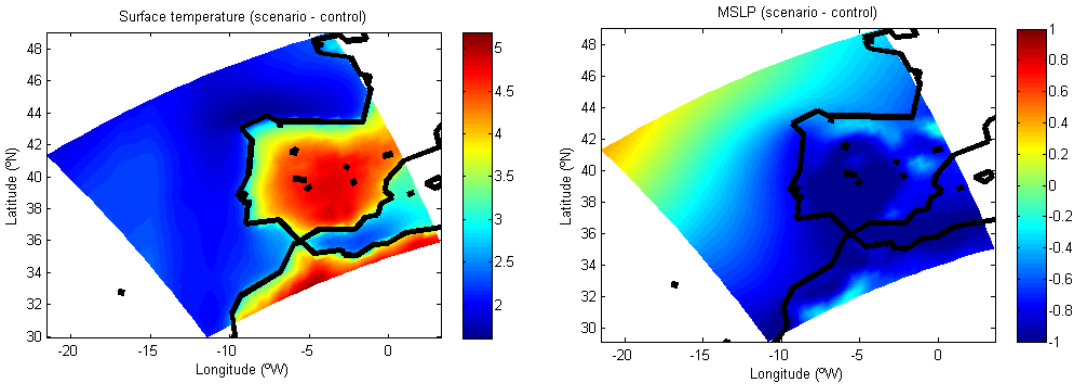

Figure 32 Mean differences (scenario minus control) of : (left) 2m temperature (ºC) and (right) sea level pressure (hPa).

With respect to the other RACMO surface variables used to daily force the ROMS ocean surface, a decrease in the precipitation during the scenario period was verified, which is more significant in the southern part of western Iberian coast. The mean surface air temperature increases by about 2°C at the three capes, with this warming being more pronounced in the south at Cape St. Vincent than in the north at Cape Finisterre. Due to the surface air temperature increase, the mean value of relative humidity suffers a slight increase as well during the scenario period.

5.2 **Results and discussion**

In order to assess the SST inter- and intra-annual variability, Figure 33 shows, for the control and scenario periods, the time-latitude variation of the SST difference between the coast and offshore, so the distribution along the western Iberian coastline.

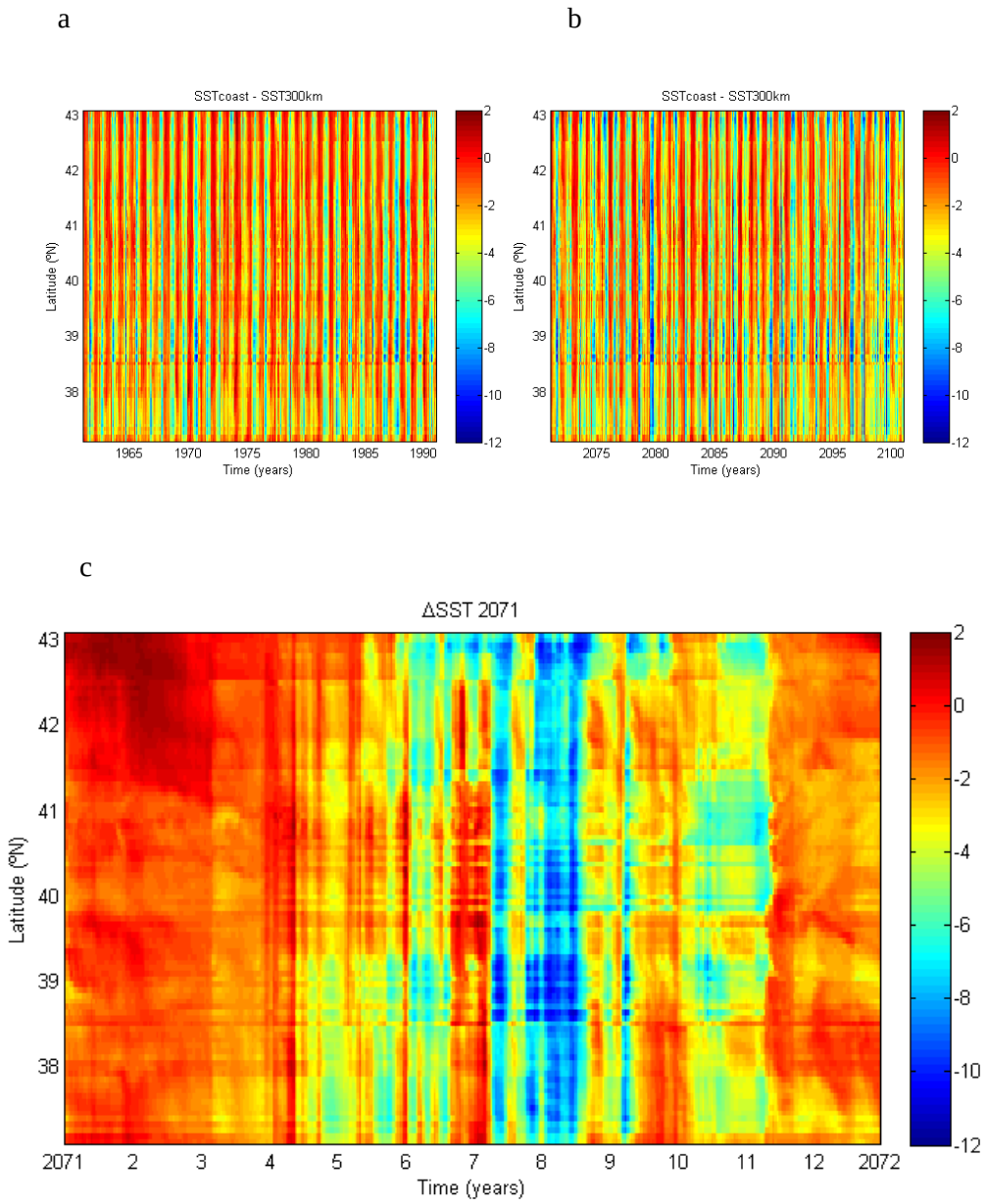

Figure 33 Hovmoeller of SST difference between a line close to the coast and a line 300 km offshore. (a) control period, (b) scenario period and (c) for the year 2071.

In the above figure, the coastal upwelling events are represented by breaks of colder periods observed during the summer season. An increasing intensity of the upwelling events for the scenario period is noticed. The events are better seen in Figure 33c, showing the hovmoeller diagram for the year 2071. The upwelling phenomenon during 2071 is present since May until November, with the most intense simulated events occurring in July and August.

Figure 34 presents the boxplots of SST for the control and scenario periods for the region near each of the three studied capes and for a region located 300 km offshore. As before, in the boxplots here presented the edges of the box represent the 25th and 75th percentiles, the red line is the median and the green point is the mean value. Points are drawn as outliers (red points) if they are larger than $q_3 + 1.5 \times (q_3 - q_1)$ or smaller than $q_1 + 1.5 \times (q_3 - q_1)$, where q_1 and q_3 are the 25th and 75th percentiles, respectively.

In the figure it can be seen that the SST increase between the control and scenario periods is always higher in the point located 300 km to the west of each cape than in the nearshore location. This could be interpreted as a consequence of increasing upwelling leading to reduced warming of coastal ocean surface water. It is also noteworthy that the coastal SST warming is slightly more pronounced in the southern region, as also seen in the near surface atmospheric temperatures. Inter-annual variability of SST is also higher in the scenario run, in the north and central sectors, for both nearshore and offshore waters. In the southern point variability increases only slightly in the nearshore and not at all offshore.

The coastal upwelling season (i.e., the summer) is characterized by an intensification of the southward and westward coastal surface currents. The ROMS simulations reveal a slight increase in the mean westward and southward surface currents during the scenario period, consistent with the reinforcement of coastal upwelling. This can be seen in the boxplots of the two surface velocity components for the region near Cape Carvoeiro (Figure 35a).

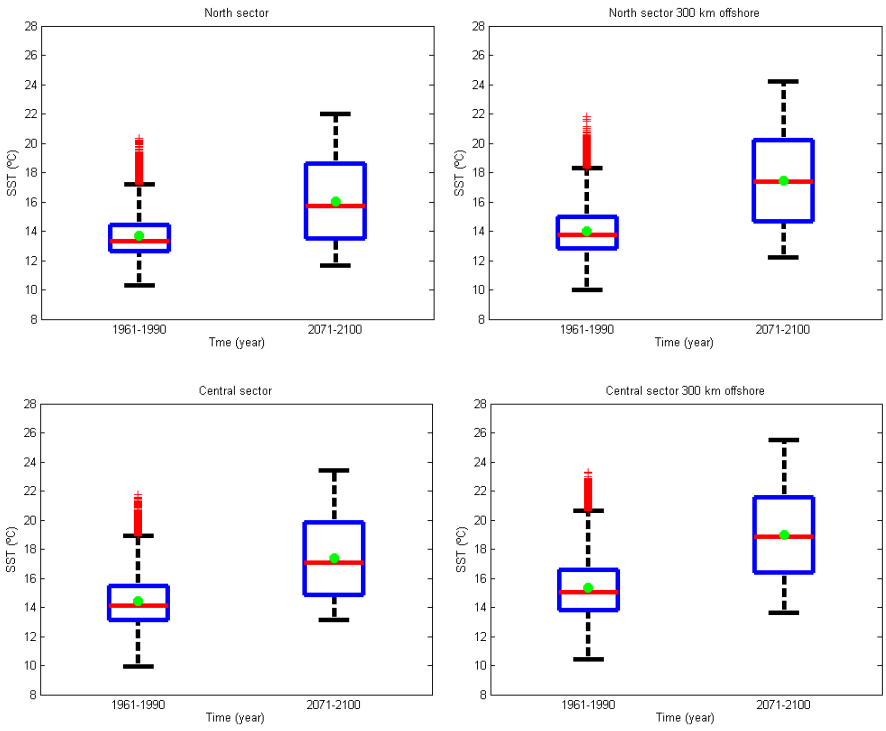

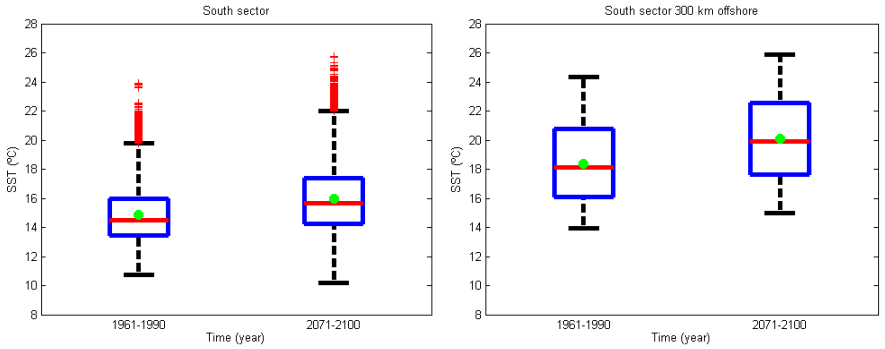

Figure 34 Boxplots of SST in a point close to the coast (left column) and other located 300 km offshore (right column) for the control and scenario periods and for three sectors along the Iberian coast.

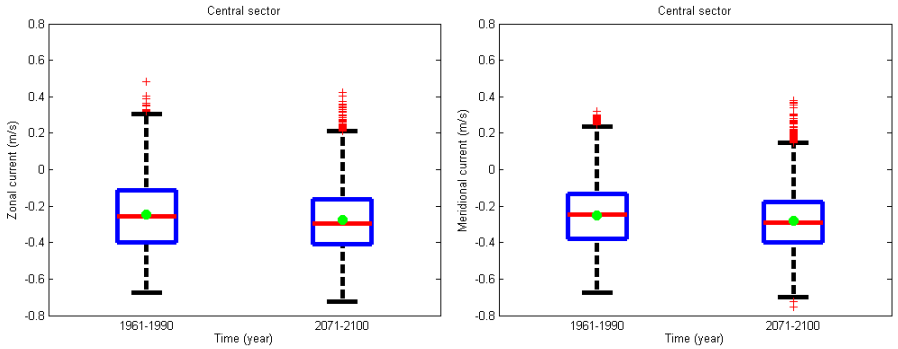

(a)

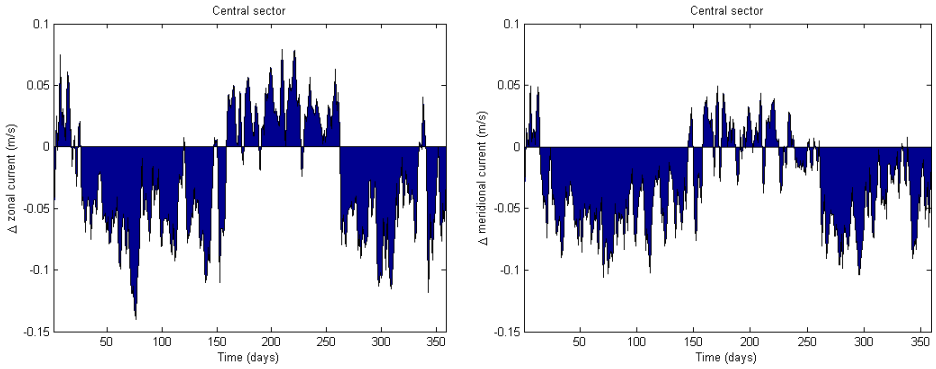

(b)

Figure 35 a) Boxplots of zonal and meridional components of surface currents off Cape Carvoeiro for the RACMO control and scenario periods. b) Yearly difference in mean zonal and meridional components of surface currents between the control and scenario simulations.

Figure 35b shows that the intensification of zonal and meridional surface currents is verified during all seasons of the year except in summer, when a slight decrease (< 0.05 $m.s^{-1}$) of the zonal and meridional surface currents is visible. This result indicates that the increasing mean annual number of upwelling days towards the end of the XXI century is mostly verified during the winter, spring and autumn seasons.

In order to identify trends in the Iberian coastal upwelling, it is useful to define an upwelling index. The index proposed here is given by the number of days per year with a coast-offshore SST difference larger than 2°C. Consistently with the increasing intensity of the RACMO meridional wind forcing, one founds an increase in the mean number of days per year with a SST difference higher than 2°C (Figure 36). At the three capes the median of the index goes up by more than 20% between the control and the scenario periods.

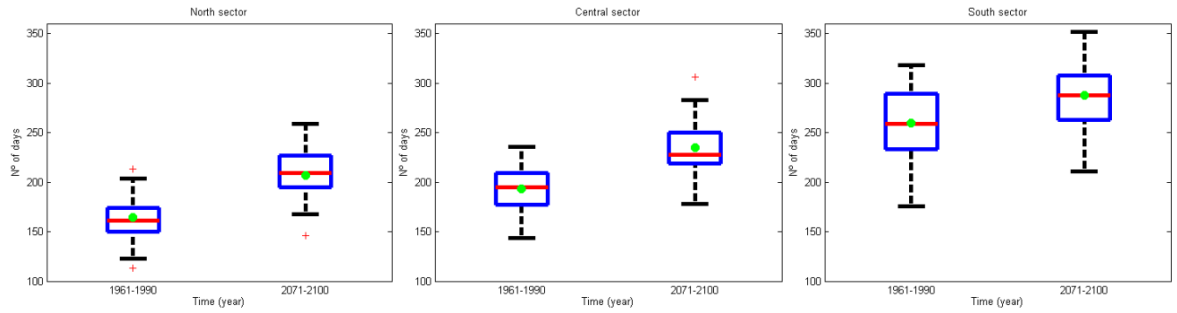

Figure 36 Boxplots of the number of days with a difference of sea surface temperature greater than 2°C between a point close to Cape Carvoeiro and other located 300 km offshore.

In order to characterize the intensity of coastal upwelling events, Figure 37 shows the boxplots of the mean number of days per year with ΔSST between 2°C and 3°C, between 3°C and 4°C, and higher than 4°C.

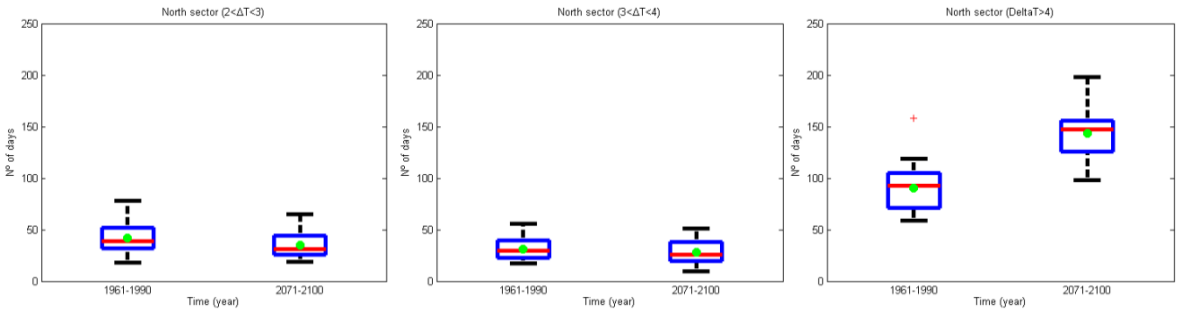

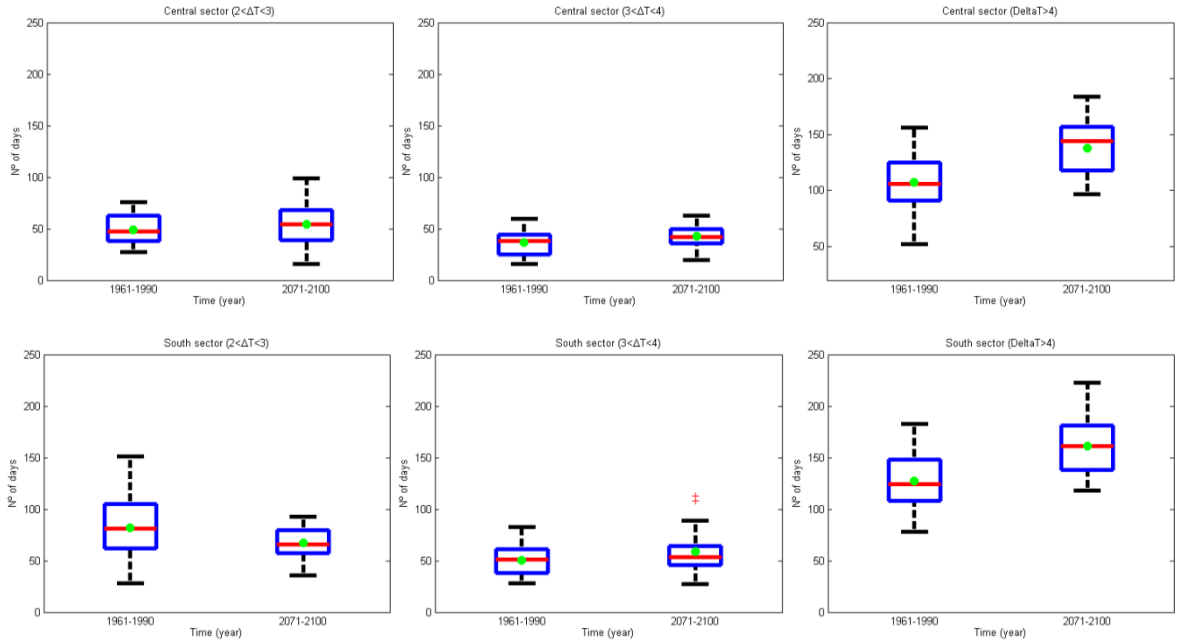

Figure 37 Boxplots of the number of days with SST difference of (left column) 2°C<ΔSST<3°C, (middle column) 3°C<ΔSST<4°C and (right column) ΔSST>4°C between a region near Cape Finisterre (top row), Cape Carvoeiro (middle row) and Cape St. Vincent (bottom row) and a point located 300 km offshore.

From these figures it can be noticed that the number of the less intense events (2°C < ΔSST < 3°C) does not change much in the scenario period. Indeed, the mean value of the less intense events suffers just a slight decrease at Capes Finisterre and St. Vincent and a slight increase at Cape Carvoeiro, with an overall decrease of inter-annual variability at all capes. The middle intensity events (3°C < ΔSST < 4°C) experience almost no change in their median and mean values. More important, one observes a higher frequency of the more intense events (ΔSST > 4°C). The latter increase is more relevant at Capes Finisterre and Carvoeiro, where it is accompanied by an increase in inter-annual variability. In short, the results suggest that the upwelling off the western Iberian coast is likely to increase in the global warming scenario, mostly due to a higher frequency of more intense events.

From the analyses of the modeled SST fields it was noted that during the winter season the number of events with different intensities is much more equally distributed than during the summer season when the majority of events are the more intense ones (ΔSST > 4ºC).

The occurrence of a coastal upwelling event implies a zonal SSH gradient in the coastal ocean, with lower SSH close to the coast and higher SSH in the far region. This zonal gradient occurs due to the offshore convergence of the ocean upper layers.

A decrease in the mean SSH in the scenario period near each cape can be noted from the SSH boxplots in Figure 38. The mean SSH increases at the location 300 km offshore from Capes St. Vincent and

Carvoeiro and decreases offshore from Cape Finisterre. The onshore decrease in the mean SSH value can be interpreted as a consequence of a stronger upwelling. The simulated SSH increase at the open ocean offshore from the coast can be interpreted as a consequence of ocean warming, which implies a thermal dilatation of the ocean surface water (steric effect). Contrary to the general behavior, however, offshore from Cape Finisterre there is an SSH decrease. This feature is here attributed to regional, long and persistent filaments usually observed off this cape, effectively extending the coastal effect farther offshore and due to a lower surface air warming in this region. In short, the impact of upwelling on SSH seems to be strong enough to overcome the contradictory trend of mean SSH increase resulting from global warming.

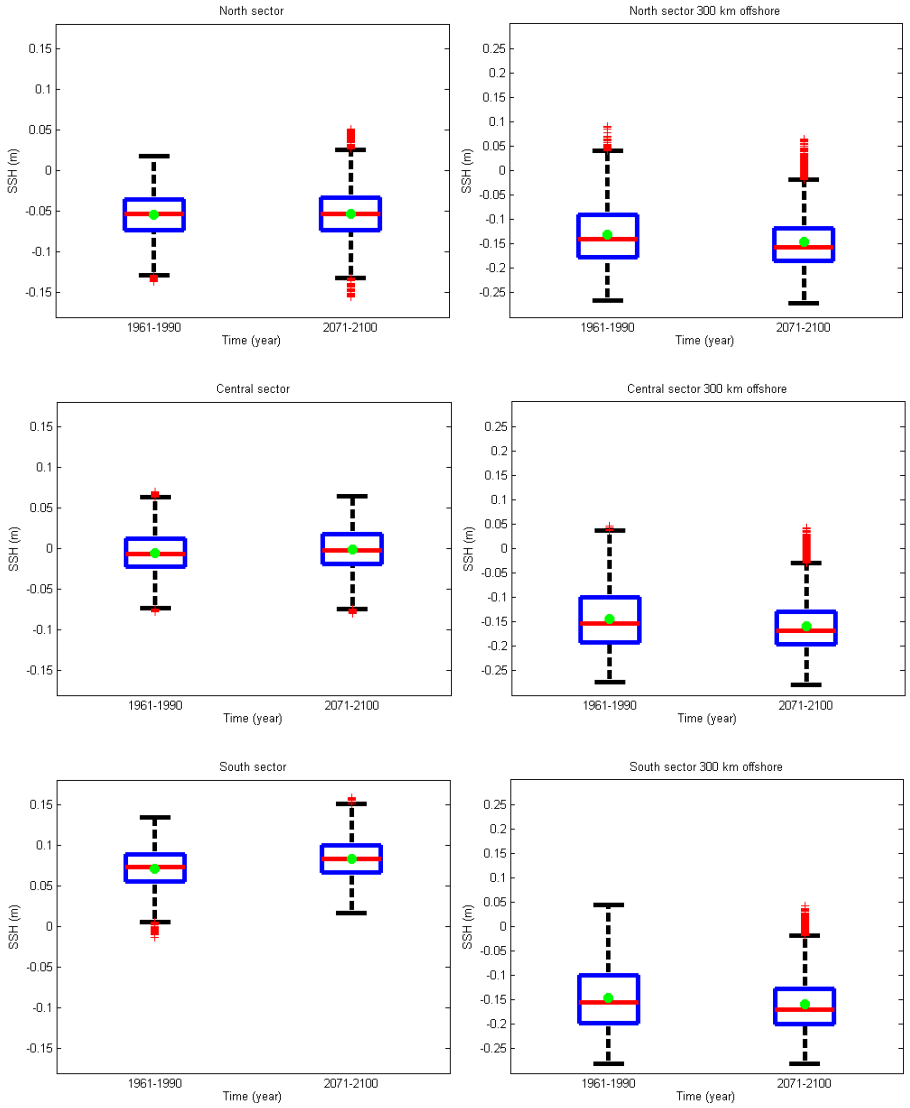

Figure 38 Boxplots of the mean SSH (m) in different sectors for the control and scenario periods along the Iberian coast: (left column) close to the coast and (right column) 300 km offshore.

Figure 39 shows the seasonal differences between the scenario and control periods for mean SST and for SST standard deviation. A lower increase of SST is observed in coastal waters, in all seasons, a consequence of the increasing upwelling along the year. The highest mean seasonal SST increase (about 3.5ºC) in coastal waters is verified during autumn, accompanied by increased intra-annual variability. Spring coastal SST is almost unaffected by global warming, with even a small SST decrease in the nearshore (< 1ºC). During summer, an SST increase is noted in the south and central parts of the coast, but in the north, particularly near Cape Finisterre, one finds a significant mean SST decrease, of about 2ºC, in the scenario period. It is in this region that the highest increase of intra-annual variability is verified, pointing to increased upwelling in the northwest extreme of the western Iberian coast, during summer, for the scenario period. The expected increase in the intra-annual variability, due to the increasing number of upwelling days, is mostly noted in the two extreme seasons: winter and summer.

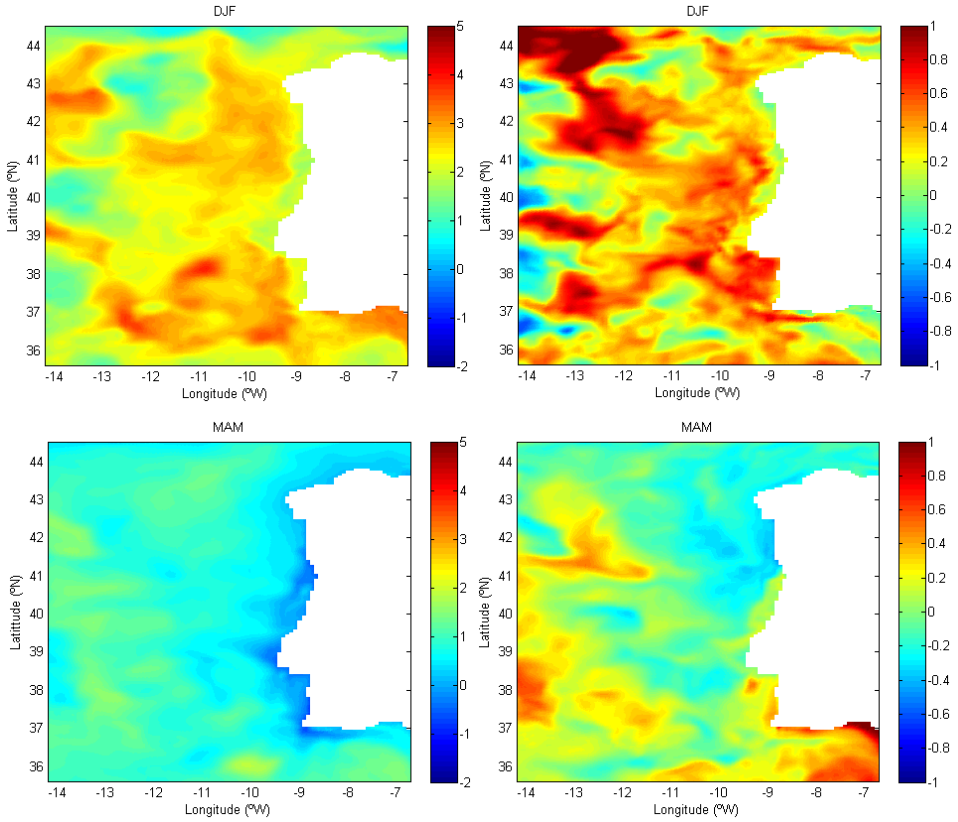

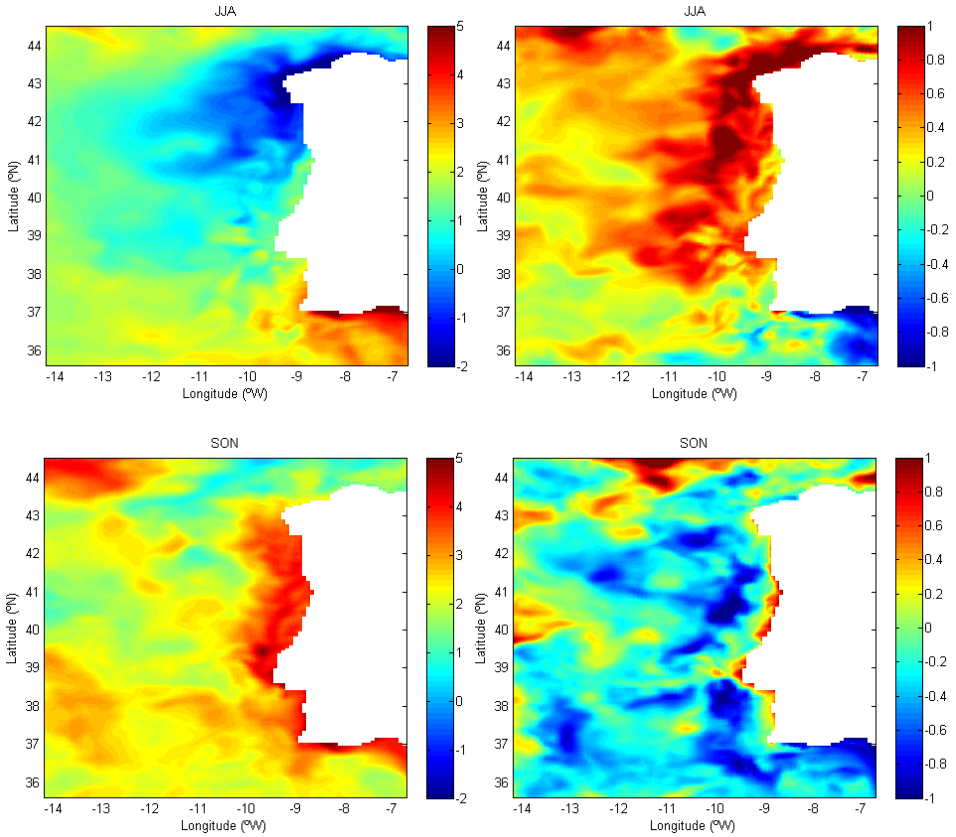

Figure 39 (Left) Mean SST for the scenario run minus the mean SST for the control run, split into seasons. (Right) Difference in inter-annual averages of the SST intra-annual standard deviation.

Figure 40 presents the mean SST at a sector close to each of the three capes (green line) and at a sector located 300 km offshore (red line), for each day of a mean year for the control and scenario periods. In spite of the cancellation that results from multiyear averaging of upwelling events, which occur at essentially random dates during the upwelling season, the nearshore mean annual cycle keeps evidence of intense SST variability associated with those events. On the other hand, offshore areas present a much smoother behavior. Global warming is clearly evident in the offshore points, where an upward shift in SST of 1 to 2 °C along the year is noted.

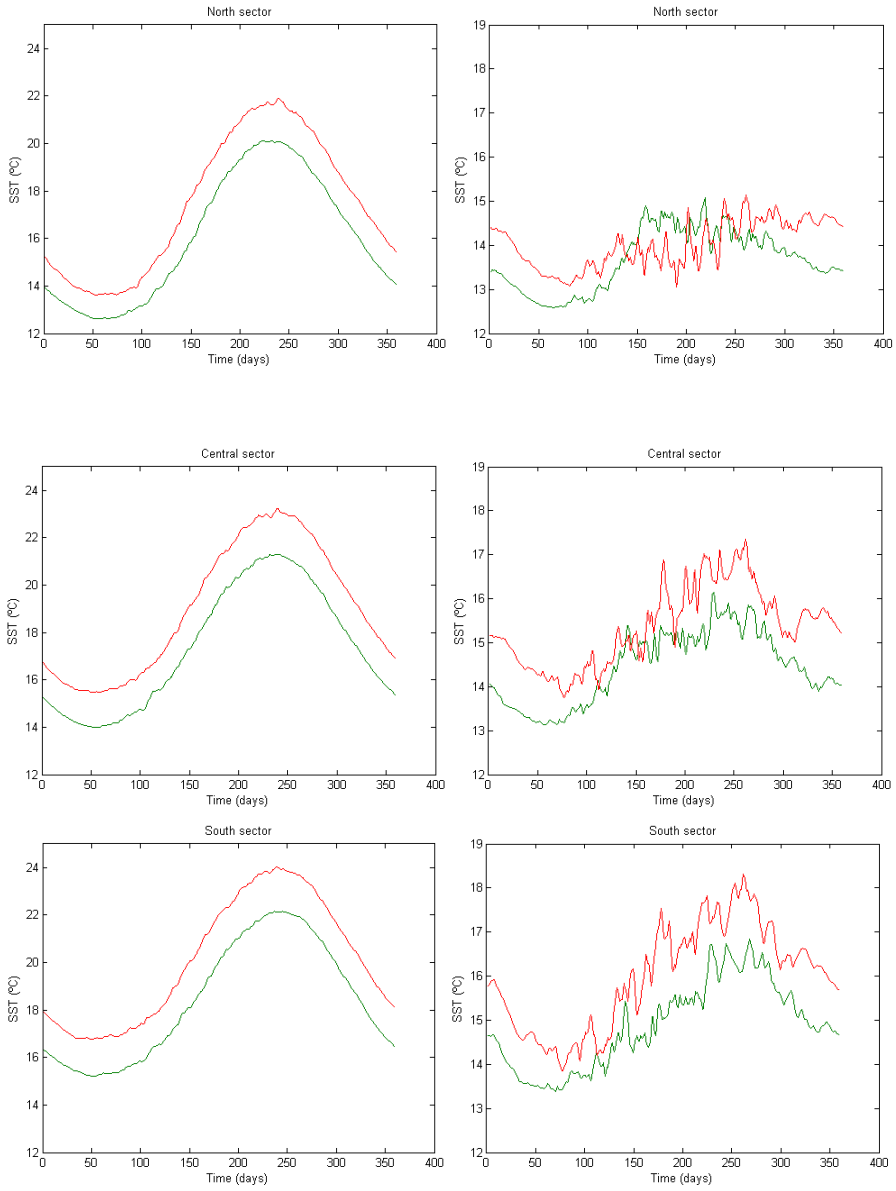
North sector
North sector
Central sector
Central sector
South sector
South sector
SST (ºC)
Time (days)

a)

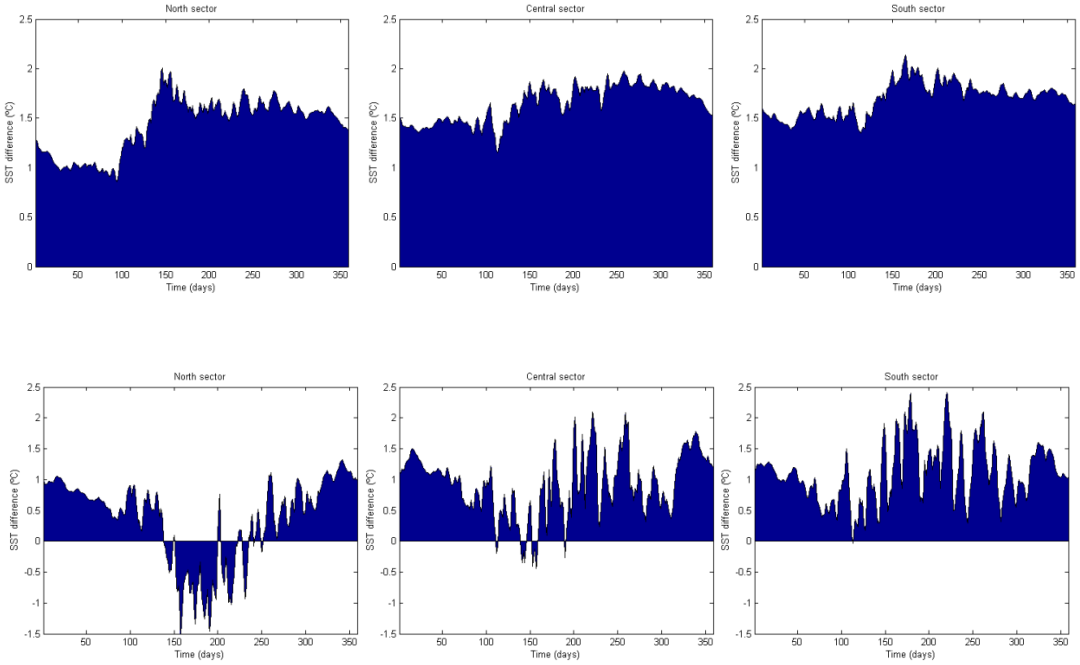

b)

Figure 40 a) Mean annual cycle of sea surface temperature at a sector close to Cape Finisterre, Cape Carvoeiro and Cape St. Vincent (right column) and at a sector located at the same latitude 300 km offshore (left column), for the control (green lines) and scenario (red lines) periods. b) Mean annual SST for the scenario period minus mean annual SST for the control period, for the sectors located 300 offshore (upper) and for the sectors located close to the coast.

Figure 40 shows that near Cape Finisterre summer upwelling is strong enough to invert the mean annual cycle, which is characterized by rather small amplitude even during the control period. At Capes Carvoeiro and St. Vincent, during the scenario period, the highest SST along the year continues to be observed at the end of summer and the lowest annual SSTs continue to be observed at the end of the winter season. In the three offshore sectors, the SST difference between the control and scenario experiments has an average value of 1.5 ºC that is maintained almost constant along the year. In the sectors close to the coast the SST difference variability is much higher along the year, and the SST difference between the two simulations, is on average much smaller than the one observed 300 km offshore. While global warming at the offshore locations is more intense in the second half of the year, especially at Cape Finisterre where it jumps from about 1ºC in January and February to more than 1.5ºC from June until November, in the nearshore the warming is not enhanced in the warmer seasons and there is evidence of the effect of upwelling in a much extended summer season.

5.3 Conclusions

The analysis of the numerical simulations conducted with ROMS forced with RACMO atmospheric data, for a present climate (control) and for a future climate (scenario), indicates an increased frequency of coastal upwelling towards the end of the 21st century. This positive trend was noted in the simulated SST, SSH and surface currents.

The SST field showed an increase of the yearly mean number of days with cold coastal waters, defined by the difference in SST between a region close to the coast and another located 300 km offshore at the same latitude. This trend is stronger in the case of more intense upwelling events ($\Delta SST > 4°C$). For the less intense events ($2°C < \Delta SST < 3°C$) the increase is less clear and a reduction was even noted at Capes Finisterre and St. Vicent. A slight increase of the zonal and meridional components of the surface currents at Cape Carvoeiro region was also noticed and attributed to the increased coastal upwelling in the period 2071-2100. The increase in surface current intensity is verified along the year except during the summer season.

The SSH field experiences an upward trend at the offshore sectors (except in the northern one) and a downward trend at the corresponding sectors near the coast, which is consistent with an increase of upwelling during the scenario period. Coastal upwelling implies a lower coastal SSH, but this is opposed by sea level changes due to thermal expansion of the ocean. The present results suggest that the former effect is dominant.

With respect to the seasonality of the coastal SST, it was noted that the highest coastal SST increase is verified during the autumn season, along the entire western Iberian coast. During summer in the northwestern extreme of Iberia, a SST decrease was noted, which points to an increase of upwelling events in that region that overlays the global warming effect.

Chapter 6 **Improving the Iberian upwelling simulations with a coupled ocean-atmosphere model**

This chapter presents results from simulations conducted with the COAWST coupled ocean-atmosphere-wave model. These simulations have potentially some advantages over the ROMS-only runs presented in Chapters 4 and 5. For instance, the coupled model allows the study of the effects of surface waves on the SST field and thus to simulate, almost in real-time, their impact on the heat and momentum fluxes at the ocean-atmosphere interface. The coupled system allows the study of feedback mechanisms associated with the coastal upwelling. A positive feedback mechanism is observed when the intensification of coastal upwelling (lower SST) increases the zonal surface temperature gradient, which will intensify the northerly wind, causing a further intensification of coastal upwelling. A negative feedback mechanism relates to the onshore advection of cool maritime air, decreasing the zonal surface atmospheric temperature gradient, which consequently decreases the northerly wind and thus the coastal upwelling intensity. However, in spite of the more complete physics available in the coupled system, the coupled model has more degrees of freedom and is loosely controlled by the imposed boundary conditions. As a consequence, results cannot be analyzed in terms of simple error statistics, which in general will turn out to be worse than those of the uncoupled model.

6.1 **Previous upwelling coupled modeling studies**

Jin et al. (2009) analyzed two 240 days-long simulations with ROMS, one without air-sea coupling, where the ocean surface was forced by a background constant wind stress, and another including the coupling, where the cold nearshore upwelling-related SST substantially weakened the surface wind field in the nearshore area, introducing spatial variations on the surface wind forcing. As a consequence, the authors noted a weaker upwelling and a higher coastal SST in the coupled experiment. Another consequence of the nearshore surface wind weakening in the coupled experiment was a 25% smaller eddy kinetic energy field at the ocean surface during the equilibrium phase of the coupled simulation. An increasing and broadening of the poleward undercurrent in the coupled simulation was also found.

Upwelling modeling studies with coupled systems including ocean, atmosphere and wave models are still in its infancy and few articles have been published to date based on fully coupled systems.

In an idealized experiment, Perlin et al. (2007), using a coupled modeling system comprising the COAMPS (Couple Ocean–Atmosphere Mesoscale Prediction System; Hodur 1997) and the ROMS model, noted a nearly two-fold decrease in the meridional wind stress, from a point located 25 km from the coast to a point near the coast, due to the SST variability. A similar wind stress decrease was also noted by Dorman et al. (2006) when analyzing observational data from an array of buoys and coastal stations over the shelf of Bodega bay, California. Perlin et al. (2007), besides a weaker nearshore wind stress, found reduced vertical mixing in the coupled case and saw that the coastal Ekman transport divergence was distributed over a wider offshore extent and a thinner ocean surface boundary layer. This led to a consistently smaller offshore and depth-integrated alongshore transport in the coupled when compared to the uncoupled experiment. The thinner Ekman boundary layer delayed the merging of the surface and bottom boundary layers over the inner shelf and allowed further inshore propagation of the bottom upwelling front. Consequently, within 2 km from the coast, local cross-shore transport estimates were slightly larger and SST slightly cooler (approximately 0.5 ºC) in the coupled case.

More recently, using the same coupled system, in an idealized domain that resembled an ocean eastern boundary coastal upwelling system with a single cape protruding into the ocean, Perlin et al. (2011) noted that the upwelling front doubled in width on the lee side of the cape. The lowest SSTs were found near the coast in that cape region, where a significant decrease in SST-wind stress coupling is observed. The authors therefore noted that strong orographic forcing is found to weaken the average wind stress-SST coupling computed for the 100-km coastal zone.

Seo et al. (2007) applied the SCOAR (Scripps Coupled Ocean–Atmosphere Regional) model, which consists of the ROMS oceanic model coupled to the Regional Spectral atmospheric Model (RSM), to the Eastern Pacific region. The authors reported an acceleration of surface wind and enhanced turbulent heat flux over warmer SST. The net heat flux in the coupled case increased from unstable atmospheric conditions in the offshore region (upward net flux of about 86 W m^{-2}) to nearly neutral or weakly stable conditions near the coast (downward net heat flux of 7 W m^{-2}) in the 72-hour forecast due to the low coastal SSTs.

It is known that stability within the atmospheric boundary layer changes as the surface wind blows across an SST front (Wallace et al., 1989). This results in an acceleration of surface wind and enhanced turbulent heat flux over warmer SST. From the analysis of surface wind stress and SST data, Chelton et al. (2007) noted that SST is positively correlated with wind stress when SST fronts are strong, which is normally the case in eastern boundary coastal upwelling regions. This correlation is apparently due to a SST modification of stability and mixing in the atmospheric boundary layer. These authors also noted that the spatial variability of this SST influence in the vicinity of SST fronts

generates wind stress curl and divergence that are linearly related to, respectively, the crosswind and downwind components of the local SST gradient, as also noted by Seo et al. (2007).

O'Neill et al. (2010), analyzing wind stress data from the QuikSCAT sensor and SST data from AMSRE-E sensor for the June 2002-August 2008 period, also noted a linear relation between wind stress curl and divergence and the crosswind and downwind components of the SST gradient, respectively. In addition, they showed that surface winds accelerate and turn anticyclonically when the surface wind blows from cool to warm SST and decelerate and turn cyclonically when the surface wind blows from warm to cool SST, with typical wind speeds changes of 1-2 ms^{-1} and wind directions changes of 4°- 8°.

6.2 Results and discussion

The COAWST coupled system simulates the coastal upwelling off Iberia, as is illustrated in Figure 41, which shows the SST and a cross-section of the ocean temperature during a coastal upwelling event in August 2002. These results stem from a fully couple experiment, in which WRF, ROMS and SWAN are coupled (setup C in Figure 7).

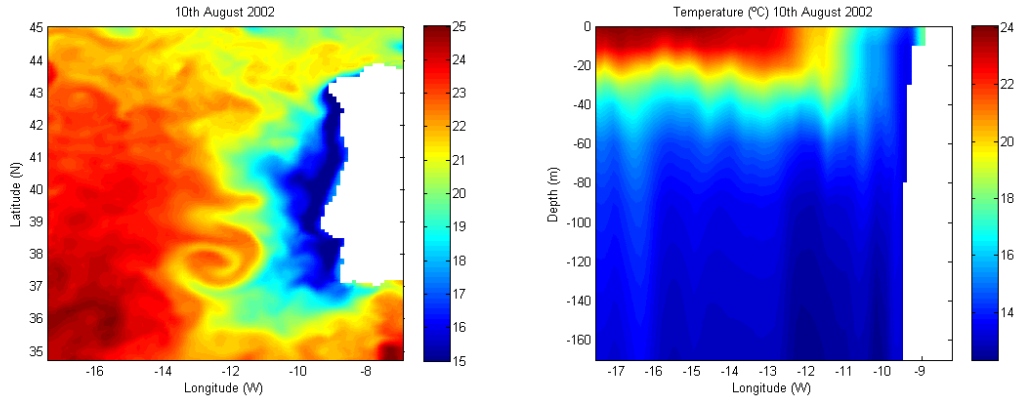

Figure 41 Simulated (left) mean sea surface temperature and (right) cross-section of mean ocean temperature off Cape Carvoeiro, for August 2002, retrieved from an experiment with WRF,ROMS and SWAN coupled.

Figure 41 shows that a coastal upwelling front extending to a distance of about 180 km offshore from the western Iberian coast. To the west of Cape St. Vincent a filament that reaches larger distances from the coast is clearly visible. In Figure 41-right the uplift of the isotherms close to the coast is observed, implying a zonal coastal SST gradient. In the offshore region, the largest temperature vertical gradient occurs in the upper 50 m, whereas in the region closer to the coast the upper ocean

vertical gradient is substantially reduced during the coastal upwelling event. In the computational cell close to the coast a slight SST warming is noticed. In that region the benthic and surface Ekman boundary layers are usually superimposed and, as a consequence, the zonal transports are partially cancelled and the upwelling of cool waters is not verified, or at least has lower intensity.

The COAWST system includes the SWAN ocean wave model. In order to assess the impact of the sea surface waves on the SST field, a simulation using ROMS coupled to WRF was compared to a simulation using ROMS, WRF and SWAN. Figure 42 presents the mean seasonal SST differences between the simulations including and excluding the wave model.

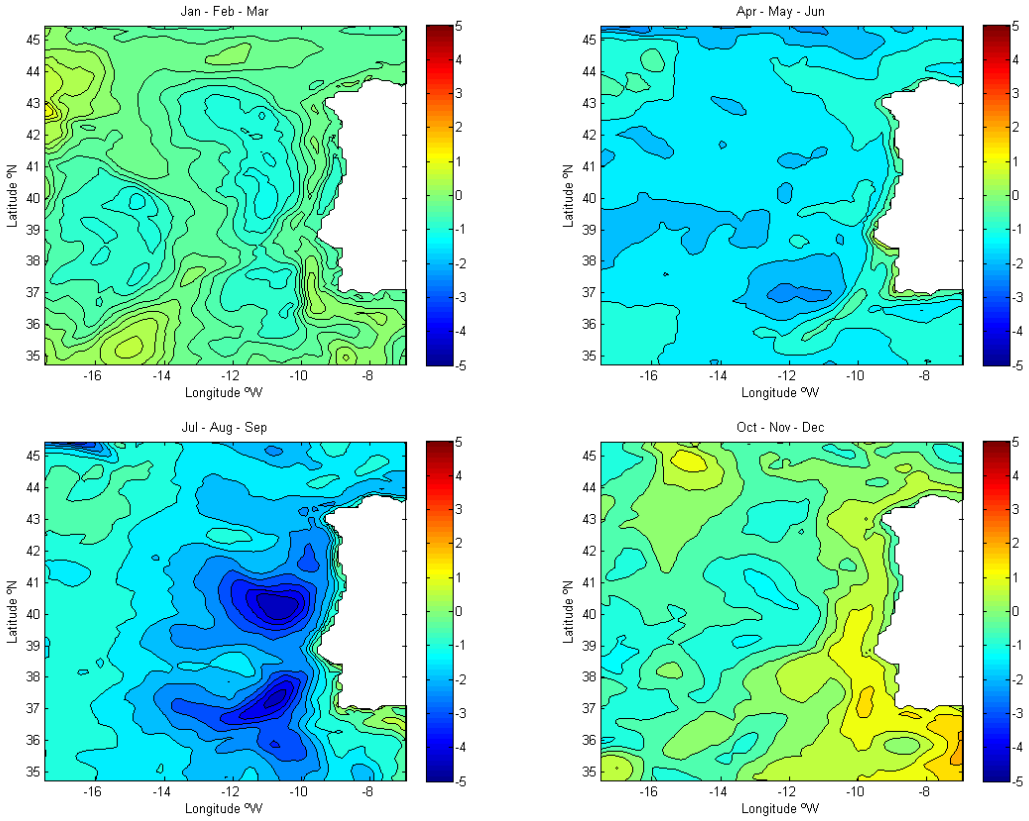

Figure 42 Mean seasonal SST differences for the year 2002 between an ocean-atmosphere coupled simulation and an ocean-wave-atmosphere coupled simulation (WRF+ROMS+SWAN minus WRF+ROMS).

During most of the year the SST differences between the two simulations are below 1°C, with the exception of the summer months of July, August and September, when a lower SST is observed in some regions (between 2 and 3.5 °C). The latter can potentially be due to increased mixing in the ocean boundary layer caused by the ocean surface waves.

Figure 43 shows the seasonally-averaged significant wave heights (wave directions are superimposed – see dark arrows) computed by SWAN for the year 2002.

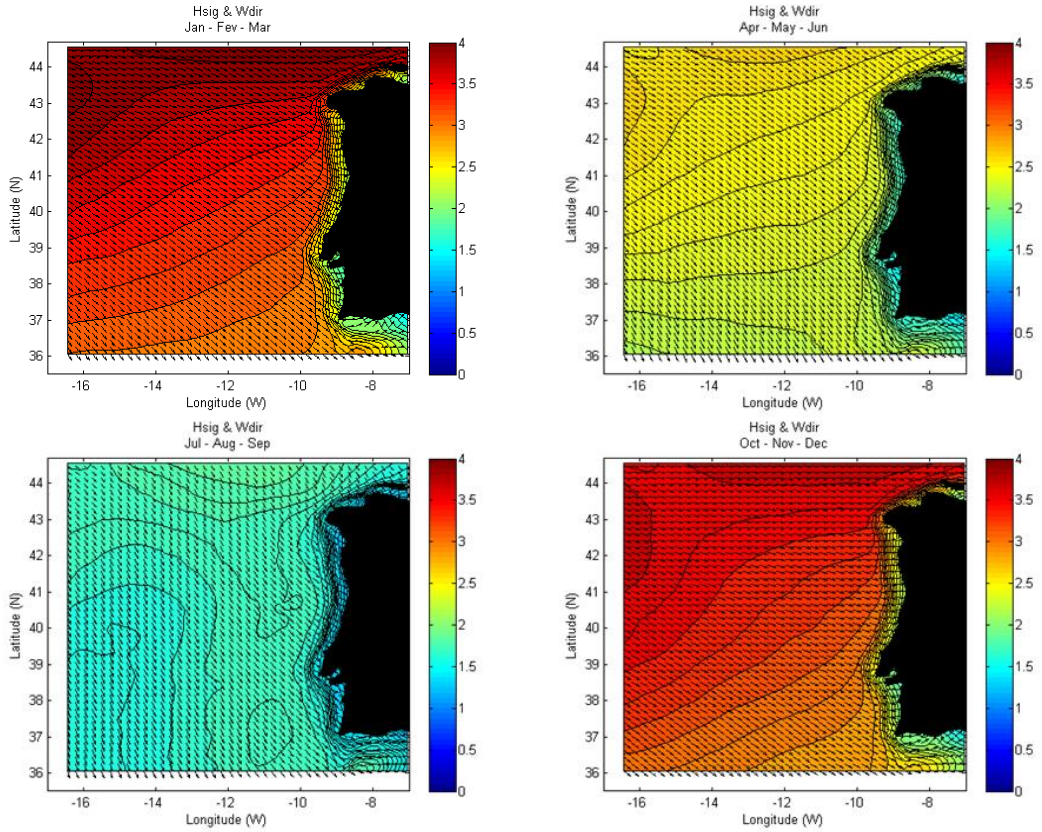

Figure 43 Mean seasonal significant wave height (contours) and direction (arrows) for the year 2002 obtained from a WRF+ROMS+SWAN coupled simulation.

Figure 43 shows that the highest seasonal mean significant wave heights (of about 4 m) are observed during the winter season in the northwestern part of the domain, and that the lowest mean significant wave heights occur during summer close to the coast. In all seasons, a strong meridional gradient is observed along the western Iberian coast. Furthermore, the mean wave direction is essentially unchanged along the year, having predominantly a northwest-southeast direction.

Despite the mean significant wave height field being much higher in winter (Figure 43), it seems that the impact of the ocean surface waves on the SST field is found to be more intense in summer, as shown in Figure 42. This apparent contradiction is explained simply because the upper ocean vertical temperature gradient is much larger in summer than in the rest of the year (Figure 44). During spring and autumn the vertical gradient has a value that is approximately half of its summer value, and the ocean temperature vertical gradient is almost null during the winter season in the top 100 m. In the

presence of a larger vertical gradient in summer, the surface waves have more impact on the temperature mixing.

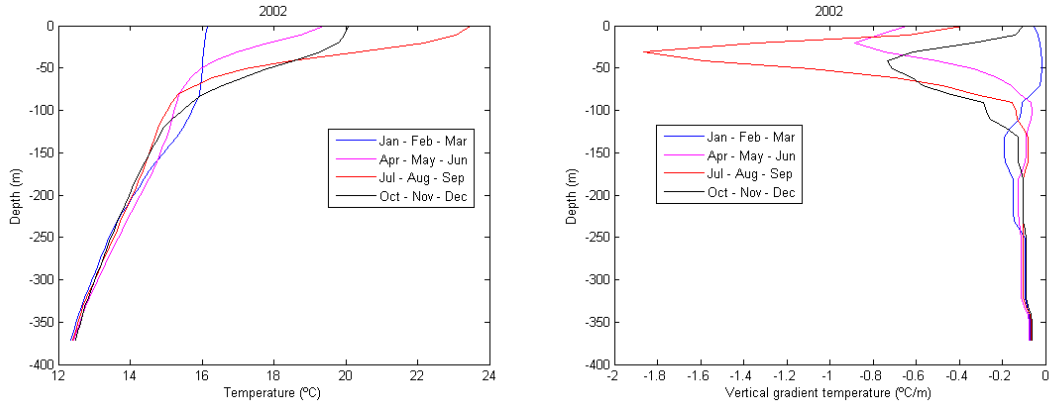

Figure 44 (left) Mean seasonal SST profiles off western Iberia and (right) associated vertical gradient, obtained from a WRF+ROMS+SWAN coupled simulation.

With respect to the impact of ocean surface waves on the simulated surface winds, only minor differences were observed (smaller than 1 $m.s^{-1}$) between the WRF+ROMS+SWAN and the WRF+ROMS experiments (not shown), with higher surface winds in the WRF+ROMS+SWAN experiment probably due to decreased ocean stability associated with the wave-induced lower SST and increased turbulence in the marine atmospheric boundary layer.

Figure 45 shows the mean seasonal difference of the WRF-simulated surface atmospheric temperature field between the experiments excluding and including SWAN. The largest impact of wave coupling on atmospheric surface temperatures (of the order of 2-3°C) are verified during summer, as already noted in Figures 42 for SST. It is also noted that the surface atmospheric temperature is usually colder in the WRF+ROMS+SWAN experiment than in the WRF+ROMS experiment, with the exception of the southeastern sector of the computational domain during the autumn season. Over land the impact of the inclusion of the SWAN model in the surface atmospheric temperature is rather small: it is only noted during the summer season by a slightly lower air temperature close to the coast. This difference in air temperature is reduced to almost zero some 100 km into the continent. The lower surface air temperature near the coast is a consequence of the lower surface temperature over the coastal ocean and increased onshore wind intensity in summer.

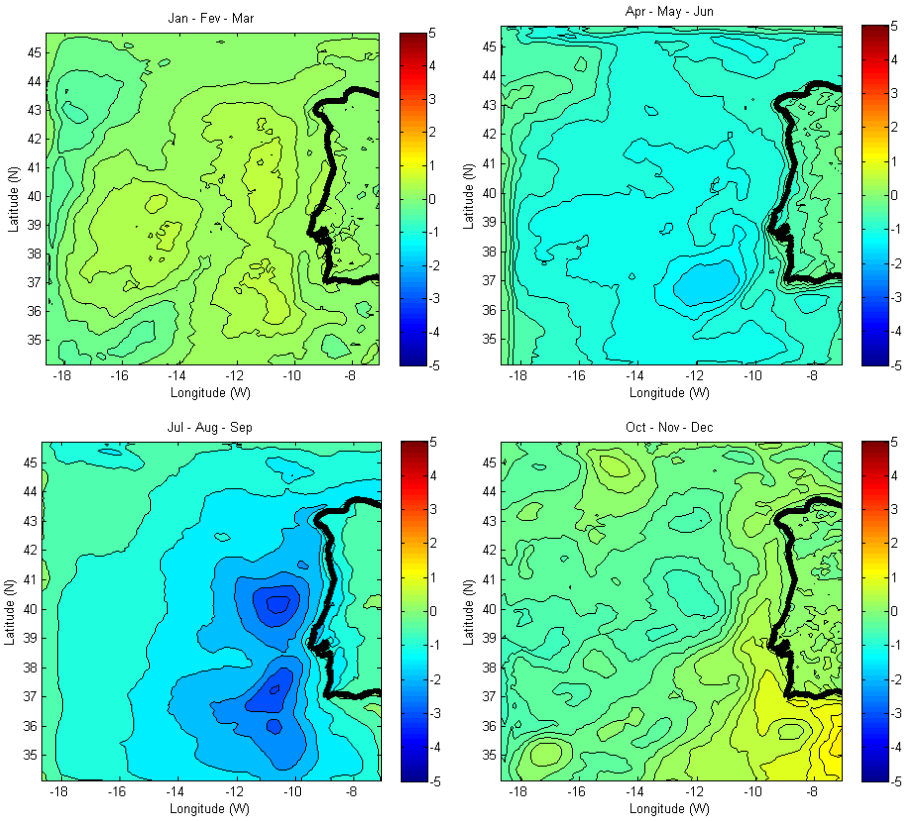

Figure 45 Mean seasonal differences in surface air temperature for the year 2002 between an experiment without and with SWAN coupled to WRF and ROMS (WRF+ROMS+SWAN minus WRF+ROMS).

In Figure 46 the mean seasonal zonal and meridional wind components are shown, as simulated by WRF+ROMS+SWAN for the year 2002. The figure shows the intensification of the zonal onshore sea-breeze during spring and summer, which is more intense in the south sector of the west coast. The sea breeze is confined to a narrow region along the western Iberia and its intensity is not uniform along the coast. In the meridional wind component one verifies that during summer it is more intense in the south than in the north part of the coast, in agreement with the surface wind stress curl maps shown in Chapter 4.

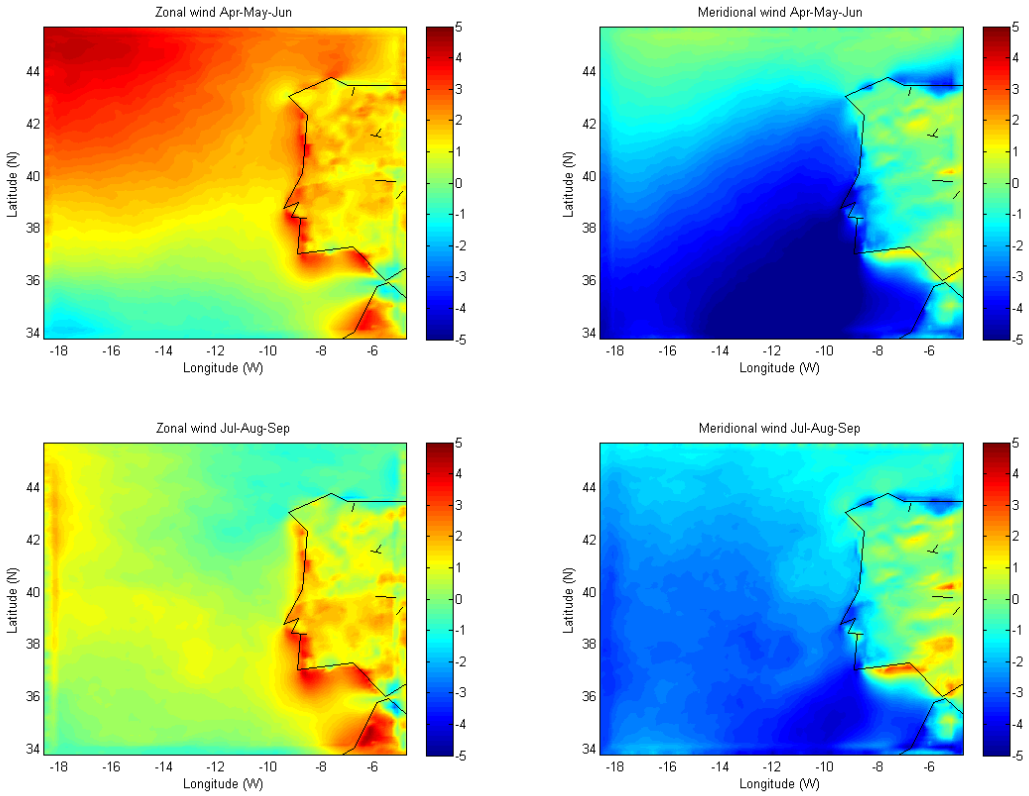

Figure 46 Mean seasonal zonal (left column) and meridional (right column) wind simulated by the WRF+ROMS+SWAN coupled experiment.

Figure 47 shows the differences of the mean zonal and meridional components of surface wind for the summer months of July, August and September, between satellite-derived winds and wind simulated by a WRF-only run, a coupled WRF+ROMS run and a fully coupled WRF+ROMS+SWAN run. The patterns of the difference (simulations-observations) in surface wind are similar among all simulation experiments. The satellite data presents higher intensity winds than those simulated by WRF. The observed biases are normally larger in the coupled experiments than in the WRF only experiment, with the exception of the zonal wind component in the northern limit of the computational domain. The better accuracy of the WRF only simulated surface wind field, should be attributed to the satellite observed SST data used in this simulation, that is more accurate than the SST filed modeled by ROMS in coupled experiments. In Figure 47 zonal wind biases are larger in the southern part of the computational domain than in the north and meridional wind biases are usually larger in the south and west limits of the domain; they are in overall terms below 2 $m.s^{-1}$, with the exception of the Iberian coastal regions where large biases are noted. When comparing the biases in WRF+ROMS and in WRF+ROMS+SWAN it can be seen that the introduction of the wave model reduced the model-observations difference in the region offshore, thus pointing to a beneficial role of the wave model in

the coupled experiments, that lead to a more accurate SST modeled field during the WRF+ROMS+SWAN experiment.

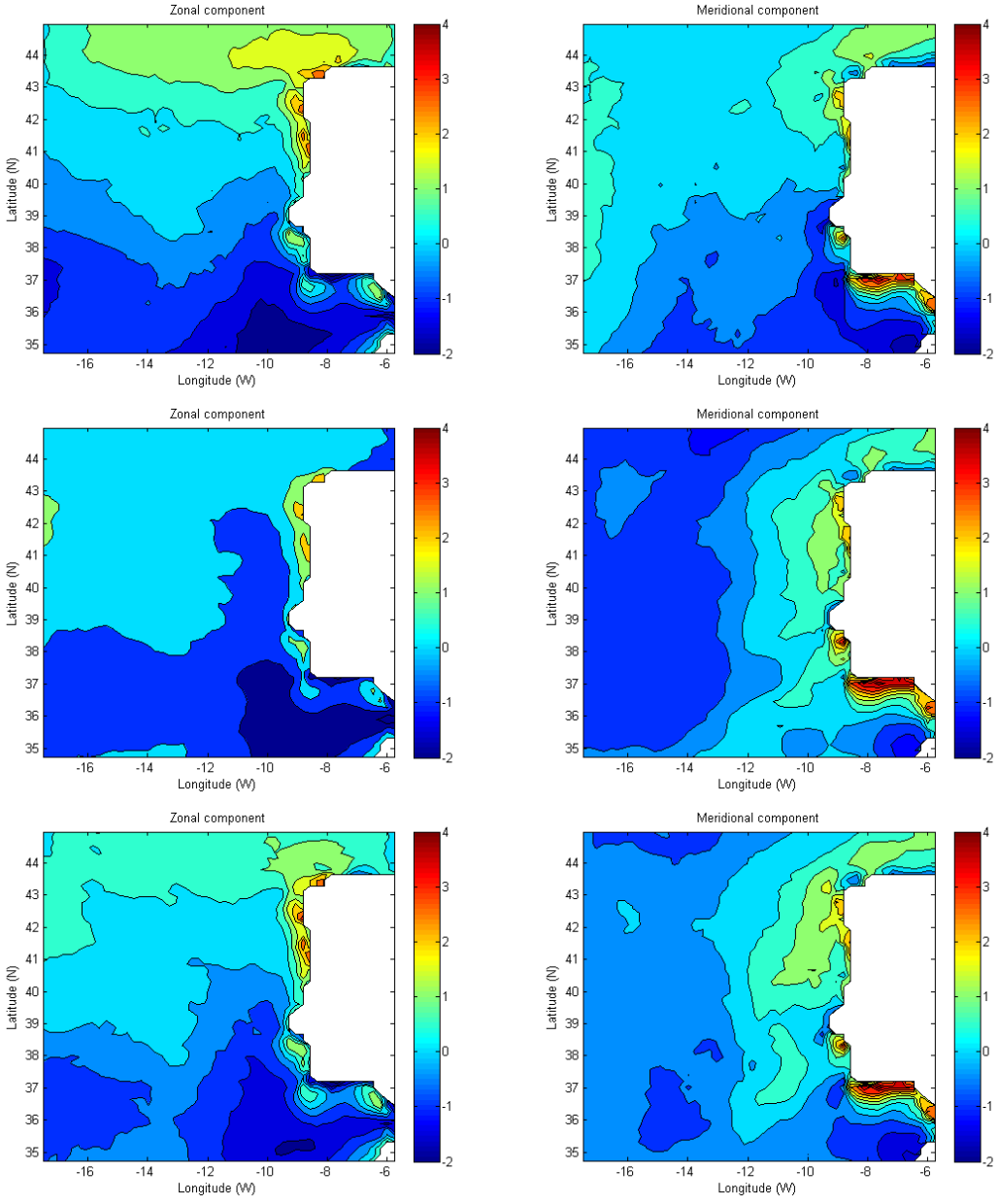

Figure 47 Average differences in (left column) zonal and (right column) meridional components of surface wind between the (top row) WRF-only, (middle row) WRF+ROMS and (bottom row) WRF+ROMS+SWAN runs and satellite-derived observational data.

The time series of SST (blue line) and meridional wind (green line) at Cape Carvoeiro, retrieved from the WRF+ROMS+SWAN coupled simulation for the year 2002, are presented in Figure 48. The correlation between SST and meridional wind during summer, is much higher (r = 0.67) than along the

entire year (r= 0.10), indicating that low coastal SST during the winter season is not related with the meridional wind intensity. During summer periods with an intensification of northerly wind are associated with a SST decrease and periods with a weakness of northerly winds are associated with a SST increase.

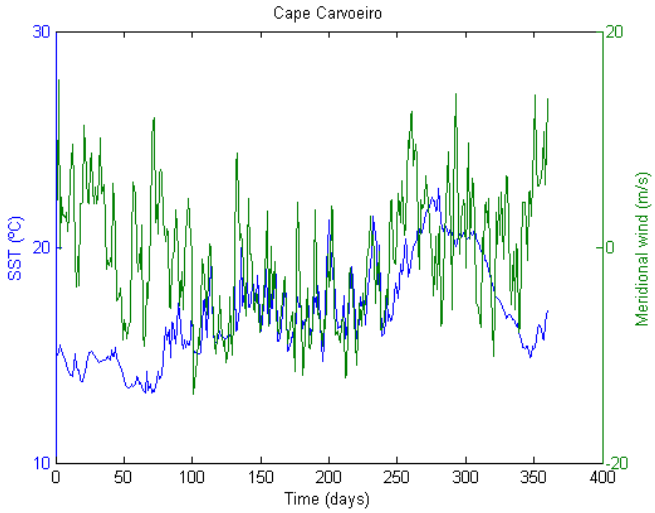

Figure 48 Time series for year 2002 of the meridional component of wind (green) and of SST (blue) at Cape Carvoeiro from the WRF+ROMS+SWAN coupled experiment.

Figure 49 shows the mean wind direction (black arrows), surface currents direction (magenta arrows) and SST for August 2002. A clear indication of coastal upwelling, characterized by a zonal coastal SST gradient, is noted. Near surface northerly wind is observed in the region more distant from the coast, whereas in the coastal region there is an increasing intensity of the zonal wind component and consequently the mean surface wind direction rotates to northwest. Offshore of western Iberia the rotation to the right of the surface currents with respect to the wind surface currents is clearly seen, as expected due to the Coriolis effect. It is noted, though, that the angle between the surface wind direction and surface currents is not constant over the computational domain, with higher angles observed in the filaments regions.

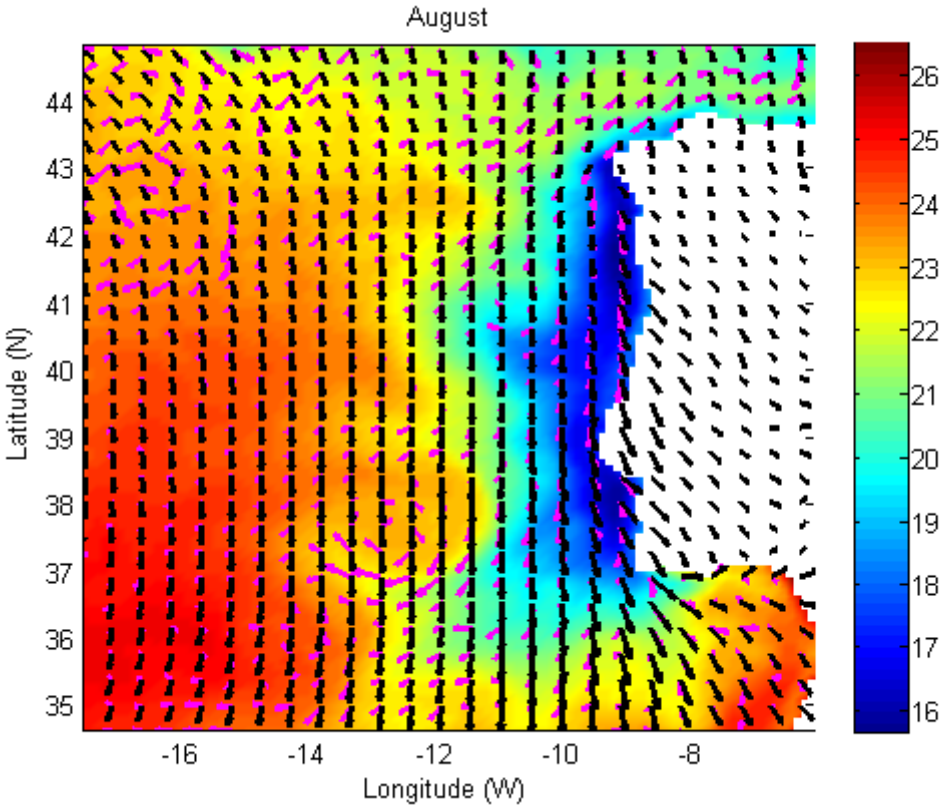

Figure 49 Mean August SST, surface currents (magenta arrows) and surface wind (black arrows), obtained from an experiment with the coupled WRF-ROMS-SWAN model.

Figure 50 shows the spatial distribution of the mean latent and sensible heat fluxes and corresponding Bowen ratio for the summer season of 2002 computed in the ROMS+WRF+SWAN run. Coastal upwelling is clearly noted on the latent and sensible heat flux mean maps for the summer season. In the latent heat flux distribution almost vanishing fluxes are observed at the coast and even more reduced values are observed in the offshore region adjacent to the coast. This is a consequence of the low temperature of upwelled water, which implies a lower surface specific humidity, in turn reducing the specific humidity vertical gradient in the first 10 m. Offshore from that region, the latent heat increases (in absolute value) away from the coast.

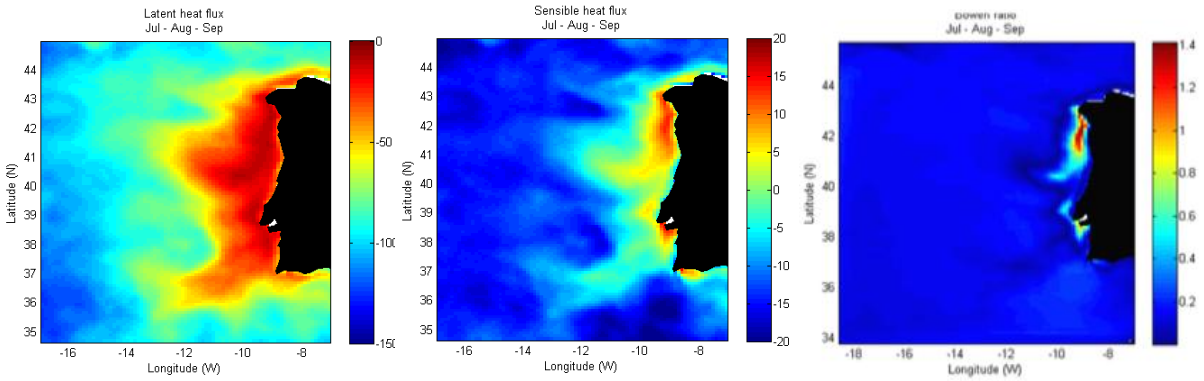

a)

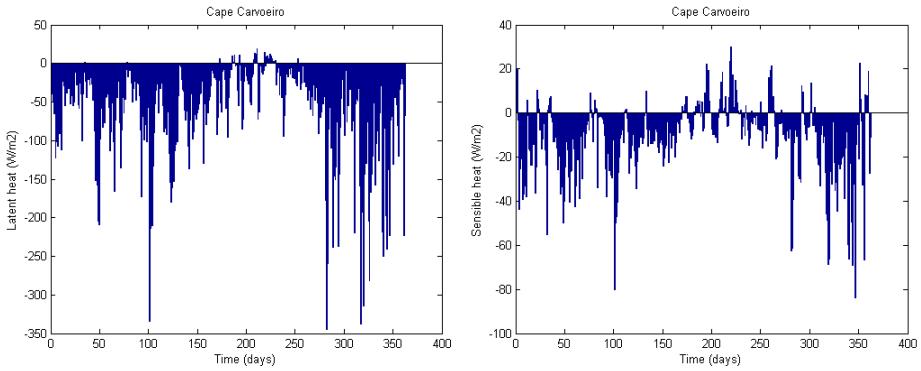

b)

Figure 50 a) Summer averaged (left) latent and (center) sensible heat fluxes and (right) Bowen ratio obtained from a WRF+ROMS+SWAN simulation for the year 2002. b) Annual time series of latent heat and sensible heat flux at Cape Carvoeiro from the same run.

The sensible heat flux map for the summer season features mostly positive values in the coastal upwelling region and negative values offshore, again a consequence of the low sea surface temperature values of the upwelled water. The Bowen ratio (Figure 50a-right), computed as the ratio between the sensible and the latent heat fluxes shows that the latent heat is larger than the sensible heat with the exception of the northwestern extreme of western Iberian coast, the region where lowest SSTs are observed during the summer season.

Figure 51 shows the time series of SSH simulated by the WRF+ROMS+SWAN coupled run for the year 2002. From the analysis of the SSH time series difference between a point close to Cape Carvoeiro and one located 200 km offshore (Figure 51-right) it is noted that during the upwelling season lower SSH values are observed close to the coast than in the computational cell located 200 km to the west of Cape Carvoeiro. During February and March of year 2002 lower SSH values were also

noted close to the coast than offshore, indicating that the dynamical behavior of coastal upwelling events can also occur during winter. During this period the mean meridional wind was southward, but a significant decrease in SST was not noted as shown in Figure 48. The almost constant SST can be justified by the weak vertical temperature gradient observed in the ocean upper layers during the winter season (Figure 44).

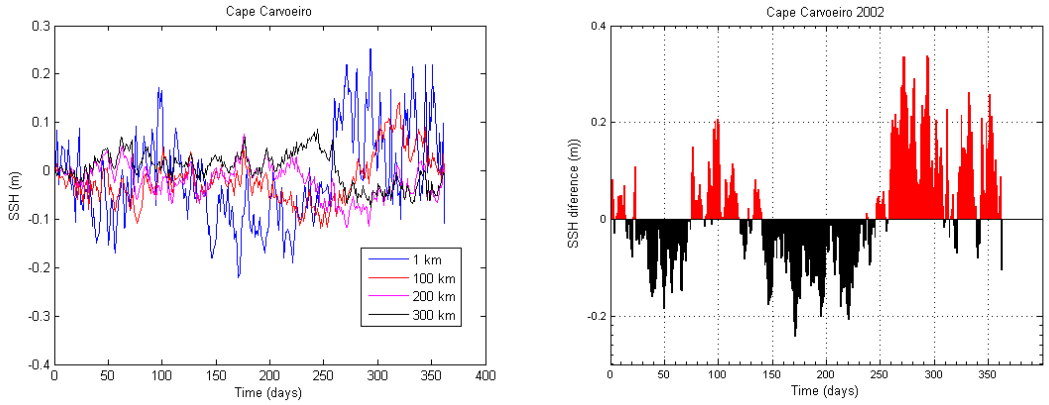

Figure 51 (left) Sea surface height at Cape Carvoeiro (blue line) and at 100 km (red line), 200 km (magenta line) and 300 km (black line) offshore from that cape. (right) Difference of SSH between Cape Carvoeiro and a location 200 km offshore.

The above results indicate that the coastal SSH gradient is a reasonable coastal upwelling index, which if used in conjunction with the usual SST index, can help to better identify lower SST events corresponding to true upwelling episodes. Indeed, the low SST values can also be due to meridional advection of cool water from the north, or due to atmospheric cooling associated with heat transfer at the atmosphere-ocean interface.

6.3 Conclusions

The numerical study conducted with the coupled model system, comprised by the ROMS, WRF and SWAN models, showed that the inclusion of the wave model had a more relevant impact on the SST and surface air temperature during the summer season. It was suggested that this is related with the vertical ocean temperature gradient, which, off the western Iberian coast, is much higher in summer than during others seasons of the year. This explained why, in spite of the mean surface wave height being lower during summer, it is during that season that the increased wave-induced turbulence is

more pronounced and impacts to a larger extent the ocean and atmosphere thermal fields. From the comparison between experiments without and with WRF and ROMS coupled to SWAN it was noted that the inclusion of the wave model implied a SST decrease of about 3°C in some regions during the summer season. During the other seasons, the SST differences due to the inclusion of the SWAN model are modest (less than 1°C). With respect to the simulated atmospheric surface temperatures over the ocean, a decrease is noted in the WRF+ROMS+SWAN experiment of 2°C in some regions. Over the continent, the surface air temperature difference between the two experiments is relatively small, with only an air temperature decrease being noted in coastal regions, related to the increased onshore wind intensity on the western Iberia (and consequent onshore advection of cool maritime air). The inclusion of the wave model had a minor impact in the simulated surface wind field (below 1 $m.s^{-1}$), with only slightly more intense surface winds in the WRF+ROMS+SWAN experiment.

In the fully coupled simulation the latent heat and sensible heat fluxes seem to serve as good coastal upwelling indices, as coastal upwelling is clearly noted in these two variables. From the SSH time series measured at different distances from Cape Carvoeiro it seems that the SSH field is also an acceptable coastal upwelling index, which allows to better identify a coastal upwelling event, since it is independent of the ocean thermal field. This way, if the SST and SSH indexes are used simultaneously, it is possible to identify days when a lower coastal SST is not due to coastal upwelling.

Chapter 7 **Conclusions and final considerations**

7.1 **Conclusions**

This chapter summarizes the main results presented in previous chapters obtained from analyses of the numerical simulations conducted with the ocean-only model and the ocean-atmosphere-wave coupled system. The main aim of the thesis was to assess trends in the coastal upwelling in the northern part of the Canary Current upwelling ecosystem, more precisely off the western Iberian coast, where it is known that coastal upwelling is episodic and subject to strong seasonality imposed by summer upwelling-favorable wind deriving from the combined effect of the Azores anticyclone and the Iberia thermal depression. Trends in the intensity and variability of dynamical variables affected by the coastal upwelling, like surface currents, SST and SSH were assessed. The study is largely based on data obtained from numerical simulations, but satellite SST data was also used to assess the trends and to validate the numerically simulated SST fields.

First, two ROMS simulations were conducted using ERA-40 (1961-2001) and ERA-Interim (1989-2008) atmospheric reanalyzes data from ECMWF. In order to simulate the lower atmospheric conditions, seven variables (surface wind, net shortwave radiation, cloud cover, precipitation, relative humidity, surface air temperature and surface pressure) were used to force the model with a 6 hour periodicity. From the analyses of the surface wind, the atmospheric variable with largest impact on coastal upwelling, opposing trends in the meridional component of wind were found in the northern and southern sectors off Iberia. This was present during the last decade of the ERA-40 period (1991-2000), during the ERA-Interim period (1989-2008) and during the satellite data period (1989-2007), although the trends have different magnitudes across the three wind sources. For instance, for the same period, trends showed to be higher in the satellite observations wind than in ERA-Interim.

The computed wind trends, characterized by a decreasing intensity in the north region and an increasing intensity in the south region, implied a decreasing intensity of upwelling in the north part of western Iberia coast and an increasing intensity in the south part of the coast. These opposing trends in upwelling were also noted in the SST satellite data retrieved from a daily Optimal Interpolated SST database.

In the present study, the coastal upwelling events were analyzed using the simulated SSTs in three sectors (north, central and south) along western Iberia. An upwelling event was defined when a

threshold of coastal cooling (between the sector close to the coast and the sector located 300 km offshore) of 2°C was attained.

The ROMS numerical experiments and the SST satellite data showed that the coastal upwelling thermal front extends to a mean offshore distance of around 200 km during the summer season. Particularly in August, the mean monthly simulated SSTs still show evidence of a weak zonal SST gradient between 200 km and 500 km from the coast, indicating that the SST front is sporadically present at distances even larger than 200 km from the coast.

The strong seasonality that characterizes the Iberian coastal upwelling was observed in the simulations and also in the satellite SST data. Both sources show that the majority of coastal upwelling events occur in the summer months. During this season an intensification of zonal and meridional coastal surface currents magnitude and variability was observed.

AVHRR observations and the ERA-Interim simulation indicate reduced intra-annual variability in the coastal waters, which is associated with cooling in the warmer period.

The period 1989-2001 is common to both ECMWF reanalyzes (ERA-40 and ERA-Interim), so it was used to assess the improvement in the simulated SST field when using the ERA-Interim instead of ERA-40 as forcing atmospheric data for ROMS. Comparing the simulated SSTs with those derived from the AVHRR satellite sensor, it was concluded that the ERA-Interim forced run is on average closer to observations, therefore showing an improvement in the new reanalysis.

The simulated SSH field showed a trend of sea level rise along the western Iberian coast, but the rate of SSH increase diminished from 1961 until 2008, which seems to indicate that the lowering effect of the increasing number of upwelling events is contributing to partially cancel in the coastal zone the rising effect of global warming.

In the simulations, upwelling days (identified as $\Delta SST > 2°C$) occur almost in all months of the year, but the dynamical properties characteristic of an upwelling event, i.e., the intensification of coastal westward and southward surface currents, upward vertical currents and the presence of a SSH zonal gradient in the region close to the coast, were only clearly noted during the summer season. That seems to indicate that the lower coastal SSTs observed in the others seasons of the year are not always due to coastal upwelling. The cold SST close to the coast observed almost in all months was also observed by satellite. It was shown that contrary to the summer season when the thermal front is present at distances of about 200 km from the coast, during others seasons the thermal front is much closer to the coast, typically at distances shorter than 50 km. It is hypothesized that the lower SST can be due to atmospheric cooling of coastal waters during the winter season, time when heat transfer from the ocean to the cold atmosphere may take place. The low coastal SST can also be due to meridional

advection of cold waters, although in the simulations an intensification of the coastal southward surface currents during the winter season was not noted. The mechanism of nearshore atmospheric cooling needs further investigation.

With the aim of assessing the impact of global warming in the Iberian coastal upwelling, a control and a scenario simulation were realized forced by atmospheric daily forcing retrieved from the RACMO regional climate model. RACMO is a regional atmospheric model developed at KNMI that was forced at its boundaries with data from the HadCM2 global model developed at the Hadley Centre, which in turn took into account the impact of greenhouse emissions as prescribed for the IPCC scenario A2. The control simulation was realized for the period 1961-1990 and the scenario for the period 2071-2100. Comparing the results obtained in the two ROMS simulations realized, an increase of the mean number of coastal upwelling days was found in all seasons during the scenario period, particularly in winter when almost no events were noted during the control period. However, a strong intra-annual seasonality continues to be noted during the last 30 years of the XXI century, with the majority of coastal upwelling events occurring during the summer season, when events as intense as $\Delta SST > 10°C$ were simulated. For the scenario period and according to the ROMS simulations, the coastal zonal and meridional surface current is also projected to increase. It was also noted that the increased number of coastal upwelling days for the scenario period is mainly verified for the more intense ones (those with $\Delta SST \geq 4$ °C). The mean number of days with events with magnitude 2 °C $\leq \Delta SST <$ 3 °C and 3 °C $\leq \Delta SST <$ 4 °C remains almost constant between the control and scenario periods. The increasing number of coastal upwelling days and the intensification of the zonal a meridional surface current is concluded to be due to the increasing intensity of coastal zonal and meridional wind components by about 10% during the scenario period. A decrease of the mean SSH along the western Iberian coast was found, which seems to indicate that the impact of the increasing number of upwelling days is large enough to suppress the rising effect of global warming on the coastal SSH.

In order to properly simulate the heat and momentum transfers at the ocean-atmosphere interface and study the impact of surface waves on the simulated SST field, a coupled modeling system comprised of an atmospheric model (WRF), an oceanic model (ROMS) and a wave model (SWAN) was used. The results obtained with the coupled system showed that the impact of the ocean surface waves on the SST field is mainly verified in summer, despite the fact that the mean significant wave height is the lowest during that season. This occurs due to the much larger vertical gradient of temperature within the ocean upper 100 m in summer.

Regarding atmospheric surface temperature, the largest difference due to the inclusion of the wave model in the coupled system occurs during summer, similarly to what was verified in the SST. Over the continent the impact of including the wave model is only noted in a narrow region close to the

western Iberian coast. The lower coastal atmospheric temperatures anomalies of about 1°C vanish almost completely at a distance of 100 km to the interior of the Peninsula. The coupled simulations also showed an increase of the zonal wind (sea breeze) during summer, as expected, due to the increased zonal gradient in the lower atmosphere temperature caused by the low temperature of upwelled water.

From the results obtained with the coupled simulations it is noticed that the air-sea sensible and latent heat fluxes are good indicators of coastal upwelling, as this coastal phenomenon has a clear signal in the distributions of these two variables. But, since these two fluxes depend essentially on the SST, the use of the heat fluxes as upwelling indices instead of SST does not seem to have significant advantages. The simulated SSH field incorporates a dynamical signal related to coastal upwelling so, when available, it should be used in addition to the SST to clearly identify periods when although a low SST is observed close to the coast, this is not due to upwelling.

7.2 **Model limitations**

The numerical experiments presented here have some limitations that stem from errors associated to the numerical methods applied to solve the advective-diffusive equations, deficiencies in sub-grid scale parameterizations (or lack of them), poor realism in the climatological data used to initialize the models, and unknown open-boundary forcing. From those, an important constraint in the multi-decadal simulations here presented is the latter monthly climatological forcing of the open lateral boundaries. For this reason, only the impact of surface boundary conditions (like the global warming signal) on coastal upwelling off Iberia was studied. The impact of the inter-annual/decadal variability of the North Atlantic circulation (and furthermore the changes due to a changing climate) was not taken into account.

More specifically, the Mediterranean Water outflow is not accurately represented in the climatological dataset used to initialize and force ROMS. This brings implications to the Gulf of Cadiz circulation (Peliz et al., 2007a). Nevertheless, a reasonably good agreement between the simulated SST and the SST obtained from satellite was shown in this study, more precisely in the regions near Cape St. Vincent, Cape Carvoeiro and Cape Finisterre during the summer season, when most of the coastal upwelling events occur. The impact of river outflows and their plumes of low density waters were also not taken into account, although it is remembered that the river outflow is much larger during winter and the upwelling is a coastal phenomenon mainly observed in summer. The possible impact of tides, with their rich spectrum of variability was also not taken into account, as this study is more focused on

decadal to multi-decadal scales. A more detailed study related with daily variability and local aspects related with small scale phenomena would require a computational grid with much more resolution as the one used. Presently it is not realistic to realize multi-decadal integrations at high resolution due to the required computational resources and the data storage capacity.

7.3 Suggestions for future work

To further deepen the study of the ocean-atmosphere exchange offshore Iberia it is essential to have access to observational data, which at the present time is very scarce in the studied region. For this reason it is suggested the deployment of a collection of buoys capable of measuring in real time oceanic and atmospheric variables off western Iberian coast. This grid of observational buoys could be similar to the ones existing in others coastal regions. For example the one off the eastern coast of the United States of America installed as part of the CBLAST (Coupled Boundary Layers Air-Sea Transfer) program (Edson et al., 2007). These observational buoys would also contribute to improve weather analysis and prediction, since most of the synoptic systems that affect the Iberia Peninsula move eastwards from the ocean to the continent. The data retrieved from a grid of buoys would also be essential in the validation of the numerically simulated heat and momentum fluxes. To maximize the usefulness of the data retrieved from these buoys they should be made available to the international community in a nationally operated data center.

On the modeling side, a long-term simulation from 1850 until 2100 with ocean and atmospheric data retrieved from an EC-Earth (Hazeleger et al., 2010) simulation will be pursuit. These data will allow to initialize and to force the boundaries of the coupled WRF and ROMS system in a consistent manner. This way it will be possible to assess the impact of ocean circulation variability on the upwelling regime. It is also proposed to extend the computational domain eastwards (and use year-long observed hydrological data from the Strait of Gibraltar) and southwards, in order to have the entire Canary Current upwelling ecosystem simulated.

References

Alvarez, I., M. deCastro, R. Prego, M. Gomez-Gesteira, 2003: Hydrographic characterization of a winter-upwelling event in the Ria of Pontevedra (NW Spain). *Estuarine Coastal and Shelf Science* 56, 869–876.

Alvarez, I., M. Gomez-Gesteira, M. deCastro, J-M. Dias, 2008: Spatio-temporal evolution of upwelling regime along the western coast of the Iberian Peninsula. *Journal of Geophysical Research* 113, C07020.doi: 10.1029/2008JC004744.

Alvarez,I., M. Gomez-Gesteira, M. deCastro, M.N. Lorenzo, A.J.C. Crespo A, J.M. Dias, 2010: Comparative analysis of upwelling influence between the western and northern coast of the Iberian Peninsula. *Continental Shelf Research*,doi:10.1016/j.csr.2010.07.009

Alvarez-Salgado, X. A., G. Roson, F. F. Perez, and Y. Pazos , 1993: Hydrographic variability off the RiasBaixas (NW, Spain) during the upwelling season, *Journal of Geophysical Research*, 98, 14,447– 14,455, doi:10.1029/93JC00458.

Ambar, I., J. Dias, 2008: Remote Sensing of Coastal Upwelling in the North-Eastern Atlantic Ocean, in *Remote Sensing of the European Seas* edited by V. Barale and M. Gade, pp 141-152, Springer.

Aristegui J., E.D. Barton, X. A.Alvarez-Salgado, A. M. P. Santos, F.G. Figueiras, S. Kifani, S. Hernandez-Leon, E. Mason, E. Machu, H. Demarcq, 2009: Sub-regional ecosystem variability in the Canary Current upwrelling *Progress in Oceanography*, 83 (1-4), p. 33-48. ISSN 0079-6611

Bakun, A., 1990: Global climate change and intensification of coastal ocean upwelling. *Science* 247, 198–201. 247/4939/198.

Bakun A. and C.S. Nelson, 1991: The seasonal cycle of wind stress curl in sub-tropical eastern boundary current regions. *Journal Physical Oceanography*, 21, 1815-1834.

Barton E.D., A. Huyer, R.L. Smith, 1977: Temporal variation observed in the hydrographic regime near CaboCorveiro in the northwest African upwelling region, February to April 1974, *Deep-Sea Research*., 24,7-23.

Barton, E. D., Arıstegui, J., Tett, P., Canton, M., Garcıa-Braun, J., Hernandez-Leon, S., Nykjaer, L., Almeida, C., Almunia, J.,Ballesteros, S., Basterretxea, G., Escanez, J., Garcıa-Weill, L., Hernandez-Guerra, A., Lopez-Laatzen, F., Molina, R., Montero, M. F., Navarro-Perez, E., Rodrıguez, J. M., van Lenning, K., Velez, H., & Wild, K., 1998: The transition zone of the Canary Current upwelling region. *Progress in Oceanography*, *41*, 455–504.

Barton, E. D., M. E. Inall, T. J. Sherwin, and R. Torres, 2001: Vertical structure, turbulent mixing and fluxes during Lagrangian observations of an upwelling filament system off northwest Iberia, *Progress in Oceanography*, 51, 249–267, doi:10.1016/S0079-6611(01)00069-6.

Blanke, B., C. Roy, P. Penven, S. Speich, J. McWilliams, and G. Nelson, 2002: Linking wind and upwelling interannual variability in a regional model of the southern Benguela. *Geophysical Research Letters*., *2*9, 2188, doi :10.1029/2002GL015718.

Blanton, J. O., L. P. Atkinson, F. Castillejo, and A. L. Montero, 1984: Coastal upwelling of the RiasBajas, Galicia, northwest Spain, I; hydrographic studies, *Rapp. P. V. Reun. Cons. Int. Explor. Mer.*, 183, 179–190.

Beljaars, A.C.M., 1994: The parameterization of surface fluxes in large-scale models under free convection, *Quarterly Journal of the Royal Meteorological Society*,121, 255–270.

Berliand ME, Berliand TG. 1952. Determining the net longwaveradiation of the Earth with consideration of the effect of cloudiness .Izvestiya Akademiya Nauk SSSR, SeriaGeofizika 1: 64–78.

Bode,A., M.T. Alvarez-Ossorio, J.M. Cabanas, A.M. Miranda, Varela, 2009: Recent trends in plankton and upwelling intensity off Galicia (NWSpain) .*Progress in Oceanography* 83,342–350.

Booij, N., R.C. Ris and L.H. Holthuijsen, 1999: A third-generation wave model for coastal regions, Part I, Model description and validation, *Journal of Geophysical. Research*. C4, 104, 7649-7666.

Capet, X.J., P. Marchesiello, J.C. McWilliams, 2004: Upwelling response to coastal wind profiles. *Geophysical Research Letters* 31, L13311. doi:10.1029/2004GL020123.

Chelton, D. B., 2005: The impact of SST specification on ECMWF surface wind stress fields in the eastern tropical Pacific. *Journal of Climate*, 18, 530–550.

Chelton, D. B., M.G. Schlax , R.M. Samelson, 2007: Summertime Coupling between Sea Surface Temperature and Wind Stress in the California Current System *Journal of Physical Oceanogr*aphy, 37, 495-517.

Chen, F., and J. Dudhia, 2001: Coupling an advanced land-surface/ hydrology model with the Penn State/ NCAR MM5 modeling system. Part I: Model description and implementation. *Monthly Weather Review*, 129, 569–585.

Christensen JH, TR Carter, F Giorgi, 2002: PRUDENCE employs new methods to assess European climate change. *EOS* 83:147

Christensen JH, OB Christensen, 2007: A summary of the prudence model projections of changes in European climate during this century. *Climate Change* 81, 7-30

Cox,M.D. (1984) A primitive equation, three-dimensional model of the ocean. GFDL Ocean Group Technical Report No. 1, GFDL, Princeton, NJ,USA, 143 pp

Cullen,M.J.P. (1993) The unified forecast/climate model *Meteor. Mag*.,122, 81-94.

Cushman-Roisin, B., 1994. *Introduction to Geophysical Fluid Dynamics*.Prentice Hall, 320 pp.

deCastro,M., A.W.Dale, M. Gomez-Gesteira, R. Prego, I. Alvarez, 2006: Hydrographic and atmospheric analysis of an autumnal upwelling event in the Ria of Vigo (NW Iberian Peninsula). *Estuarine Coastal and Shelf Science* 68, 529–537. doi:10.1016/j.ecss.2006.03.004.

deCastro, M., M. Gomez-Gesteira, M.N. Lorenzo, I. Alvarez, AJC, Crespo, 2008: Influence of atmospheric modes on coastal upwelling along the western coast of the Iberian Peninsula, 1985 to 2005. *Climate Research* 36, 169–179. doi:10.3354/cr00742.

Dee, D. P., Uppala, S. M., Simmons, A. J., Berrisford, P., Poli, P., Kobayashi, S., Andrae, U., Balmaseda, M. A., Balsamo, G., Bauer, P., Bechtold, P., Beljaars, A. C. M., van de Berg, L., Bidlot, J., Bormann, N., Delsol, C., Dragani, R., Fuentes, M., Geer, A. J., Haimberger, L., Healy, S. B., Hersbach, H., Hólm, E. V., Isaksen, L., Kållberg, P., Köhler, M., Matricardi, M., McNally, A. P., Monge-Sanz, B. M., Morcrette, J.-J., Park, B.-K., Peubey, C., de Rosnay, P., Tavolato, C., Thépaut, J.-N. andVitart, F., 2011: The ERA-Interim reanalysis: configuration and performance of the data assimilation system. *Quarterly Journal of the Royal Meteorological Society*, 137: 553–597. doi: 10.1002/qj.828

Demarcq, H., 2009: Trends in primary production, sea surface temperature and wind in upwelling systems (1998–2007). *Progress in Oceanography*, *83*(1-4), 376-385.

Dorman C E, E. P. Dever, J. Largier, and D. Koracin, 2006: Buoy measured wind, wind stress and wind stress curl over the shelf off Bodega Bay. *Deep-Sea Research II*, 53, 2850–2864.

Dudhia, J., 1989: Numerical study of convection observed during the winter monsoon experiment using a mesoscale two-dimensional model, *Journal of Atmospheric Science*, 46, 3077–3107.

Dyer, A. J., and B. B. Hicks, 1970: Flux-gradient relationships in the constant flux layer, *Quarterly Journal of the Royal Meteorological Society* 96, 715–721.

Echevin, V., Aumont, O., Ledesma, J., Flores, G. 2008: The seasonal cycle of surface chlorophyll in the Peru upwelling system: a modelling study. *Progress in Oceanography* 79, 167-176.

Edson, James, and Coauthors, 2007: The Coupled Boundary Layers and Air–Sea Transfer Experiment in Low Winds. *Bulletim of the American Meteorological Society*,88, 341–356. doi: 10.1175/BAMS-88-3-341

Estrade, P.; Marchesiello, P.; De Verdière, A. C.; Roy, C. 2008: Cross-shelf structure of coastal upwelling: A two — dimensional extension of Ekman's theory and a mechanism for inner shelf upwelling shut down *Journal of Marine Research*, Volume 66, Number 5, September, pp. 589-616(28)

Fairall, C, W., E.R. Bradley, D.P. Rogers, J.B.Edson& G.S. Young, 1996: Bulk parameterization of air-sea fluxes in TOGA COARE. *Journal of Geophyical. Research.*, 101, 3747 - 3767.

Fairall, C.W., E.F. Bradley, J.E.Hare, A.A.Grachev& J.B. Edson, 2003: Bulk Parameterization of Air-Sea Fluxes: Updates and Verification for the COARE Algorithm. *Journal of Climate*, 16, 571 - 591.

Figueroa, D., and C. Moffat, 2000: On the influence of topography in the induction of coastal upwelling along the Chilean Coast, *Geophysical Research. Leters.*, 27(23), 3905–3908, doi:10.1029/1999GL011302.

Fiuza, A., M. Macedo, and M. Guerreiro, 1982: Climatological space and time variation of the Portuguese coastal upwelling, *Oceanological Acta*, 5, 31–40.

Fiuza, A.F.G., 1983: "Upwelling Patterns Off Portugal", 85-98 in "Coastal Upwelling: its Sediment Record", E. Suess& J. Thiede (editores), Plenum Publ. Co.

Fraga, F.,1981: Upwelling off the Galician Coast, Northwest Spain, in Coastal Upwelling, *Coastal Estuarine Stud.*, vol. 1, edited by F. A. Richards, pp. 176– 182, AGU, Washington, D. C.

Gomez-Gesteira, M.,Moreira,C.,Alvarez,I.,deCastro,M., 2006: Ekman transport along the Galician coast (NW,Spain) calculated from forecasted winds .*Journal of Geophysical Research* 111,C10005.doi:10.1029/2005JC003331.

Haidvogel, D.B., H.G. Arango, K. Hedstrom, . Beckmann, P. Malanotte-Rizzoli, A.F. Shchepetkin, 2000: Model evaluation experiments in the North Atlantic Basin: simulations in nonlinear terrain-following coordinates, *Dynamics of Atmospheres and Oceans*, 32, 239-281.

Haynes, R., E. D. Barton, and I. Pilling, 1993: Development, persistence and variability of upwelling filaments off the Atlantic coast of the Iberian Peninsula, *Journal Geophysical. Research.*, 98, 22,681 – 22,692, doi:10.1029/ 93JC02016.

Hazeleger, W., C. Severijns, T. Semmler, S. Stefanescu, S. Yang, X. Wang, K. Wyser, E. Dutra, J. Baldasano, R. Bintanja, P. Bougeault, R. Caballero, A. M. L. Ekman, J. H. Christensen, B. van den Hurk, P. Jimenez, C. Jones, P. Kallberg, T. Koenigk, R. McGrath, P. Miranda, T. Noije, T. Palmer, J. Parodi, T. Schmith, F. Selten, T. Storelvmo, A. Sterl, H. Tapamo, M. Vancoppenolle, P. Viterbo, U. Willén, 2010 : EC-Earth: A Seamless Earth System Prediction Approach in Action. *Bulletim of the American Meteorological Society*, 91, 1357-1363 .doi: 10.1175/2010BAMS2877.1

Hodur, R. M., 1997: The Naval Research Laboratory's Coupled Ocean/Atmosphere Mesoscale Prediction System (COAMPS). *Monthly Weather Review*, 125, 1414–1430.

Hong, S.-Y., J. Dudhia, and S.-H. Chen, 2004: A Revised Approach to Ice Microphysical Processes for the Bulk Parameterization of Clouds and Precipitation, *Monthly Weather Review*, 132, 103–120.

Hong, S.-Y., and J.O.J. Lim, 2006: The WRF Single-Moment 6-Class Microphysics Scheme (WSM6), *Journal of Korean Meteorological Society.*, 42, 129–151.

Hong, S.-Y., and Y. Noh, and J. Dudhia, 2006: A new vertical diffusion package with an explicit treatment of entrainment processes. *Monthly Weather Review* 134, 2318–2341.

Hughes P., E.D. Barton, 1974a: Stratification and water mass structure in the upwelling area off northwest Africa in April/May 1969, *Deep-Sea Research*, 21, 611-628.

Hughes P., E.D. Barton, 1974b: Physical investigations in the upwelling region of north west Africa on RSS Discovery cruise 48 *TETHYS* 6 (1-2) 1974 pp. 43-52

Huthnance, J. M., 1984: Slope currents and ''JEBAR.'' *Journal PhysicalOceanography.*,**14,** 795–810.

Kain, J. S., 2004: The Kain-Fritsch convective parameterization: An update. *Journal of Applied Meteorology*, 43, 170–181.

Jackett, D. R. and T. J. McDougall, 1995: Minimal Adjustment of Hydrostatic Profiles to Achieve Static Stability, *Journal of Atmospheric and Oceanic Technology*, 12, 381-389.

Jacob, R., J. Larson, E. Ong, 2005: M N Communication and Parallel Interpolation in CCSM Using the Model Coupling Toolkit. Preprint ANL/MCSP1225-0205. Mathematics and Computer Science Division, Argonne National Laboratory, 25 pp.

Jones, P.W., 1998: A Users Guide for SCRIP: A Spherical Coordinate Remapping and Interpolation Package. V 1.4, Los Alamos National Laboratory. http://climate.lanl.gov/Software/SCRIP/.

Larson, J., R. Jacob, E. Ong, 2004: The Model Coupling Toolkit: A New Fortran90 Toolkit for Building Multiphysics Parallel Coupled Models. Preprint ANL/MCSP1208-1204. Mathematics and Computer Science Division, Argonne National Laboratory, 25 pp.

Jin, Xin, Changming Dong, JaisonKurian, James C. McWilliams, Dudley B. Chelton, Zhijin Li, 2009: SST–Wind Interaction in Coastal Upwelling: Oceanic Simulation with Empirical Coupling. *Journal of Physical Oceanography*, **39**, 2957–2970. doi: 10.1175/2009JPO4205.1

Lemos, R.T., HO Pires, 2004: The upwelling regime off the West Portuguese coast, 1941–2000. *International Journal of Climatology* 24, 511–524.

Locarnini, R.A., A.V. Mishonov, J.I. Antonov, T.P. Boyer, and H. E. Garcia, 2006: World Ocean Atlas 2005, Volume 1: Temperature. S. Levitus, Ed. NOAA Atlas NESDIS 61, U.S. Government Printing Office, Washington, D.C., 182 pp, CD-ROM.

Mlawer, E. J., S. J. Taubman, P. D. Brown, M. J. Iacono, and S. A. Clough, 1997: Radiative transfer for inhomogeneous atmosphere: RRTM, a validated correlated-k model for the longwave. *Journal of Geophysical Research*, 102 (D14), 16663–16682.

Marchesiello, P., JC. McWilliams, A. Shchepetkin, 2001: Open boundary conditions for long-term integration of regional oceanic models. *Ocean Modelling* 3, 1–20.

Marullo, S., Buongiorno Nardelli, B., Guarracino, M., and Santoleri, R., 2007: Observing the Mediterranean Sea from space: 21 years of Pathfinder-AVHRR sea surface temperatures (1985 to 2005): re-analysis and validation, *Ocean Science*, 3, 299-310, doi:10.5194/os-3-299-2007

McGregor, H.V., Dima, M., Fisher, W., Mulitza, S., 2007: Rapid 20th-century increase in coastal upwelling off Northwest Africa. *Science* 312, 637–639. doi:10.1126.1134839.

Mitas, C.M., A. Clement, 2006: Recent behavior of the Hadley cell and tropical thermodynamics in climate models and reanalyses. *Geophysical Research Letters* 33, L01810. doi:10.1029/2005GL024406.

Murphy,J.M. (1995) Transient response of the Hadley Centre coupled ocean-atmosphere model to increasing carbon dioxide. Part I, control climate and flux adjustment *Journal of Climate*, 8, 36-56

Narayan N., Paul A., Mulitza S., Schulz M., 2010: Trends in coastal upwelling intensity *Ocean Science*, 6, 815–823, 2010

Nykjaer,L., L. VanCamp, 1994: Seasonal and Inter annual variability of coastal upwelling along northwest Africa and Portugal from 1981 to 1991. *Journal of Geophysical Research* 99 (C7), 14197–14207.

Oliveira, P.B., R. Nolasco R., J. Dubert , T. Moita, A. Peliz , 2009: Summer diatom and dinoflagellate blooms in Lisbon Bay from 2002 to 2005: Pre-conditions inferred from wind and satellite data. *Progress in Oceanography*,doi:10.1016/j.pocean.2009.07.030

O'Neill, LW Dudley B. Chelton, Steven K. Esbensen., 2010: The Effects of SST-Induced Surface Wind Speed and Direction Gradients on Midlatitude Surface Vorticity and Divergence. *Journal of Climate* 23:2, 255-281

Parker, D. E.; H. Wilson; P.D. Jones; J.R. Christy; C.K. Folland, 1996: The impact of Mount Pinatubo on worldwide temperatures international *Journal of Climatology*, Vol. 16,487497

Paulson, C. A., 1970: The mathematical representation of wind speed and temperature profiles in the unstable atmospheric surface layer. *Journal of Applied Meteorology*, 9, 857–861.

Peliz, A., T. Rosa, A. M. P. Santos, and J. Pissarra, 2002: Fronts, jets, and counter flows in the Western Iberian upwelling system, *Journal of Marine Systems*,35(1 –2), 61–77.

Peliz, A., J. Dubert, P. Marchesiello, A. Teles-Machado, 2007a: Circulation in the Gulf of Cadiz: Part 1 Model and Mean flow structure. *Journal of Geophysical Research* 112, C11, C11015, doi:10.1029/2007JC004159

Peliz, A., P. Marchesiello, J. Dubert, M. Marta Almeida, C. Roy, H. Queiroga, 2007b: A study of crab larvae dispersal on the Western Iberian Shelf : physical Processes .*Journal of Marine Systems* 68 , 215–236.

Penven, P., C. Roy, J. R. E. Lutjeharms, A. Colin de Verdiere, A. Johnson, F. Shillington, P. Freon, and G. Brundrit, 2001: A regional hydrodynamic model of the Southern Benguela, *South Africa Journal of Science*, 97, 472– 476.

Penven, P., J. Echevin, J. Pasapera, F. Colas, and J. Tam, 2005: Average circulation, seasonal cycle, and mesoscale dynamics of the Peru Current System: A modeling approach, *Journal of Geophysical Research*, 110, C10021, doi:10.1029/2005JC002945.

Penven, P., L. Debreu, P. Marchesiello, and J. McWilliams, 2006: Evaluation and application of the ROMS 1-way embedding procedure to the Central California Upwelling System, *Ocean Modelling*, 12, 157–187.

Perlin,N, E. D. Skyllingstad, R. M. Samelson, and P. L. Barbour, 2007: Numerical simulation of air–sea coupling during coastal upwelling. *Journal Physical Oceanography*, 37, 837–854.

Perlin, N., E. D. Skyllingstad, and R. M. Samelson, 2011: Coastal atmospheric circulation around a cape and its response to wind-driven upwelling studied using a coupled ocean-atmosphere model. *Monthly Weather Review*, 139, 809-829.

Perez, F. F., A. F. Rıos, B. A. King, and R. T. Pollard, 1995: Decadal changes of the q-S relationship of the Eastern North Atlantic Central Water, *Deep Sea Research, Part I*, 42, 1849 – 1864, doi:10.1016/0967-0637(95)00091-7.

Relvas, P, Luis J, Santos, A.M.P., 2009: Decadal Changes in the Canary System *Geophysical Research Letters*, Vol. 36, L22601, doi:10.1029/2009GL040504

Santos, A.M.P., Peliz, A., Dubert, J., Oliveira, P.B., Angelico, M.M., Ré, P., 2004: Impact of a winter upwelling event on the distribution and transport of sardine eggs and larvae off western Iberia: a retention mechanism. *Continental Shelf Research* 24, 149–165.

Santos, A., A. Kazmin, and A. Peliz, 2005: Decadal changes in the Canary upwelling system as revealed by satellite observations: Their impact on productivity, *Journal of Marine Research*, 63, 359– 379.

Seidel, D.J., Q. Fu, W.J. Randel, T.J. Reichler, 2008: Widening of the tropical belt in a changing climate. *Nature Geoscience* 1, 21–24. doi:10.1038/ngeo.2007.38.

Seo, H., A.J. Miller, and J.O. Roads., 2007: The Scripps Coupled Ocean-Atmosphere Regional (SCOAR) model, with applications in the eastern Pacific sector. *Journal of Climate* 20:381–402

Shchepetkin, A. and J.C. McWilliams, 2003: A method for computing horizontal pressure-gradient force in an ocean model with a nonaligned vertical coordinate. *Journal of Geophysical Research* 108 (C3), 3090.doi:10.1029/2001JC001047.

Shchepetkin, A.F., and J.C. McWilliams, 2005: The regional oceanic modeling system (ROMS):a split-explicit, free-surface, topography – following – coordinate oceanic model. *Ocean Modelling* 9(4), 347–404.Skamarock, W.C.,Klemp, J.B.,Dudhia, J.,Gill, D.O.,Barker, D.M., Wang,W., Powers,

Shchepetkin, A. F. and J. C. McWilliams, 2009: Computational kernel algorithms for fine-scale, multi-process, long-term oceanic simulations. In: Handbook of Numerical Analysis, Vol. XIV: Computational Methods for the Ocean and the Atmosphere, P. G. Ciarlet, editor, R. Temam& J. Tribbia, guest eds., Elsevier *Science*, pp. 121-183,doi:10.1016/S1570-8659(08)01202-0

Skamarock, W. C., J. B. Klemp, J. Dudhia, D. O. Gill, D. M. Barker, M. Duda, X.-Y. Huang, W. Wang and J. G. Powers, 2008: A Description of the Advanced Research WRF Version 3 NCAR Technical Note.

Taylor, P.K., M.J. Yelland, 2000: The dependence of sea surface roughness on the height and steepness of the waves. *Journal of Physical Oceanography* 31, 572–590.

Tenore, K. R., R. M. Cal, R. B. Hanson, E. Lopez-Jamar, G. Santiago, and J. M. Tietjen, 1984: Coastal upwelling off the RiasBajas, Galicia, Northwest Spain. II Benthic studies, Rapp. P. V. Reun. Cons. Int. Explor. Mer., 183, 91– 100.

Uppala, S.M., P.W. Kållberg, A.J. Simmons, U. Andrae, V. da Costa Bechtold, M. Fiorino, J.K. Gibson, J. Haseler, A. Hernandez, G.A. Kelly, X. Li, K. Onogi, S. Saarinen, N. Sokka, R.P. Allan, E. Andersson, K. Arpe, M.A. Balmaseda, A.C.M. Beljaars, L. van de Berg, J. Bidlot, N. Bormann, S. Caires, F. Chevallier, A. Dethof, M. Dragosavac, M. Fisher, M. Fuentes, S. Hagemann, E. Hólm, B.J. Hoskins, L. Isaksen, P.A.E.M. Janssen, R. Jenne, A.P. McNally, J.F. Mahfouf, J.J. Morcrette, N.A. Rayner, R.W. Saunders, P. Simon, A. Sterl, K.E. Trenberth, A. Untch, D. Vasiljevic, P. Viterbo, and J. Woollen, 2005: The ERA-40 re-analysis. *Quarterly Journal of the Royal Meteorological Society*, 131, 2961-3012.doi:10.1256/qj.04.176

vanMeijgaard, E., L. van Ulft, W. van de Berg, F. Bosveld, B. van den Hurk, G. Lenderink, and A. Siebesma, 2008: The KNMI regional atmospheric climate model RACMO, version 2.1, Tech. Rep. 302, R. Neth. Meteorol. Inst., De Bilt, Netherlands.

Wallace, J. M., T. P. Mitchell, and C. Deser, 1989: The influence of sea surface temperature on surface wind in the eastern equatorial Pacific: Seasonal and interannual variability. *Journal of Climate*, 2, 1492–1499.

Warner, J. C., C. R. Sherwood, H. G. Arango, and R. P. Signell, 2005: Performance of four turbulence closure methods implemented using a generic length scale method, *Ocean Modelling*, 8, 81-113.

Warner, J. C., N. Perlin, E. D. Skyllingstad, 2008: Using the Model Coupling Toolkit to couple earth system models, *Environmental Modelling& Software*, 23, 1240-1249.

Warner, J.C., B. Armstrong, R. He, and J.B. Zambon, 2010: Development of a Coupled Ocean-Atmosphere-Wave-Sediment Transport (COAWST) modeling system: *Ocean Modeling*, v. 35, no. 3, p. 230-244.

Webb, E. K., 1970: Profile relationships: The log-linear range and extension to strong stability, *Quarterly Journal of the Royal Meteorological Society*,96, 67–90.

Wooster, W. S., A. Bakun, and D. R. McClain, 1976: The seasonal upwelling cycle along the eastern boundary of the north Atlantic, *Journal of Marine Research*, 34, 131– 141.